MODELING AND DESIGN OF MODIFIED FABRY-PEROT SEMICONDUCTOR LASERS

MODELING AND DESIGN OF MODIFIED FABRY-PEROT SEMICONDUCTOR LASERS

By

Yu Li,

M.Sc.

A Thesis

Submitted to the School of Graduate Studies

in Partial Fulfilment of the Requirements

for the Degree

Doctor of Philosophy

McMaster University

DOCTOR OF PHILOSOPHY (2011) McMaster University

(Electrical and Computer Engineering) Hamilton, Ontario

TITLE:	Modeling and design of modified Fabry-Perot semiconductor lasers
AUTHOR:	Yu Li M.Sc. (Physics Department, Brock University, Canada) B.Sc., (School of Physics and Microelectronics, Shandong University, China)
SUPERVISOR:	Dr. Wei-Ping Huang Professor, Department of Electrical and Computer Engineering
NUMBER OF PAGES:	xiv, 134

Abstract

New types of laser using the basic structure of FP cavity are designed and modelled, to achieve high SMSR single-mode lasing that can be immune to high level of optical feedbacks for optical network communication applications.

The work includes design of asymmetric Bragg reflection waveguide laser that employs wavelength selective Bragg reflectors as the claddings to confine and filter desired FP longitudinal modes for amplification and lasing. Si-rich SiO_2 single-mode laser based on this structure is also proposed and analysed.

To optimize a recent design of discrete mode laser that is re-growth free and feedback-perturbation insensitive, a comprehensive implementation of the time domain transfer matrix method, including temperature and feedback effects, is carried out. The model helps to obtain a optimized DM structure that is balanced between high SMSR and low feedback sensitivity.

.

Acknowledgements

I would like to express my sincere gratitude to my supervisor Dr. Wei-Ping Huang for all his guidance and supports during the Ph.D. studies at McMaster. I would also like to express my special thanks to Dr. Xun Li for his generous and indispensible helps for the research and degree throughout the four years. My special thanks also go to Dr. Yanping Xi, who is always whole-heartedly helping me out of those difficulties during the research.

The life at Mac can not be so colourful and memorable without everybody of the research group, where Qingyi, Hanlin, Lanxin, Lanyi, Yuchun and Zhanghua must be the special friends I would like to thank. Also, I would like to thank Dr. Qiuping Bian for his always helps in the six years both at Brock and Mac.

Finally, I would like to thank again my families and friends at home for their always heart-feeling words and supports during the so many years in Canada. Without them all, the peace-minded life of mine here would not be possible.

Contents

List of Figures

Chapter 1
Introduction

1.1 Background of the Research

Semiconductor laser has been widely used in the optical communication networks [1] as the premium light sources to generate digital signals for information transmissions. Then, the reliability and spectral purity of those lasers would be of great importance in the network system construction to guarantee any communications of their best quality. The edge-emitting Fabry-Perot (FP) laser has the simplest and most economical laser structure available in this category; however, it operates in multi-mode intrinsically with mode spacing determined by the FP cavity length. In long-haul fiber-optic communication systems, pure single-mode laser has to be used to avoid transmission caused deterioration of signal quality at high modulation speed. Thus, specific modifications on the FP structures would be required to make the laser working at single-mode state with high spectrum purity.

As one of the engineered single-mode laser candidates, distributed Bragg reflector (DBR) laser [2-4] can be viewed as the combination of an active FP resonance region and two frequency-selective passive mirrors on the cavity's both end-facets. The selected wavelength of light by the mirrors can achieve constructive interference and amplification inside the cavity, to finally reach the single-mode lasing out of one or both ends. On the other hand, the distributed-feedback (DFB) laser [2, 3, 5], which has thousands of reflectional gratings periodically etched above the active layer along the FP longitudinal cavity, can be regarded as a 1D Bragg structure where cumulative Bragg reflection and phase condition determines the lasing modes of the structure.

Despite those two lasers' wide use in optical communication networks, the existing issues such as feedback interference vulnerability [6, 7] and re-growth caused high manufacturing cost still need to be solved for more applications in either the next generation fibre-to-the-home optical network deployments [1] or the high-speed telecommunication upgrades [8]. To address those critical problems, we need to explore structures that can retain the advantage of feedback immunization from FP lasers [9], while suppressing the undesired side-modes of FP longitudinal cavity, to make the laser working at single-mode condition with high spectral purity. The following subsections include more detailed descriptions of the FP, DBR and DFB lasers, correspondingly, to summarize their advantages, as well as the disadvantages so that we can improve.

1.1.1 Fabry-Perot Lasers

A Fabry-Perot laser is an optical resonator, in which two parallel end-facet mirrors are separated by a uniform amplifying medium, such that light of certain wavelengths traveling through this gain medium can be continuously amplified and extracted from the output facet. The reflection from end mirrors enables the traveling waves of opposite directions in the cavity to interfere with each other either constructively to set up a standing wave or destructively to cancel out on average over time. Once the wave set up inside the cavity, say of wavelength λ, then any other optical waves that are different by any integer number of the half-wavelength (λ/2) can be fit into the cavity, which makes the FP laser multi-mode. The schematic 1D structure of the FP laser is shown in Fig. 1.1.

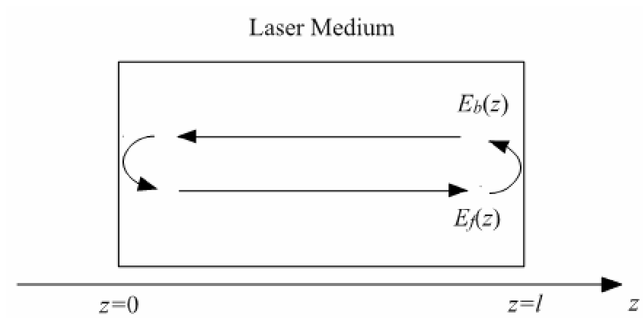

Figure 1.1 Fabry-Perot laser cavity and gain medium.

Therefore, the relation between the resonance wavelength λ and the longitudinal length L for an FP laser can be written as follows:

$$m\left(\frac{\lambda}{2n}\right) = L \tag{1.1}$$

, where *m* is an integer and *n* is the effective index of the FP cavity.

a) Lasing threshold

To analyse the threshold gain condition under which a pumped laser starts to emit light continuously, we have to find the balance between optical loss of the laser cavity and the wave amplification through its active region. In other words, to make the net optical power gain G_{op} equals unity, the initial optical power P_i should be equal to the power P_f after a round trip as

$$G_{op} = P_f / P_i = 1 \tag{1.2}$$

This process includes two end-facet mirror reflections r_1, r_2 and a uniform medium amplification of length L as

$$r_1 r_2 \exp\left[-j2kL\right] = 1 \tag{1.3}$$

,where the longitudinal wave vector k is as

$$k = \beta - j\frac{1}{2}\left(g - \alpha\right) \tag{1.4}$$

Here, β is the propagation constant, g is the material gain and α is the material loss. By plugging k back into Eq. (1.3), we can find the lasing threshold condition for FP laser as

$$g = \alpha + \frac{1}{L}\ln\left(\frac{1}{r_1 r_2}\right) \tag{1.5}$$

and

$$2\beta L = 2m\pi\ . \tag{1.6}$$

b) Spectrum

As described before for resonance condition of the FP cavity, we can see from the following plot, Fig. 1.2, that the FP lasers are intrinsically multi-mode, with mode spacing as given by $\Delta\lambda = \frac{\lambda^2}{2nL}$. And the lasing spectrum is determined by the material gain profile, as well as level of the injection pumping power.

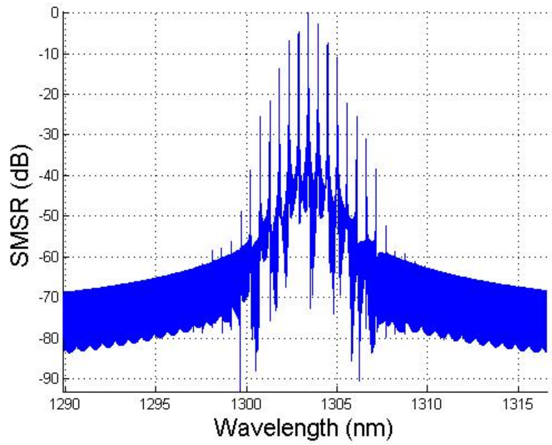

Figure 1.2 FP laser output spectrum.

c) Noise

As we see, Fabry-Perot lasers are the simplest and most economical type of semiconductor laser diodes, but they are generally noisier than DBR and DFB, because carriers in the active layer are shared by a large number of supported longitudinal modes who can compete with each other to obtain energy from the carriers for photon emissions. Then, the mode competition will cause mode partition noise (MPN) and affects the relative intensity noise (RIN) and bit-error rate (BER) during transmission through fiber. The following figures, Fig. 1.3-1.4, are plots for the carrier density, photon number, output power distribution and RIN calculations carried out using a multi-mode time-domain rate equation simulation. From the graphs, we can see that the mode competition can sometimes seriously affect the stable operation of the FP lasers, especially for their use in fibre optic communications.

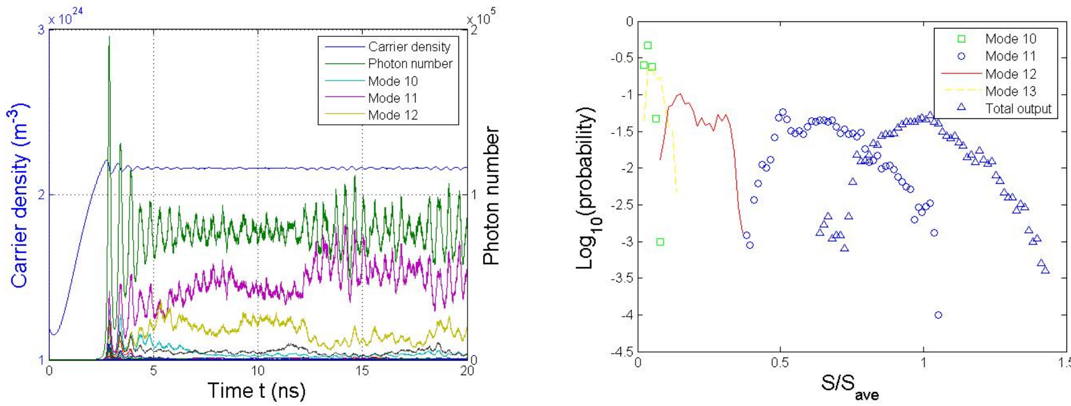

Figure 1.3 FP laser carrier and photon in CW case; photon distribution

In Fig. 1.3, the MPN of FP is shown to be heavily affecting the lasing output, which, under long distance fiber transmission, could lead to further distortion of the signal, as there will be serious overlap of the signal bits, known as intersymbol interferences (ISI) for optical waves of different wavelengths. For a reliable signal source in optical communications, the main mode should have the same photon distribution as the total output, while all other side modes should have an exponential decay around 0 for S/S_{ave}. The RIN plot of Fig. 1.4 is also indicating the high level of noise for their relative magnitude to be around -30 ~ -35 dB.

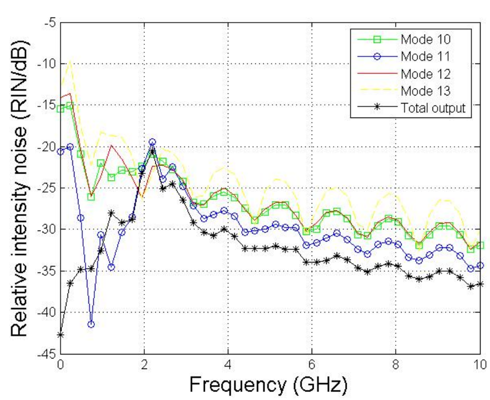

Figure 1.4 FP laser RIN for different modes.

d) Large signal

For large signal demonstration, we also showed the time-domain simulation of FP laser modulated by square wave current injection switched between 30-50 mA at 5GB/s. For short range communications, multi-mode FP laser can still be used depending on the transmission quality required.

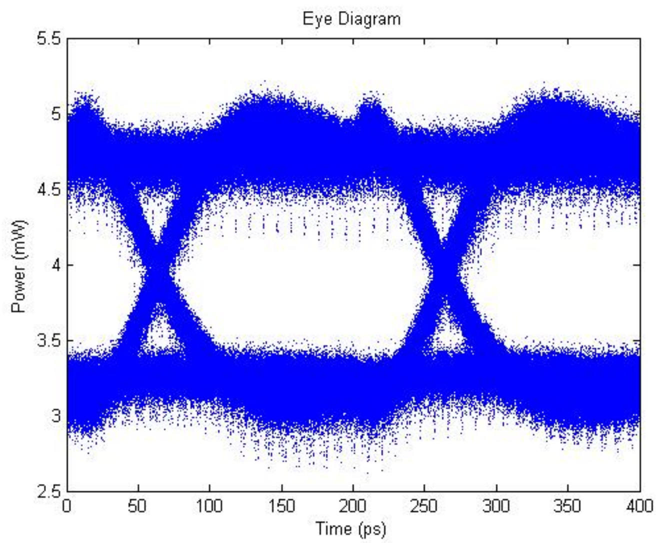

Figure 1.5 FP laser large signal eye diagram

1.1.2 Distributed Bragg Reflection Lasers

To narrow down the output spectrum and reduce the mode numbers, DBR [4, 10] laser is designed as shown in Fig. 1.6 schematically. Two passive Bragg gratings of lengths L_1 and L_3 with periodic indice are separated by a gain region of length L_2. The gratings serve as frequency-selective mirrors, whose reflectivity diagram with respect to the wavelength can be given by Fig. 1.7.

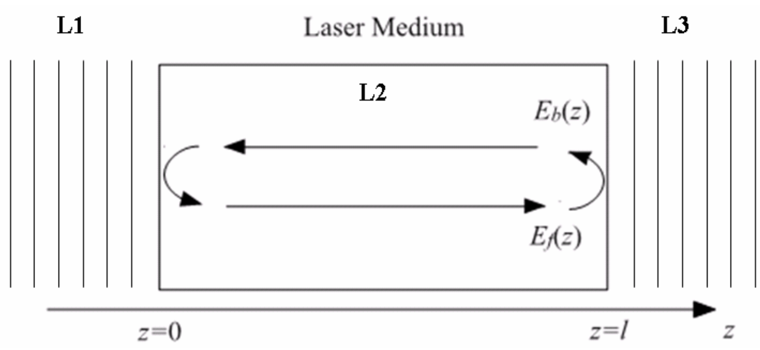

Figure 1.6 DBR laser cavity and gain medium.

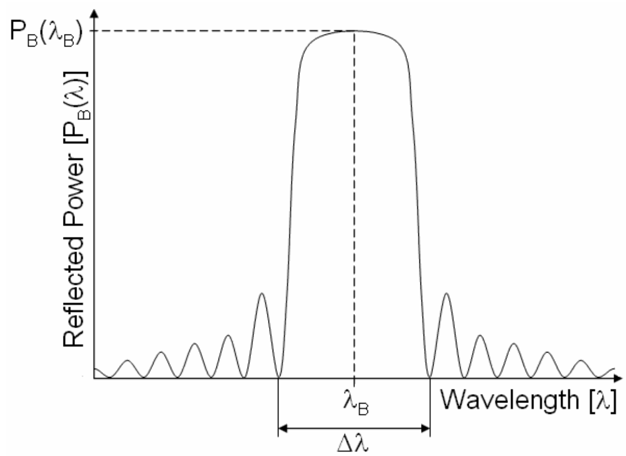

Figure 1.7 DBR laser reflection spectrum.

A number of longitudinal modes with spacing $\Delta\lambda = \lambda^2 / 2nL$ can be supported within the grating's stop band, while all other modes outside the stop band decay exponentially in the passive gratings. The Bragg mirror, often a stack of quarter-wave gratings, is then used to provide the maximum amount of reflection around the Bragg wavelength for mode selection. When the cavity length is reduced, resonance wavelength λ will increase until only one longitudinal mode is allowed at λ_B. Then, a single-mode DBR laser is obtained. There are also other ways to make single-mode DBR lasers by tuning the cladding parameters, etc., but we will not explain here in details in this thesis.

For analytical solution of the structure's lasing threshold condition, we can use the effective reflectivity r_{eff} ($= C \cdot r_g$) for the Bragg mirror [10], instead of FP facet reflectivity r, in the previous Eq. (1.3) as

$$r_{eff}^2 \exp\left[-j2kL\right] = 1 \qquad (1.7)$$

, which, by separating the complex reflectivity and wave number into real and imaginary parts, can lead to the following phase and gain equation as

$$g = \alpha + \frac{1}{L}\ln\left(\frac{1}{C^2\left|r_g\right|^2}\right) \qquad (1.8)$$

and

$$2\beta L + \phi = 2m\pi\ . \qquad (1.9)$$

Here, C is the coupling-efficiency coefficient of the DBR laser from the active region to the passive Bragg mirror, r_g is the amplitude-reflection coefficient of the mirror at the transition point, and ϕ is the phase of r_g [10].

Single-mode DBR laser diodes are often wavelength-tunable, which can be accomplished by using a separate phase section, as in Fig. 1.8, heated by the driving current electrically. In general, the refractive index decreases with an increase in the carrier density, (or injected current), resulting in a blue shift of the Bragg wavelength and therefore the lasing wavelength. This kind of multi-section current injection scheme can achieve continuous wavelength tuning over a range of 5-20 nm [11]. There are also more sophisticated device designs, exploiting sampled gratings (SG-DBR laser) [12], which offer a tuning range as wide as e.g. 40 nm, although with certain possibilities of the mode hopping.

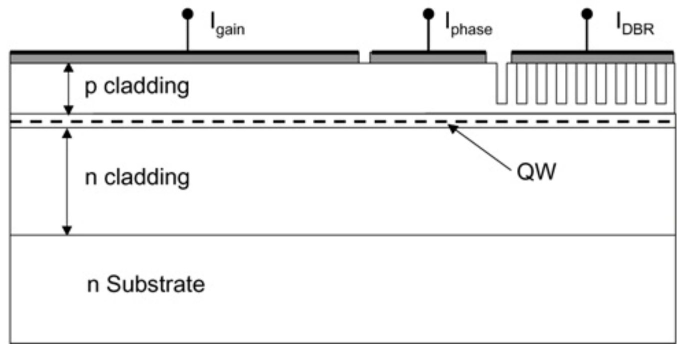

Figure 1.8 DBR laser structure with separate gain and phase tuning sections.

The linewidth of a DBR laser is typically a few megahertz [13], which is larger than that, for example, of a coupled-cavity laser [14], because of the former one's relatively short resonance cavity. For any FP structure, linewidth of the resonator can be much narrower than that of the Bragg reflectors.

Vertical cavity surface-emitting lasers (VCSELs) [15-17] are also distributed Bragg reflector lasers, although the term "DBR laser diodes" is normally used for edge-emitting semiconductor lasers. This structure can be formed by epitaxially growing periodic layers onto the wafer substrate to obtain Bragg reflectors in the vertical direction, such that waves in the sandwiched active layer can achieve resonance at any desired wavelength.

Applications of DBR laser diodes include optical fiber communications [18], free-space optical communications [19], laser cooling [20, 21], optical metrology and sensors

[22, 23], and high-resolution spectroscopy [24, 25]. DBR lasers actually compete with external-cavity diode lasers, which also offer wavelength-tunable single-frequency output, with potentially better performance in terms of noise control, but requiring a significantly more complex setup [26].

1.1.3 Distributed Feedback Lasers

A distributed-feedback laser [3, 5] is also a Bragg grating assisted structure, whose periodic etchings sit right above the active layer along the longitudinal direction, to achieve accumulative Bragg reflections and lasing when threshold gain and phase conditions are met. The end-facet mirror can also be omitted or coated with anti-reflective layers to minimize the facet reflection and perturbations back into the laser structure. Typically, for high purity single-mode DFB laser, the periodic structure is modified with an additional $\lambda/4$ -phase shift region in the middle [27], such that the constructive interference condition can be met at the reflection spectrum peak center, rather than two sides of the main lobe as in the non-shifted DFB case.

a) Lasing threshold

For the threshold gain analysis of a DFB structure, we can use the boundary condition at two ends as

$$A(0) = r_1 B(0) \text{ and } B(L) = r_2 A(L)\,. \tag{1.10}$$

Then, by plugging in the expression for A and B from the coupled-mode equation as

$$\begin{aligned} A(z) &= A_1 \exp(iqz) + r(q) B_2 \exp(-iqz) \\ B(z) &= B_2 \exp(-iqz) + r(q) A_1 \exp(iqz) \end{aligned} \tag{1.11}$$

, where $r(q)$ and q are the effective-reflection coefficient and wave number, we can get the threshold equation for the laser as

$$\left(\frac{r_1 - r}{1 - rr_1}\right)\left(\frac{r_2 - r}{1 - rr_2}\right)\exp(2iqL) = 1\,. \tag{1.12}$$

Since $r(q)$ and q are both related to the wave number difference $\Delta\beta\left(=\beta-\beta_B\right)$ and coupling coefficient κ as

$$r(q) = \frac{q - \Delta\beta}{\kappa} \tag{1.13}$$

and

$$q = \pm\left[\left(\Delta\beta\right)^2 - \kappa^2\right]^{1/2} \tag{1.14}$$

, we can obtain a similar solution as plotted in the following figure [3] as

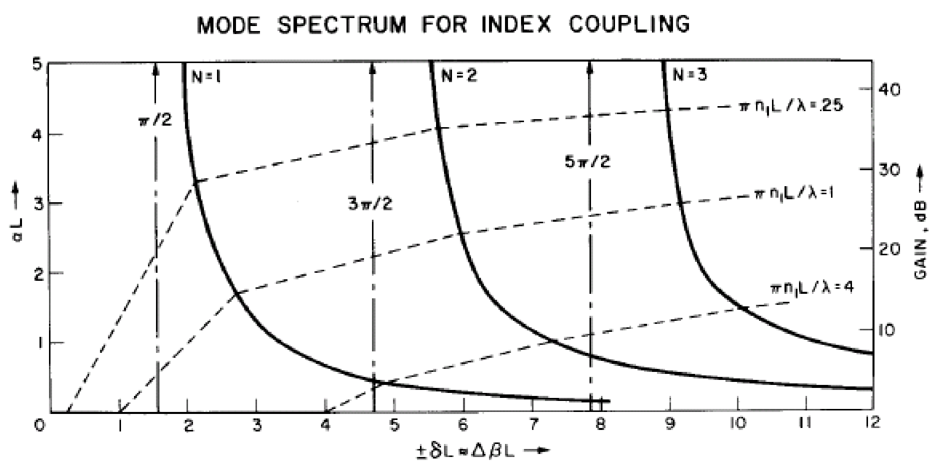

Figure 1.9 Normalized threshold gain and detuning for three modes of an anti-reflection coated DFB laser [3]

,where the detuning factor is $\delta = \mathrm{Re}\left[\Delta\beta\right]$ and the threshold gain is $\alpha = 2*\mathrm{Im}\left[\Delta\beta\right]$.

Therefore, a single-mode operation can be obtained with proper choice of the grating depth, device length and facet reflectivities, as indicated by the dashed lines in Fig. 1.9.

b) Spectrum

The spectrum of DFB laser is usually single-mode with high SMSR (around 50 dB as in Fig. 1.10), whose mode spacing is similar to FP mode as $\Delta\lambda = \lambda^2 / 2nL$. The first side-mode of a non-shifted DFB laser usually sits 1~3 nm away from the main mode, and is often the most common mode-hopping wavelength spot, as is determined by the intrinsic feature of the DFB structure. The threshold gain profile should be theoretically symmetric with respect to the Bragg wavelength, if no asymmetric factors are introduced into the laser at all during its fabrication process.

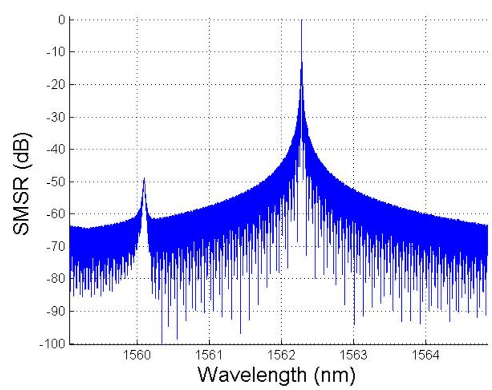

Figure 1.10 DFB laser output spectrum.

c) Noise

DFB laser usually works in the single mode condition with high SMSR, such that its MPN and RIN are relatively low, and may only be subject to certain levels of external feedback interferences. When DFB laser is used in the optical networks, isolator is always accompanied to prevent reflected feedbacks from re-entering the laser's structure and breaking the already built-up resonance condition. In the following Fig. 1.11, we could see that a level of -25dB feedback can dramatically increase the noise level of the laser output from the black curve to the red one.

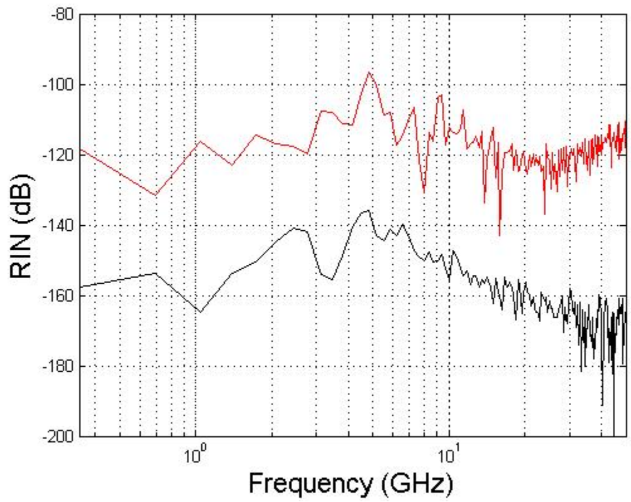

Figure 1.11 DFB laser with/without external feedback interferences.

This can be understood as there are complicated constructive interferences established in the DFB cavity between those thousands of gratings, such that a certain level of external perturbations can easily disturb the whole system before the phase resonance condition can be re-established.

d) Large signal direct modulation

The DFB laser can still be stable for single-mode lasing at high modulation speed, so it is always used in the central office for long-haul communications, because of its supreme lasing quality, but relatively higher cost. The following figure, Fig. 1.12, shows a clean eye-diagram at 5 Gbit/s modulation, without external feedback interferences.

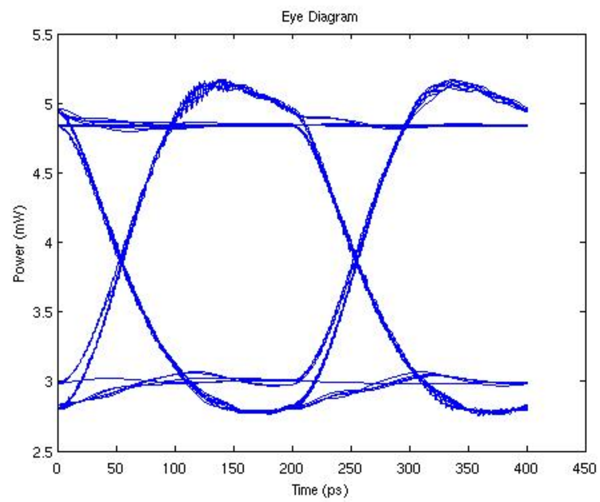

Figure 1.12 DFB laser eye-diagram at 5Gbit/s.

1.2 Motivation of the Research

To reduce the feedback caused signal quality deterioration, without resorting to the optical isolators, we wish to design lasers that can combine the simplicity of FP cavity together with the frequency-selective transversely placed Bragg mirrors, to obtain single longitudinal mode lasing at any desired wavelength. Our Bragg reflection waveguide (BRW) laser design is one of the choices, which not only enables the single-mode lasing, but also provides light confinement in the low index gain medium, such that materials like the silicon-rich SiO_x can be directly integrated onto the Si-substrate and be used as a light source for the all-in-one optical components board.

Also, considering the design that can use only a few defects etched along the FP cavity's longitudinal direction to achieve single mode lasing with high SMSR, we wish to study the discrete mode (DM) laser of its dynamic properties, as well as performances over the spectral purity and feedback sensitivity issues, under the high-speed direct modulation conditions.

1.3 Outline of the Thesis

This thesis is organized as follows. We will describe the basic theory about transfer matrix method for waveguide with detailed transverse structures. Then, we discuss the 1D band structure of Bragg reflection waveguide, which can be directly extended to the design of Bragg reflection waveguide (BRW) lasers. Then we explain the properties of BRW laser. In Chapter 5, we will discuss the transfer matrix method applied to the FP cavity's longitudinal direction and therefore explain the design of discrete mode (DM) laser structure. Following that, we will discuss the time-domain traveling wave model, which can be used for large signal simulation of many customized laser structures, especially non-periodic ones. Then, we discuss the properties of DM laser under high-speed direct modulation conditions and explain the procedures we can follow to improve its dynamic performances.

Chapter 2

Transfer Matrix Method

In this chapter, we will explain the method that has been used to investigate the one-dimensional (1D) waveguide structure by forming a chain of multiplied transfer matrices according to the boundary conditions of the electromagnetic fields at the interfaces. The transferring of waves at each point of the 1D waveguide can be uniquely determined by using their phase information, such that an ordinary 2-by-2 matrix can be formed piecewisely. With the help of computers, many complex chain of matrix algebra can be easily handled for a final solution of the waveguide modes.

2.1 Introduction

The transfer matrix method is designed to deal with propagations of optical waves in the layered media. Theoretically, electric and magnetic fields of the waves are all governed by the Maxwell's equations, which provide the background physics for the fields to be connected and calculated at different positions of the material, especially at the material interfaces. For our studies of the optical waves in most media, except for the metallic waveguides that utilize surface plasma polaritons [28] to carry on optical fields, we assume zero net electric charges to reside on the dielectric material interfaces. Then, for the waves at those discontinuities, we can obtain the scattering matrix by applying the electric and magnetic fields continuity condition at the interfaces. And for wave propagations in the uniform and lossless media, we can use the propagation matrix to describe. Having solved those two cases, i.e., the index jump and the uniform medium cases, we can be ready to deal with their combinations --- the layered media, for the design of waveguides and lasers in optical communication systems.

In the following subsections, we will briefly review the Maxwell's equations and the material equations as the starting point of the functional optoelectronic device descriptions and simulations.

2.2 Maxwell's Equations

The most fundamental equations in electrodynamics are the Maxwell's equations, which are given as follows:

$$\begin{array}{ll} \nabla\times\mathbf{E}+\dfrac{\partial\mathbf{B}}{\partial t}=0 & \quad \nabla\cdot\mathbf{D}=\rho \\ \nabla\times\mathbf{H}-\dfrac{\partial\mathbf{D}}{\partial t}=\mathbf{J} & \quad \nabla\cdot\mathbf{B}=0 \end{array}. \tag{2.1}$$

In the equations, **E** and **H** are the electric and magnetic field vectors, respectively, which are often used to describe an electromagnetic field. The quantities **D** and **B** are called the electric displacement and magnetic induction, respectively, which are introduced to include interactions between the field and the material. The quantities ρ and **J** are the electric charge and current density, respectively, which may be considered as sources of the fields **E** and **H**. These four Maxwell equations completely determine the propagation of electromagnetic field inside the medium and are the fundamental equations of the electrodynamics theory.

2.3 Wave equations

If we assume the electromagnetic field oscillates at a single angular frequency ω, we can write the field vector A as a function of space and time in frequency domain as

$$\mathbf{A}(\mathbf{r},t) = \mathrm{Re}\left[\overline{\mathbf{A}}(\mathbf{r})\exp\left(j\omega t\right)\right], \tag{2.2}$$

where **A** can represent the electric field **E**, the magnetic field **H**, the electric flux density **D**, and the magnetic flux density **B**, respectively. Then, for dielectric medium in absence of the surface current or surface charges, we can rewrite the Maxwell's equations in frequency domain as

$$\begin{aligned} &\nabla\times\mathbf{E} = -j\omega\mathbf{B} = -j\omega\mu_0\mathbf{H} \qquad && \nabla\cdot\left(\varepsilon_r\varepsilon_0\mathbf{E}\right) = 0 \\ &\nabla\times\mathbf{H} = -j\omega\mathbf{D} = j\omega\varepsilon_r\varepsilon_0\mathbf{E} \qquad && \nabla\cdot\left(\mu_0\mathbf{H}\right) = 0 \end{aligned} \tag{2.3}$$

where we assumed $\mathbf{B} = \mu_r\mu_0\mathbf{H} = \mu_0\mathbf{H}$ (i.e., $\mu_r = 1$) and $\mathbf{D} = \varepsilon_r\varepsilon_0\mathbf{E}$

2.3.1 Wave equation for electric field E

Applying a vectorial rotation operation $\nabla\times$ to the above equation, we can get

$$\nabla\times\left(\nabla\times\mathbf{E}\right) = \nabla\left(\nabla\cdot\mathbf{E}\right) - \nabla^2\mathbf{E} = -j\omega\mu_0\nabla\times\mathbf{H}\,. \tag{2.4}$$

With the help of equations $\nabla\cdot\left(\varepsilon_r\mathbf{E}\right) = \nabla\varepsilon_r\cdot\mathbf{E} + \varepsilon_r\nabla\cdot\mathbf{E} = 0$ and $\nabla\times\mathbf{H} = j\omega\varepsilon_r\varepsilon_0\mathbf{E}$, we can reduce the above equation to contain only the electric field as

$$\nabla^2\mathbf{E} + \nabla\left(\frac{\nabla\varepsilon_r}{\varepsilon_r}\cdot\mathbf{E}\right) + k^2\mathbf{E} = 0 \tag{2.5}$$

, where k is the wave number in that medium as $k = k_0 n = k_0\sqrt{\varepsilon_r} = \omega\sqrt{\varepsilon_r\varepsilon_0\mu_0}$.

For uniform medium with constant relative permittivity ε_r, the vectorial wave equation for the electric field can be reduced to the Helmholtz equation as

$$\nabla^2\mathbf{E} + k^2\mathbf{E} = 0 \tag{2.6}$$

2.3.2 Wave equation for magnetic field H

Applying a vectorial rotation operation $\nabla\times$ to Eq. (2.3), we get

$$\nabla\times(\nabla\times\mathbf{H}) = \nabla(\nabla\cdot\mathbf{H}) - \nabla^2\mathbf{H} = j\omega\varepsilon_0\nabla\times(\varepsilon_r\mathbf{E}). \tag{2.7}$$

With the help of equations $\nabla\times(\varepsilon_r\mathbf{E}) = \nabla\varepsilon_r\times\mathbf{E} + \varepsilon_r\nabla\times\mathbf{E} = 0$ and $\nabla\times\mathbf{E} = -j\omega\mu_0\mathbf{H}$, we can simplify the above equation to contain only the magnetic field as

$$\nabla^2\mathbf{H} + \frac{\nabla\varepsilon_r}{\varepsilon_r}\times(\nabla\times\mathbf{H}) + k_0^2\varepsilon_r\mathbf{H} = 0. \tag{2.8}$$

If the relative permittivity ε_r is constant in the medium, the above equation can also be reduced to the Helmholtz equation as

$$\nabla^2\mathbf{H} + k^2\mathbf{H} = 0. \tag{2.9}$$

2.4 Boundary conditions

One of the most important problems in determination of the reflection and transmission for the electromagnetic waves through layered medium is the continuity relation of the field components at dielectric interfaces. Although physical properties may change abruptly across the layers, some of the field components are continuous at the dielectric boundaries. These continuity equations can be derived directly from the Maxwell's equations.

Consider an interface separating two media with different dielectric permittivities and permeabilities: If we construct a thin cylinder over a unit area of the surface and carry out the surface integral, we can obtain the boundary conditions for **B** and **D** as follows

$$\mathbf{n}\cdot(\mathbf{B}_2-\mathbf{B}_1)=0 \qquad \mathbf{n}\cdot(\mathbf{D}_2-\mathbf{D}_1)=\sigma \tag{2.10}$$

In the above equations, **n** is the unit normal to the surface directed from medium 1 into medium 2, and σ is the surface charge density. They can also be written as

$$B_{2n}=B_{1n} \qquad D_{2n}-D_{1n}=\sigma\,. \tag{2.11}$$

For the boundary condition of field vector E and H, we can draw a rectangular contour with their two longer sides parallel to the boundary and carry out a contour integral to obtain the following equaitons as:

$$\mathbf{n}\times(\mathbf{E}_2-\mathbf{E}_1)=0 \qquad \mathbf{n}\times(\mathbf{H}_2-\mathbf{H}_1)=J_s \tag{2.12}$$

, where J_s is the surface current density. Again, the above can be rewritten as

$$E_{2t}=E_{1t} \qquad H_{2t}-H_{1t}=J_s \tag{2.13}$$

, where t represents the tangential component of the field vector.

Thus, the boundary condition of electromagnetic fields in the dielectric media can be summarized as follows:

(a) Tangential components of the electric fields are continuous as

$$E_{1t}=E_{2t} \tag{2.14}$$

(b) Tangential components of the magnetic fields are continuous, if no current flows at the interface surface, as

$$H_{1t} = H_{2t}\,. \tag{2.15}$$

(c) Normal components of the electric flux density are continuous, if no charge resides at the interface surface, as

$$D_{1n} = D_{2n} \tag{2.16}$$

(d) Normal components of the magnetic flux densities are continuous as

$$B_{2n} = B_{1n}\,. \tag{2.17}$$

2.5 Transfer matrix method formulation

With the above discussions for the Maxwell's equations and the boundary conditions of the dielectric materials, we can construct the transfer matrix to describe wave propagations in the layered media. Following, we will use a three-layer slab waveguide as an example to introduce the TE and TM modes:

The slab index profile can be written as follows

$$n(x) = \begin{cases} n_1, & x < 0 \\ n_2, & 0 < x < d \\ n_3, & x > d \end{cases} \tag{2.18}$$

where n_1, n_2, and n_3 are the refractive indices and d is the thickness of the middle layer. Since the structure is one-dimensional, i.e., homogeneous in the y and z direction, and the wave is propagating along the z-axis in xz plane, therefore, $\frac{\partial}{\partial y} = 0$ and $\frac{\partial}{\partial z} = -j\beta$.

From the Maxwell's equations

$$\begin{aligned} \nabla \times \mathbf{E} &= -j\omega\mu_0 \mathbf{H} \\ \nabla \times \mathbf{H} &= j\omega\varepsilon_r\varepsilon_0 \mathbf{E} \end{aligned} \tag{2.19}$$

whose component representation can be written as follows

$$\begin{aligned} \frac{\partial}{\partial y}E_z - \frac{\partial}{\partial z}E_y &= -j\omega\mu_0 H_x \\ \frac{\partial}{\partial z}E_x - \frac{\partial}{\partial x}E_z &= -j\omega\mu_0 H_y \\ \frac{\partial}{\partial x}E_y - \frac{\partial}{\partial y}E_x &= -j\omega\mu_0 H_z \end{aligned} \tag{2.20}$$

$$\begin{aligned} \frac{\partial}{\partial y}H_z - \frac{\partial}{\partial z}H_y &= j\omega\varepsilon_0\varepsilon_r E_x \\ \frac{\partial}{\partial z}H_x - \frac{\partial}{\partial x}H_z &= j\omega\varepsilon_0\varepsilon_r E_y \\ \frac{\partial}{\partial x}H_y - \frac{\partial}{\partial y}H_x &= j\omega\varepsilon_0\varepsilon_r E_z \end{aligned} \tag{2.21}$$

Thus, we can have two modes as solutions of the above equations, i.e., the transverse electric (TE) mode and transverse magnetic (TM) mode that propagate in the three-layer slab waveguide.

For the TE mode, longitudinal component of the electric field is zero ($E_z = 0$), then, Eq. (2.20) and $\frac{\partial}{\partial y} = 0$ give the relation $H_y = 0$ and $E_x = 0$. The above six equations are therefore reduced to one Helmholtz equation, one 1st and one 0th order rate equations as

$$\begin{aligned}
&\frac{\partial^2}{\partial x^2}E_y+\left(n^2k_0^2-\beta^2\right)E_y=0\\
&H_z=-\frac{1}{j\omega\mu_0}\frac{\partial E_y}{\partial x}\\
&H_x=-\frac{\beta}{\omega\mu_0}E_y
\end{aligned} \quad . \tag{2.22}$$

For the TM mode, longitudinal component of the magnetic field is zero ($H_z=0$), then, Eq. (2.21) and $\frac{\partial}{\partial y}=0$ give the relation $E_y=0$ and $H_x=0$. The six equations can also be reduced to one Helmholtz equation, one 1st and one 0th order rate equations as

$$\begin{aligned}
&n^2\frac{\partial}{\partial x}\left(\frac{1}{n^2}\frac{\partial}{\partial x}H_y\right)+\left(n^2k_0^2-\beta^2\right)H_y=0\\
&E_z=\frac{1}{j\omega\varepsilon_r\varepsilon_0}\frac{\partial H_y}{\partial x}\\
&E_x=\frac{\beta}{\omega\varepsilon_r\varepsilon_0}H_y
\end{aligned} \tag{2.23}$$

This is one important property of the 1D multilayer, which splits the problem into two independent ones as TE and TM polarizations, respectively.

2.5.1 Introduce the transfer matrix for TE mode

As we know, the field $E_{iy}(x)$ satisfying TE wave equations in the *i*-th layer (*i*=1,2, and 3) has the following form of two (forward and backward) traveling waves as

$$E_{iy}(x)=a_ie^{-jk_{ix}x}+b_ie^{+jk_{ix}x}=A_i(x)+B_i(x) \tag{2.24}$$

, where

$$k_{ix}=\sqrt{(n_ik_0)^2-\beta^2} \tag{2.25}$$

is the x-component of the wave vector in the ith layer, and a_i, b_i are the amplitude constants in each layer.

In terms of the matrix representation, we can write

$$E_{iy}(x) = \begin{pmatrix} A_i(x) \\ B_i(x) \end{pmatrix} = \begin{pmatrix} e^{-jk_{ix}x} & 0 \\ 0 & e^{+jk_{ix}x} \end{pmatrix} \begin{pmatrix} a_i \\ b_i \end{pmatrix} \tag{2.26}$$

, for the field propagation in the uniform medium i.

For the fields scattered at interfaces between the layers, we need to apply their boundary condition by requiring the field components $E_{iy}(x)$ and $H_{iz}(x)\left(= \frac{j}{\omega\mu_0} \frac{\partial E_{iy}}{\partial x} \right)$ to be continuous as

$$E_{iy}(x) = a_i e^{-jk_{ix}x} + b_i e^{+jk_{ix}x} = E_{(i+1)y}(x) = a_{i+1} e^{-jk_{(i+1)x}x} + b_{i+1} e^{+jk_{(i+1)x}x} \tag{2.27}$$

$$\frac{j}{\omega\mu_0} \frac{\partial}{\partial x} E_{iy}(x) = \frac{j}{\omega\mu_0} \frac{\partial}{\partial x} E_{(i+1)y}(x) \tag{2.28}$$

The second equation can be written more explicitly as

$$a_i k_{ix} e^{-jk_{ix}x} - b_i k_{ix} e^{+jk_{ix}x} = a_{i+1} k_{(i+1)x} e^{-jk_{(i+1)x}x} - b_{i+1} k_{(i+1)x} e^{+jk_{(i+1)x}x} \tag{2.29}$$

In terms of the matrix representation, we can write

$$\begin{pmatrix} e^{-jk_{ix}x} & e^{+jk_{ix}x} \\ k_{ix} e^{-jk_{ix}x} & -k_{ix} e^{+jk_{ix}x} \end{pmatrix} \begin{pmatrix} a_i \\ b_i \end{pmatrix} = \begin{pmatrix} e^{-jk_{(i+1)x}x} & e^{+jk_{(i+1)x}x} \\ k_{(i+1)x} e^{-jk_{(i+1)x}x} & -k_{(i+1)x} e^{+jk_{(i+1)x}x} \end{pmatrix} \begin{pmatrix} a_{i+1} \\ b_{i+1} \end{pmatrix} \tag{2.30}$$

, which can be split into a scattering matrix multiplying a propagation matrix as

$$\begin{pmatrix} 1 & 1 \\ k_{ix} & -k_{ix} \end{pmatrix} \begin{pmatrix} e^{-jk_{ix}x} & 0 \\ 0 & e^{+jk_{ix}x} \end{pmatrix} \begin{pmatrix} a_i \\ b_i \end{pmatrix} \tag{2.31}$$

Therefore, we can define the “propagation” and “scattering” matrices for the TE mode as

$$P_i = \begin{pmatrix} e^{-jk_{ix}x} & 0 \\ 0 & e^{+jk_{ix}x} \end{pmatrix} \tag{2.32}$$

$$D_i = \begin{pmatrix} 1 & 1 \\ k_{ix} & -k_{ix} \end{pmatrix}. \tag{2.33}$$

2.5.2 Introduce the transfer matrix for TM mode

For the field $H_{iy}(x)$ satisfying TM wave equations in the *i*-th layer (*i*=1, 2, and 3), we have the forward and backward traveling waves combined as

$$H_{iy}(x) = a_i e^{-jk_{ix}x} + b_i e^{+jk_{ix}x} = A_i(x) + B_i(x) \tag{2.34}$$

, where

$$k_{ix} = \sqrt{(n_i k_0)^2 - \beta^2} \tag{2.35}$$

is the x-component of the wave vector in the *i*th layer, and a_i, b_i are the amplitude constants in each layer.

In terms of the matrix representation, we can still write

$$H_{iy}(x) = \begin{pmatrix} A_i(x) \\ B_i(x) \end{pmatrix} = \begin{pmatrix} e^{-jk_{ix}x} & 0 \\ 0 & e^{+jk_{ix}x} \end{pmatrix} \begin{pmatrix} a_i \\ b_i \end{pmatrix} \tag{2.36}$$

, for the field propagation in the uniform medium *i*.

For the field scattered at interfaces between the layers, we need to apply their boundary condition by requiring the components $H_{iy}(x)$ and $E_{iz}(x)\left(= -\frac{j}{\omega\varepsilon_r\varepsilon_0}\frac{\partial H_{iy}}{\partial x} \right)$ to be continuous as

$$H_{iy}(x) = a_i e^{-jk_{ix}x} + b_i e^{+jk_{ix}x} = H_{(i+1)y}(x) = a_{i+1} e^{-jk_{(i+1)x}x} + b_{i+1} e^{+jk_{(i+1)x}x} \tag{2.37}$$

$$-\frac{j}{\omega\varepsilon_{ir}\varepsilon_0}\frac{\partial}{\partial x}H_{iy}(x) = -\frac{j}{\omega\varepsilon_{(i+1)r}\varepsilon_0}\frac{\partial}{\partial x}H_{(i+1)y}(x) \tag{2.38}$$

The second equation can be written more explicitly as

$$a_i\frac{k_{ix}}{\varepsilon_{ir}}e^{-jk_{ix}x} - b_i\frac{k_{ix}}{\varepsilon_{ir}}e^{+jk_{ix}x} = a_{i+1}\frac{k_{(i+1)x}}{\varepsilon_{(i+1)r}}e^{-jk_{(i+1)x}x} - b_{i+1}\frac{k_{(i+1)x}}{\varepsilon_{(i+1)r}}e^{+jk_{(i+1)x}x} \tag{2.39}$$

In terms of the matrix representation, we can write

$$\begin{pmatrix} e^{-jk_{ix}x} & e^{+jk_{ix}x} \\ \frac{k_{ix}}{\varepsilon_{ir}}e^{-jk_{ix}x} & -\frac{k_{ix}}{\varepsilon_{ir}}e^{+jk_{ix}x} \end{pmatrix}\begin{pmatrix} a_i \\ b_i \end{pmatrix} = \begin{pmatrix} e^{-jk_{(i+1)x}x} & e^{+jk_{(i+1)x}x} \\ \frac{k_{(i+1)x}}{\varepsilon_{(i+1)r}}e^{-jk_{(i+1)x}x} & -\frac{k_{(i+1)x}}{\varepsilon_{(i+1)r}}e^{+jk_{(i+1)x}x} \end{pmatrix}\begin{pmatrix} a_{i+1} \\ b_{i+1} \end{pmatrix} \tag{2.40}$$

, which can also be split into a scattering matrix multiplying a propagation matrix as

$$\begin{pmatrix} 1 & 1 \\ k_{ix}/\varepsilon_{ir} & -k_{ix}/\varepsilon_{ir} \end{pmatrix}\begin{pmatrix} e^{-jk_{ix}x} & 0 \\ 0 & e^{+jk_{ix}x} \end{pmatrix}\begin{pmatrix} a_i \\ b_i \end{pmatrix} \tag{2.41}$$

Then, we define the "propagation" and "scattering" matrices for the TM mode as

$$P_i = \begin{pmatrix} e^{-jk_{ix}x} & 0 \\ 0 & e^{+jk_{ix}x} \end{pmatrix} \tag{2.42}$$

$$D_i = \begin{pmatrix} 1 & 1 \\ k_{ix}/\varepsilon_{ir} & -k_{ix}/\varepsilon_{ir} \end{pmatrix} \text{ or } D_i = \begin{pmatrix} 1 & 1 \\ k_{ix}/n_{ir}^2 & -k_{ix}/n_{ir}^2 \end{pmatrix} \tag{2.43}$$

2.6 Example

In the following example, we use the analytical method described above to calculate and plot the dispersion curve, main mode field distributions and effective index profiles at 1.55 μm wavelength for a slab waveguide. The core index is 2.0 and cladding index is 1.0. The core width is 100 nm.

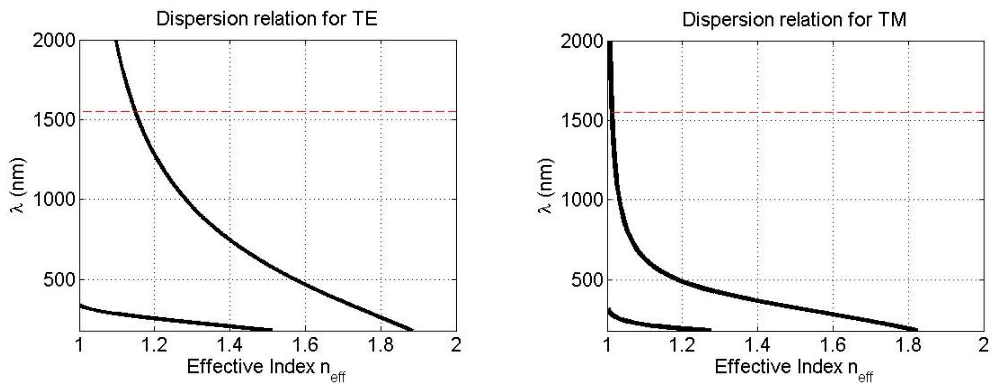

Figure 2.1 Dispersion curves for TE and TM waves of a 3-layer slab waveguide.

From Fig. 2.1, we see the dispersion curves take different shapes for TE and TM waves insed the 3-layer slab waveguide, which is due to the different boundary conditions at the index interfaces. In Fig. 2.2, the fields plot for both TE and TM are more obvious as we see the wider distribution of fields outside the core into the cladding.

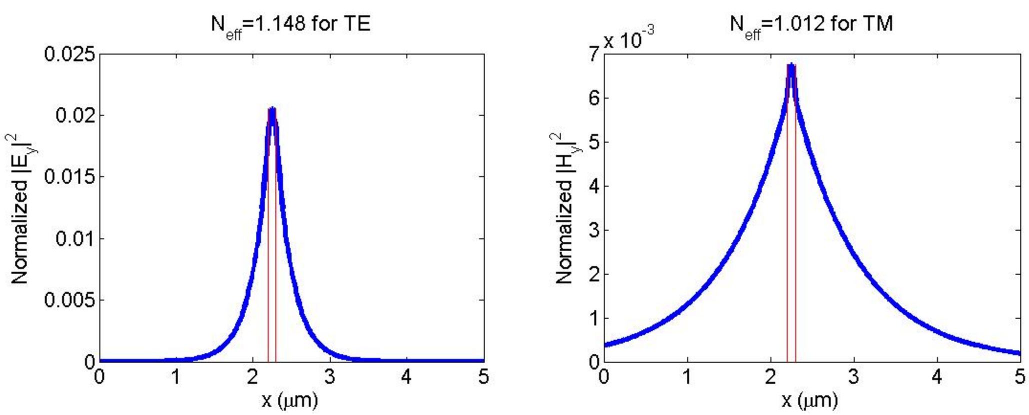

Figure 2.2 Main mode field distribution for TE and TM waves of a 3-layer slab waveguide..

In Fig. 2.3, we see the single-guided fundamental modes for both the TE and TM waves are on the real axis, while all other leaky modes are in the complex plane below the real x-axis.

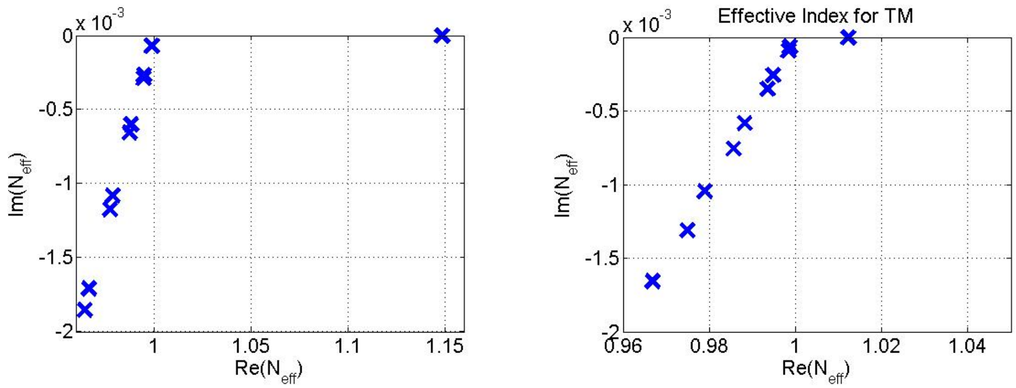

Figure 2.3 Index profile for TE and TM waves of a 3-layer slab waveguide.

2.7 Summary

In this chapter, we have discussed the basic theories of the electromagnetic waves in the dielectric medium, and derived the formula for the transfer matrix method to describe the multilayer structure. By cascading corresponding propagation and scattering matrices of the wave from one end to the other throughout the media, we can solve the equation in matrix form and obtain possible modes, or standing wave pattern, of the structure, with proper boundary conditions of the two ends.

Chapter 3

Multilayer medium and the Bragg reflector

After having introduced the transfer matrix method for optical waves in a general media, we now come to this chapter to discuss more specific cases such as the multilayer and periodic layer structures. Periodic layered media are a special class of multilayer structure in which dielectric materials of two (or more) different refractive indices are stacked together periodically. The simplest example of such medium would be a 1D Bragg reflector [29], in which there are two layers, with equal thicknesses, in each period, and the period repeats itself continuously to cascade along one direction through the structure. Wave propagations in these media will exhibit many special and potentially useful phenomena, which include Bragg reflection and optical stop bands, etc. In nature, many remarkable colors of the butterflies and fishes come from the light that is selectively reflected from those periodic patterns/shapes grown on their wings and skins. Artificially, we can also use many techniques, such as the molecular beam epitaxy, metal-organic chemical vapour phase deposition and atomic layer epitaxy, to make layered media grow periodically. In this chapter, we discuss the propagation of optical waves in these media, and discuss the main properties of the Bragg reflector.

3.1 Introduction

Propagation of the electromagnetic waves in periodic media has been studied intensively for its wide applications in optical fibre and laser designs. While light experiences Fresnel reflections from the dielectric interfaces, a periodic layered medium may be considered as an enhanced light reflector, where array of the interfaces accumulatively provide reflections for a certain wavelength, even though each individual interface is weak in back scattering.

An example from the experiment [29] would be the dielectric omni-reflector, as shown in Fig. 3.1. For both TE and TM waves incident on the left side of the air-material interface from normal to 10° angles, a wide range of wavelengths can be covered to have a reflectance of around 100%.

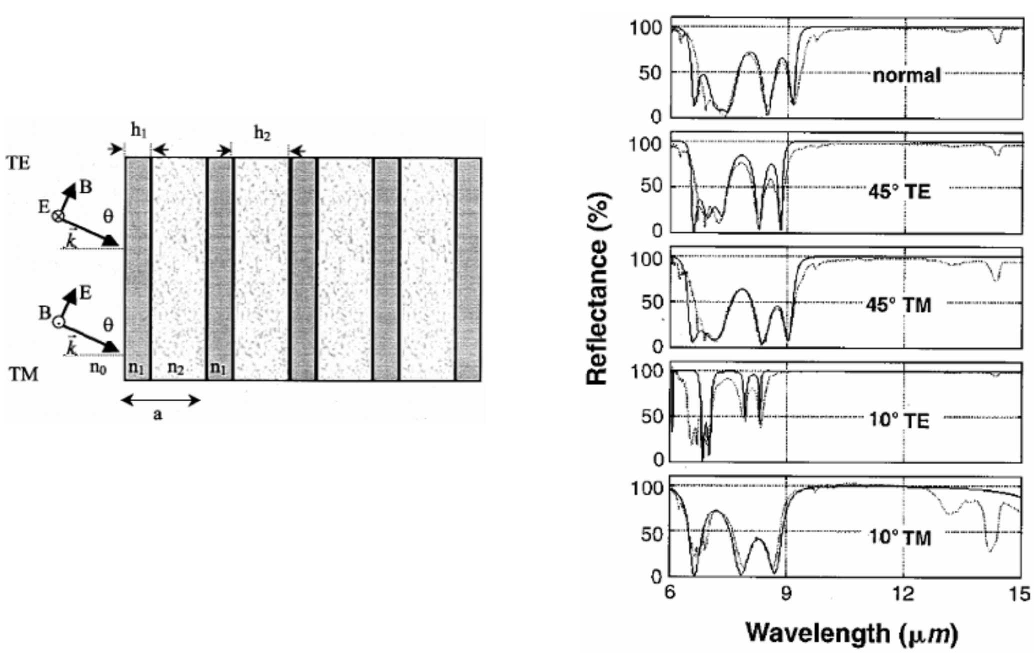

Figure 3.1 Structure and reflectance of a dielectric omni-reflector

This structure enables the fabrication of optical mirrors using a variety of dielectric materials, regardless of their refractive indices.

In the following subsections, we will study the propagation of electromagnetic waves in the multilayer medium and a simple periodic one, which consists of two alternating layers of dielectric materials with different refractive indices.

3.2 Transfer matrix for multilayer medium

A typical example of the multilayer medium can be shown in Fig. 3.2, where we take the *x* axis to be along the direction normal to the layers' interfaces. The materials are also assumed to be homogeneous and nonmagnetic $(\mu_r = 1)$ inside each layer.

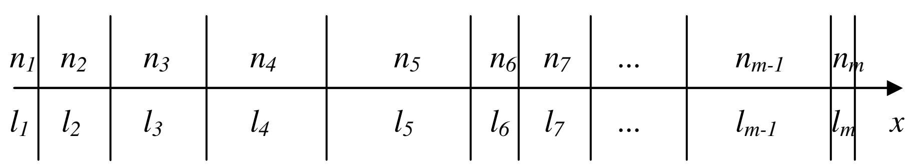

Figure 3.2 Structure of a multilayer medium.

The index of refraction profile is given by

$$n(x) = \begin{cases} n_1, & 0 < x < l_1 \\ \ldots & \\ n_m, & l_{m-1} < x < l_m \end{cases} \tag{3.1}$$

, where *n* and *l* are the index and thickness of each layer.

Here, we use the simplest structure, with "one" core layer, as an introductory example. To connect the electromagnetic waves in the slab media, we use the 2x2 matrix formulation derived in the previous chapter. By utilizing the continuity relation of corresponding field and its derivatives, we can obtain the forward and backward fields A_i and B_i through the scattering matrix D_i and the propagation matrix P_i as:

$$\begin{pmatrix} A_1 \\ B_1 \end{pmatrix} = D_1^{-1} D_2 \begin{pmatrix} A'_2 \\ B'_2 \end{pmatrix} \tag{3.2}$$

$$\begin{pmatrix} A'_2 \\ B'_2 \end{pmatrix} = P_2 \begin{pmatrix} A_2 \\ B_2 \end{pmatrix} \tag{3.3}$$

$$\begin{pmatrix} A_2 \\ B_2 \end{pmatrix} = D_2^{-1} D_3 \begin{pmatrix} A'_3 \\ B'_3 \end{pmatrix} \tag{3.4}$$

where

$$D_i = \begin{cases} \begin{pmatrix} 1 & 1 \\ \dfrac{k_{ix}}{k} & -\dfrac{k_{ix}}{k} \end{pmatrix} & \text{for TE wave} \\ \begin{pmatrix} \dfrac{k_{ix}}{kn_i} & \dfrac{k_{ix}}{kn_i} \\ n_i & -n_i \end{pmatrix} & \text{for TM wave} \end{cases} \tag{3.5}$$

$$P_2 = \begin{pmatrix} e^{+jk_{2x}d} & 0 \\ 0 & e^{-jk_{2x}d} \end{pmatrix}. \tag{3.6}$$

The determinant of the matrix D_i is equal to $-2k_{ix}/k$. It is worth to note that, in order to be consistent with the definitions of parameters for both polarizations, the free space wave number k is added to the matrix D_i, which will not affect the final results.

By combining the equations Eq. (3.2)-(3.4), a 2x2 matrix formulation for the slab media can be given in Eq. (3.7) as

$$\begin{pmatrix} A_1 \\ B_1 \end{pmatrix} = D_1^{-1} D_2 P_2 D_2^{-1} D_3 \begin{pmatrix} A'_3 \\ B'_3 \end{pmatrix} = \begin{pmatrix} M_{11} & M_{12} \\ M_{21} & M_{22} \end{pmatrix} \begin{pmatrix} A'_3 \\ B'_3 \end{pmatrix} \tag{3.7}$$

where the elements M_{ij} (*j*=1 and 2) of the matrix are given by Eq. (3.8) as

$$\begin{aligned}
M_{11} &= \frac{1}{2}(1+\frac{k_{3x}}{k_{1x}})\cos(k_{2x}d) + \frac{j}{2}(\frac{k_{2x}}{k_{1x}} + \frac{k_{3x}}{k_{2x}})\sin(k_{2x}d) \\
M_{12} &= \frac{1}{2}(1-\frac{k_{3x}}{k_{1x}})\cos(k_{2x}d) + \frac{j}{2}(\frac{k_{2x}}{k_{1x}} - \frac{k_{3x}}{k_{2x}})\sin(k_{2x}d) \\
M_{11} &= \frac{1}{2}(\frac{n_1 k_{3x}}{n_3 k_{1x}} + \frac{n_3}{n_1})\cos(k_{2x}d) + \frac{j}{2}(\frac{n_1 n_3 k_{2x}}{n_2^2 k_{1x}} + \frac{n_2^2 k_{3x}}{n_1 n_3 k_{2x}})\sin(k_{2x}d) \\
M_{12} &= \frac{1}{2}(\frac{n_1 k_{3x}}{n_3 k_{1x}} - \frac{n_3}{n_1})\cos(k_{2x}d) - \frac{j}{2}(\frac{n_1 n_3 k_{2x}}{n_2^2 k_{1x}} - \frac{n_2^2 k_{3x}}{n_1 n_3 k_{2x}})\sin(k_{2x}d)
\end{aligned} \tag{3.8}$$

Then in general, if the core contains a multi N-layer structure rather than only one core layer, the 2x2 matrix formulation can be obtained in a similar fashion as

$$\begin{aligned}
\begin{pmatrix} A_0 \\ B_0 \end{pmatrix} &= D_0^{-1} D_1 P_1 D_1^{-1} D_2 P_2 D_2 ... D_N P_N D_N^{-1} D_s \begin{pmatrix} A_s \\ B_s \end{pmatrix} \\
&= D_0^{-1} (\prod_{i=1,N} D_i P_i D_i^{-1}) D_S \begin{pmatrix} A_s \\ B_s \end{pmatrix} = \begin{pmatrix} M_{11} & M_{12} \\ M_{21} & M_{22} \end{pmatrix} \begin{pmatrix} A_s \\ B_s \end{pmatrix}
\end{aligned} \tag{3.9}$$

, where we can set $Q_i = D_i P_i D_i^{-1}$ as the transfer matrix for the *i*-th layer. Note that Q_i is uni-modular, e.g. $\det(Q_i) = 1$ as

$$Q_i = \begin{pmatrix} \cos(k_{ix}d_i) & j\sin(k_{ix}d_i)/q_i \\ jq_i \sin(k_{ix}d_i) & \cos(k_{ix}d_i) \end{pmatrix} \tag{3.10}$$

where

$$q_i = \begin{cases} \dfrac{k_{ix}}{k} & \text{for TE wave} \\ \dfrac{kn_i^2}{k_{ix}} & \text{for TM wave} \end{cases} . \tag{3.11}$$

By using the symmetry property of the transfer matrix Q_i, it can be shown that the matrix elements of M satisfy that $M_{21} = M_{12}^*$ and $M_{22} = M_{11}^*$. Furthermore, if we assume the light to be incident from the cover (n_c), the reflectance and transmittance of the waves through a multiplayer dielectric structure can be calculated as

$$R = |r|^2 \tag{3.12}$$

$$T = \frac{k_{sx}}{k_{0x}} |t|^2 \tag{3.13}$$

, where the reflection and transmission coefficients r and t are defined as follows:

$$r = \left(\frac{B_0}{A_0}\right)_{B_s=0} = \left(\frac{M_{21}}{M_{11}}\right) \tag{3.14}$$

$$t = \left(\frac{A_s}{A_0}\right)_{B_s=0} = \left(\frac{1}{M_{11}}\right) \tag{3.15}$$

Here we note that $R + T = 1$, because the determinant of matrix M can be calculated from equation (3.10) [because $\det(Q_i) = 1$ and $\det(M) = \det(D_0^{-1})\det(D_s)$] as

$$|M| = |M_{11}|^2 - |M_{12}|^2 = \frac{k_{sx}}{k_{0x}} \tag{3.16}$$

3.3 1D Bragg reflector

After having described the transfer matrix formulism of a general multi-layer structure, as well as its reflection and transmission properties, we can now consider the 1D Bragg structure of finite width, where we add the periodicity into the discussion. The structure is always used as an optical reflective media sandwiched by the cover (n_c) and substrate (n_s) layers, as shown in Fig. 3.3(a). This can generally consist N sections with pitch Λ (n=1, 2, …, N), and each section consists of P layers with refractive index n_p and thickness d_p (p=1, 2, …, P). In the simplest case, as shown in Fig. 3.3(b), we can have N sections, each consisting two alternating layers (n_1 and n_2), with corresponding thicknesses d_1 and d_2, respectively ($\Lambda = d_1 + d_2$).

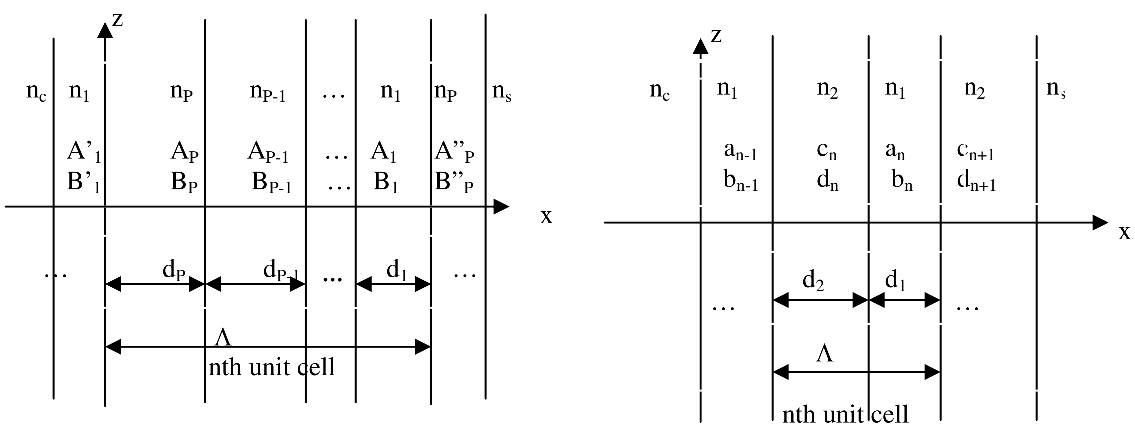

(a) General case: the unit cell with multiplayer (p) (b) Simple case: the unit cell with two layers

Figure 3.3 A schematic drawing of a 1D periodic layered isotropic media and the plane-wave amplitudes associated with the *n*th unit cell and its neighboring layers

By using the transfer matrix method, the section matrix M for the n-th unit cell can be express as follows

$$\begin{aligned}\begin{pmatrix} A'_1 \\ B'_1 \end{pmatrix} &= D_1^{-1} D_P P_P D_P^{-1} D_{P-1} P_{P-1} D_{P-1} ... D_2 P_2 D_2^{-1} D_1 P_1 \begin{pmatrix} A_1 \\ B_1 \end{pmatrix} \\ &= D_1^{-1} (\prod_{i=P,2} Q_i) D_1 P_1 \begin{pmatrix} A_1 \\ B_1 \end{pmatrix} = \begin{pmatrix} M_{11} & M_{12} \\ M_{21} & M_{22} \end{pmatrix} \begin{pmatrix} A_1 \\ B_1 \end{pmatrix} = (M) \begin{pmatrix} A_1 \\ B_1 \end{pmatrix}\end{aligned} \tag{3.17}$$

, where we note that $M_{21} = M_{12}^*$ and $M_{22} = M_{11}^*$. Elements of the section matrix M can be given as

$$\begin{aligned}M_{11} &= e^{jk_{1x}d_1} [\cos(k_{2x}d_2) + \frac{j}{2}(\frac{q_1}{q_2} + \frac{q_2}{q_1}) \sin(k_{2x}d_2)] \\ M_{12} &= e^{-jk_{1x}d_1} (-1)^m \frac{j}{2}(\frac{q_1}{q_2} + \frac{q_2}{q_1}) \sin(k_{2x}d_2)\end{aligned} \tag{3.18}$$

, where $q_i = k_{ix} / k$ for TE wave and $q_i = kn_i^2 / k_{ix}$ (i =1 and 2) for TM wave.

According to the Bloch-Floquet theorem [30], periodicity $n(x) = n(x + \Lambda)$ of the structure leads to Bloch wave solutions $E_K(x,z)$ of the Maxwell equations, then

$$E_K(x,z) = E_K(x,z) \exp[-j(\beta\, z + Kx)] \tag{3.19}$$

, where $E_K(x)$ is the Bloch wave function [$E_K(x) = E_K(x + \Lambda)$] and K is the Bloch wave number. In term of (3.17) and (3.19), the eigenvalue equation can be obtained as

$$\begin{pmatrix} M_{11} & M_{12} \\ M_{21} & M_{22} \end{pmatrix} \begin{pmatrix} A_1 \\ B_1 \end{pmatrix} = e^{+jK\Lambda} \begin{pmatrix} A_1 \\ B_1 \end{pmatrix} \tag{3.20}$$

After some simple analytic procedures, the dispersion relation between the Bloch wave number and the frequency can be obtained as [29]

$$K(\beta, \omega) = \cos^{-1}\left(\frac{M_{11} + M_{22}}{2} \right) / \Lambda \tag{3.21}$$

, where β is the tangential component of the Bloch wave vector and ω is the frequency. The above equation can be further expanded as

$$K(\beta,\omega)=\cos^{-1}\left(\cos(k_{1x}d_1)\cos(k_{2x}d_2)-\frac{1}{2}(\frac{q_1}{q_2}+\frac{q_2}{q_1})\sin(k_{1x}d_1)\sin(k_{2x}d_2)\right)/\Lambda \quad (3.22)$$

The eigenvectors corresponding to the above eigenmodes are also obtained as

$$\begin{pmatrix} a_0 \\ b_0 \end{pmatrix}=\begin{pmatrix} M_{12} \\ e^{iK\Lambda}-M_{11} \end{pmatrix} \quad (3.23)$$

By plot the governing equation Eq. (3.22) in terms of effective index and wavelength, we can obtain the following band diagram for TE and TM waves of the Bragg reflector as:

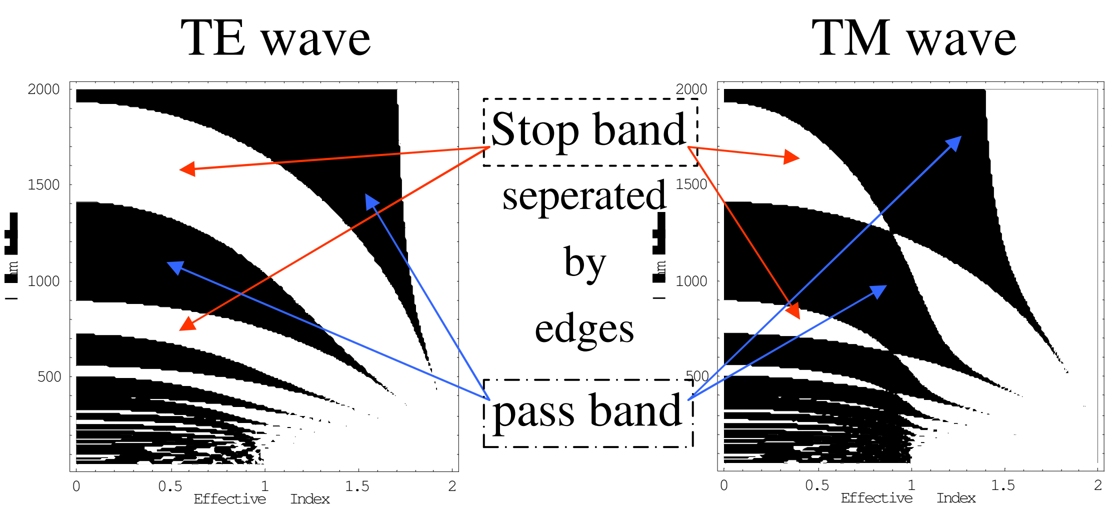

Figure 3.4 Band diagram of a 1D Bragg reflector.

The black regions are the pass bands with $\left|(M_{11}+M_{22})/2\right|<1$, which means that K is real and the waves travel through the layers without decay. The stop-band regions are where $\left|(M_{11}+M_{22})/2\right|>1$, such that $K = m\pi/\Lambda+iK_i$ is complex and the waves decay exponentially through the layers. The band-edges (i.e., borders between the black and white regions) are marked where $\left|\left(M_{11}+M_{22}\right)/2\right|=1$, such that the guidance condition for $k \sim \lambda$ at $K = m\pi/\Lambda$ are satisfied exactly.

For normal incidence onto the Bragg reflector, we can observe the following band shapes as in Fig. 3.5. Its intrinsic reflection characteristics are similar to the energy bands of the crystallized structure in solid state physics, where the extended Brillion-zone band diagram are obtained by self-repeating the reduced Brillion-zone image within the K = $m\pi/\Lambda$ region.

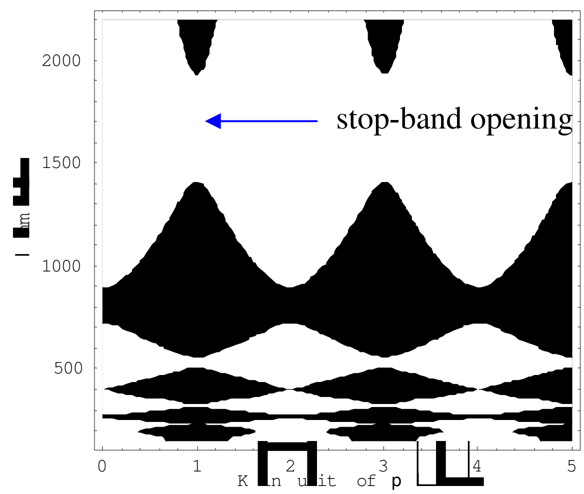

Figure 3.5 The extended Brillion-zone band diagram (λ-K) at normal incidence (k_z=0)

3.4 Summary

In this chapter, we have analytically studied the Bragg reflector, as cascade of two index-alternating layers, using the transfer matrix method. From the dispersion relation of this type of structures, we can find the medium to be transparent for certain wavelength range, which corresponds to the pass band, while being a perfect reflector for some of the other wavelengths if they sit in the stop band. This accumulative reflection of optical waves can be used effectively in modifying the functionality of optical devices, including coupling or reflective gratings in the waveguide, as well as the distributed Bragg reflections in lasers. In the following chapters, we will fully utilize this particular property and design new lasers for optical communication applications.

Chapter 4
Bragg Reflection Waveguide Based Single-Mode Laser

4.1 Introduction

The main purpose of our research is to overcome the existing difficulties in DFB, DBR and FP, and combine them into a new breed of low cost and feedback insensitive lasers. Bragg reflection waveguide (BRW) laser [31] is one of the choices that may provide an option. By placing two dissimilar Bragg reflectors as in Fig. 4.1 for the transverse direction claddings, whose stop bands overlap with each other by a small region, the waveguide can filter optical waves to allow only a sub-nanometer bandwidth of the fields to be guided in the structure. Then, a single mode laser with high spectral purity and feedback insensitivity can be built.

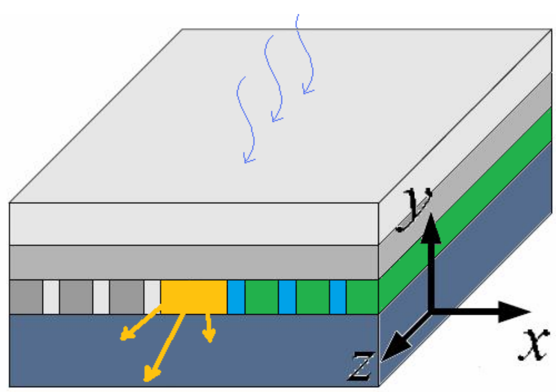

Figure 4.1 Asymmectric BRW single-mode laser design

For the infinite layer BRW, whose claddings are the Bragg reflectors as we have discussed in the previous chapter, the band edge of the waveguide is a clear-cut line (at $K = m\pi/\Lambda$ in Fig. 3.4) distinguishing the zero reflection and the total Bragg reflection regions. This is an ideal case, but there is no practical necessity or possibility to make a waveguide with infinite layers. Then, for any finite-layer BRWs, the incomplete reflection from the Bragg reflectors will introduce optical loss and band edge blurring that suggests a gradual transition from the total reflection to the diminishing zero reflection. The slope of this transition depends on the number of periods used in the waveguide, and also on the index contrast of two adjacent layers in each period.

Theoretically, we have to initiate the study based on the infinite-layer case and then use numerical methods, such as the finite-difference method, to calculate the more practical finite-layered (usually less 50) waveguide cases. We also need to pay attention to some key design parameters of the laser, such as the confinement factor, leakage loss and threshold gain, to optimize and balance the structure between manufacturing complexity and single-mode operation stability.

In the following subsections, we will discuss the mode properties of the BRW, and extend it to the single-mode laser designs. Also, we will analyse the laser's stability issues over several of its design parameters. Then, some practical laser designs done on the silicon substrate will be discussed.

4.2 BRW resonance condition and mode selection

As discussed in the previous chapter about the Bragg reflector, we can now use it to construct waveguide and achieve mode selections for laser uses. In the ray-optics model, light trapped in the guiding layer is considered to be bouncing back and forth along the propagation direction without reduction in intensity. Then, for waveguides made of Bragg reflectors, the cladding on each side of the guiding layer has to work in the forbidden band of the semi-infinite periodic structure. Within these bands, light undergoes an accumulated total reflection from the claddings and is finally confined in the guiding layer, regardless of the core's refractive index.

As we have discussed before for a guided wave in Chapter 2, the field pattern must be invariant in the direction of wave propagation. This means a standing wave must be set up in the transverse direction, with the total phase shift, acquired by the wave traveling after a transverse round trip between two boundaries of the guiding layer, being equal to an integer number of 2π. This is referred to as the transverse resonance condition, which is the main point different from the previous chapter's discussions, as we now not only have to work with the stop bands of the Bragg reflectors, but also have to tune relations of the reflectors and the core to find a proper resonance condition for the laser to work at designed wavelength.

The phase shift acquired by the wave in the guiding layers over a distance of d_g is $k_g d_g$, where $k_g = n_g k_0 \cos\theta$ is the x component of the wave vector. The transverse resonance condition can then be expressed as

$$2k_g d_g + 4\varphi = 2m\pi \tag{3.24}$$

, where 2φ is the phase shift acquired when the wave is incident upon the boundary between the guiding layer and the first layer of the Bragg structure.

The resonance condition of the Bragg waveguide can be carried out using the transfer matrix scheme as described in Chapter 2 and 3:

Because fields in any general periodic structure can be written as

$$F_1 = \left\{ a_{1j} \exp[ik_1(x - j\Lambda + \Lambda)] + b_{1j} \exp[ik_1(x - j\Lambda + \Lambda)] \right\} \exp(i\beta z) \tag{3.25}$$

$$F_2 = \left\{ a_{2j} \exp[ik_2(x - j\Lambda)] + b_{2j} \exp[ik_2(x - j\Lambda)] \right\} \exp(i\beta z) \tag{3.26}$$

, where F represents the electric field for the TE polarization and the magnetic field for the TM polarization and j is for the j-th unit cell, then, field connections between layers can be then written as

$$\begin{aligned}\begin{pmatrix} a_{1,j} \\ b_{1,j} \end{pmatrix} &= \frac{1}{2} \begin{pmatrix} \left(1+\frac{K_2}{K_1}\right) \exp\left[-i\left(k_1 d_1 + k_2 d_2\right)\right] & \left(1-\frac{K_2}{K_1}\right) \exp\left[-i\left(k_1 d_1 - k_2 d_2\right)\right] \\ \left(1-\frac{K_2}{K_1}\right) \exp\left[i\left(k_1 d_1 - k_2 d_2\right)\right] & \left(1+\frac{K_2}{K_1}\right) \exp\left[i\left(k_1 d_1 + k_2 d_2\right)\right] \end{pmatrix} \begin{pmatrix} a_{2,j} \\ b_{2,j} \end{pmatrix} \\ &= M \begin{pmatrix} a_{2,j} \\ b_{2,j} \end{pmatrix}\end{aligned} \tag{3.27}$$

, with $K_{1,2} = k_{1,2}$ for the TE polarization and $K_{1,2} = k_{1,2} / n_{1,2}^2$ for the TM polarization. Due to the Floquet theorem for periodic structures, the Bloch wave (of wave number K) can also be found in Bragg waveguide between any two of its adjacent cladding periods as

$$\begin{pmatrix} a_{2,j} \\ b_{2,j} \end{pmatrix} = \exp\left[iK\Lambda\right] \begin{pmatrix} a_{2,j-1} \\ b_{2,j-1} \end{pmatrix} \tag{3.28}$$

, which leads to

$$\begin{pmatrix} a_{2,j} \\ b_{2,j} \end{pmatrix} = C \begin{pmatrix} M_{12} \\ e^{-iK\Lambda} - M_{11} \end{pmatrix} \tag{3.29}$$

, as we have discussed in Chapter 3.

For the connection between the claddings and the core, we can derive the matrices as follows:

Consider the Bragg waveguide shown in Fig. 4.2, where $x = 0$ is defined as the interface between the guiding layer and the semi-infinite Bragg structure on the right-hand side,

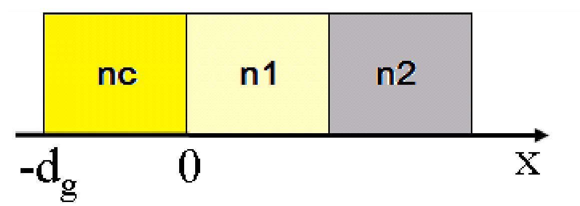

Figure 4.2 Core layer and its first two adjacent claddings in the Bragg waveguide .

the field in the guiding layer $-d_g < x < 0$ can be expressed as

$$F_g(x,z) = \left[a_g \exp\left(ik_g x\right) + b_g \exp\left(-ik_g x\right) \right] \exp(i\beta z) \tag{3.30}$$

, where F_g represents the electric field for the TE polarization or the magnetic field for the TM polarization along the y direction. By applying the continuity condition at $x = 0$, field amplitudes in the guiding layer a_g and b_g can be related to the field amplitudes in the first high-index layer of the Bragg structure as

$$\begin{pmatrix} a_g \\ b_g \end{pmatrix} = \frac{1}{2} \begin{pmatrix} 1+\dfrac{K_1}{K_g} & 1-\dfrac{K_1}{K_g} \\ 1-\dfrac{K_1}{K_g} & 1+\dfrac{K_1}{K_g} \end{pmatrix} \begin{pmatrix} a_{1,1} \\ b_{1,1} \end{pmatrix} \tag{3.31}$$

, where again, $K_g = k_g$ is for the TE polarization and $K_g = k_g / n_g^2$ is for the TM polarization. The reflection of wave at the interface $x = 0$ is simply given by $R = b_g / a_g$. From Eq.(3.31), we can find $R = \exp(i2\varphi_g)$ with

$$\varphi_g = \arctan\left(\frac{K_2}{K_g}\tan\varphi_0\right) \tag{3.32}$$

, where

$$\exp(i2\varphi_0) = \left\{\chi\left[1+\left(1-1/\chi^2\right)^{1/2}\right] - M_{11}\right\} \Big/ M_{12}\,. \tag{3.33}$$

The relation $\exp(-iK\Lambda) = \chi\left[1+\left(1-1/\chi^2\right)^{1/2}\right]$ has been used in the derivation, as well as $\chi = \cos K\Lambda = (M_{11} + M_{22})/2$. Therefore, within the stop band, reflection of the wave from the Bragg cladding is around one in magnitude, while the reflected wave acquires a phase shift of $2\varphi_g$.

Substituting the phase shift $2\varphi_g$ from Eq. (3.33) into the eigenvalue equation Eq.(3.24), we can solve the mode index n_{eff} of the Bragg waveguide structure, with respect to a given range of free-space wavelength λ. And for any BRW, we can find the effective index of the guided modes to follow the relation $0 < n_{eff} < n_g$.

In the following Fig. 4.3, we show the band structure of a specific Bragg waveguide for both TE and TM waves. The blue curves inside the stop bands would be the dispersion relations of the guided modes. The Bragg mirror structural parameters are set as n_{core}=1.0, n_1=2.0, n_2=1.0, t_c=1000 nm, a =300 nm, b =200 nm and Λ=a+b. These parameters are chosen only to demonstrate the versatile filtering functionality of the BRW, while more careful parameters should be chosen from real materials for further practical applications and designs.

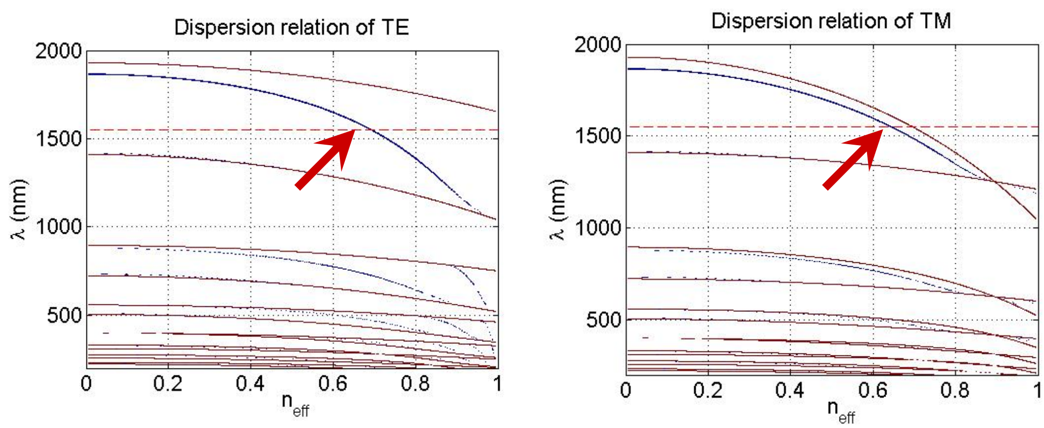

Figure 4.3 Dispersion curve inside stop band of the Bragg structure for both TE and TM waves.

4.3 Single mode design

4.3.1 Conventional design

Based on the previous two sections' discussions on the Bragg reflector's band structures and the waveguide dispersion conditions, we can proceed to the single mode design for the BRW laser constructions. Generally, there are two approaches available to make the waveguide highly selective on supported wavelengths. One is to make the stop band of both Bragg mirrors really narrow, such that only a few desired wavelengths can be reflected back from the claddings to the core and confined therein. This approach can be briefly described in the following series of graphs, with the starting Bragg mirror structural parameters as n_{core}=1.5, n_1=2.0, n_2=1.0, t_c=1000 nm, a =150 nm, b =100 nm and Λ=a+b.

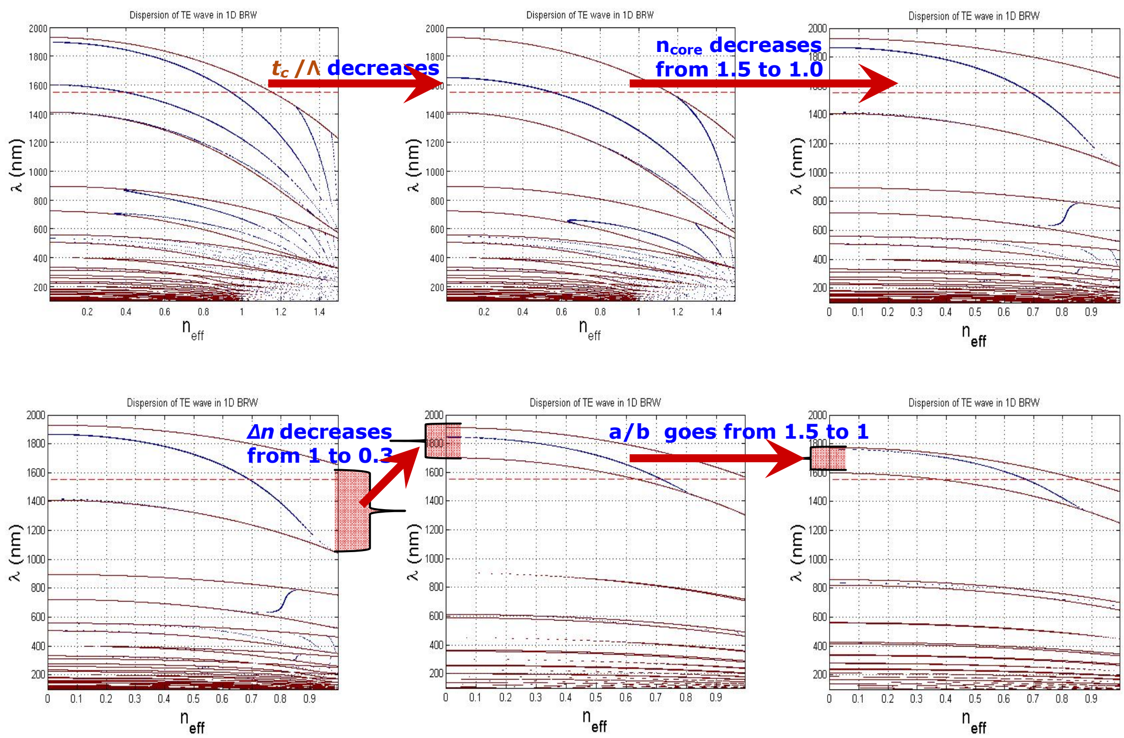

Figure 4.4 Design procedures for a single-mode Bragg waveguide example.

Then, from the Bragg mirror as shown in the first graph, we need to

1) choose a wavelength for the BRW to be operated on and a possible/desirable range of propagation constant for the guided light;

2) then, we need to adjust the BRW core width and cladding period ratio to reduce the number of supported dispersion curves in the stop band zone;

3) core index can also be decreased to minimize the curves available in the same band (as we see in the third graph that there is only one left now);

4) cladding index contrast and duty cycle can be changed to put the stop band over the above chosen (wavelength v.s. N_{eff}) area in the band structure plot, as seen in the last three graphs;

5) further careful adjustments of 2), 3) and 4) will be needed, until the narrow/broad bandwidth of the BRW is achieved.

However, as we expect in those single-mode narrow bandwidth BRW, confinement of the device would be poor, since most of the light is now distributed in the claddings, rather than the core for the supported wavelength, such that light amplification and lasing would be unrealistic to achieve. The following example in Fig. 4.5 shows a narrow bandwidth BRW calculated by FDM simulations, whose parameters are given as n_{core}=1.0, n_1=1.687, n_2=1.684, t_c=1000 nm, a =300 nm, b =200 nm and Λ=a+b.

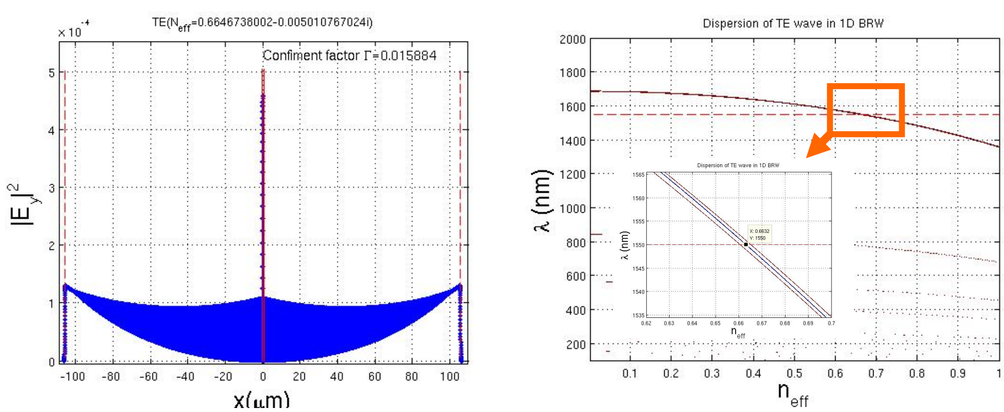

Figure 4.5 Field pattern and band diagram of the narrow bandwidth BRW

From the above field pattern plot, we see that the confinement for such design can be even less than 1%, such that light are all distributed in the claddings. The band diagram also shows the detailed tailoring of the cladding parameters are already approaching their limit, as the cladding index contrast is now only around 0.003. Therefore, we need to further study the sensitivity of this conventional symmetric BRW structure, as in the following subsection, for references of future asymmetric BRW designs.

4.3.2 Sensitivity study of conventional structure

To study the guidance characteristics of symmetric Bragg waveguide with respect to the key design parameters, we could calculate the effective index change, confinement and loss at different cladding index contrasts and number of periods.

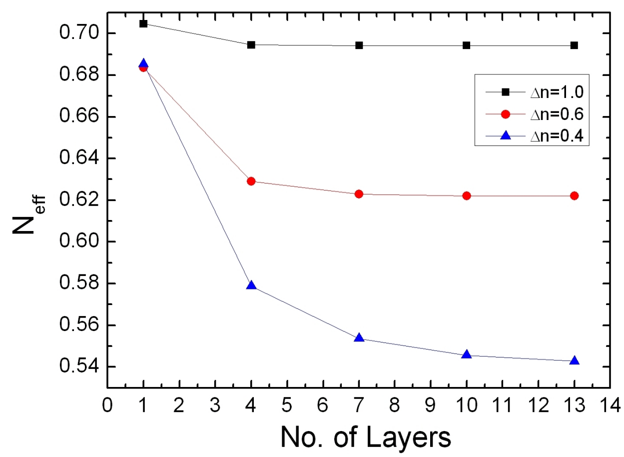

Figure 4.6 Effective index change with respect to the number of layers and cladding index contrast of the Bragg waveguide.

Here, we can see in Fig. 4.6, the effective index curve will converge faster to its infinite layer value, for the higher index contrast case, and will have a higher N_{eff} value, which means the dispersion curve will shift toward right side for the given wavelength.

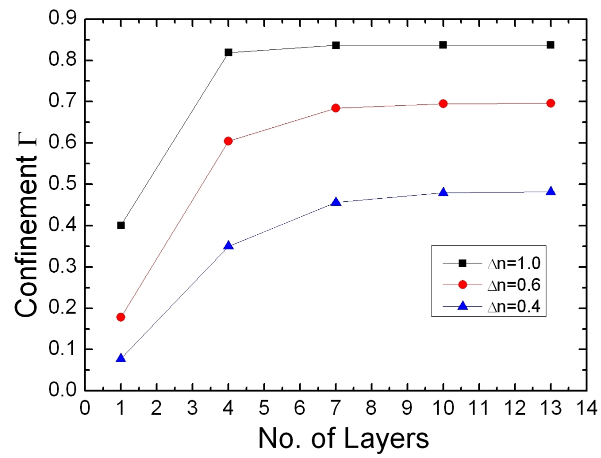

Figure 4.7 Confinement factor change with respect to the number of layers and cladding index contrast of the Bragg waveguide.

Here, in Fig. 4.7, we could see a higher converged confinement factor value to be found for the BRW with higher cladding index contrast. And at the same time, less number of layers would be needed to achieve the same confinement.

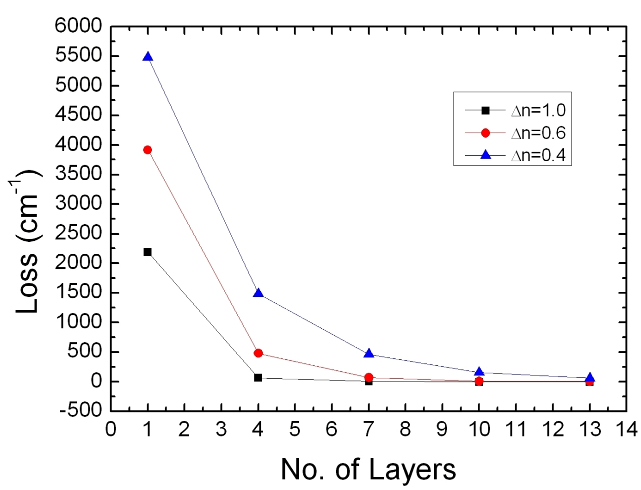

Figure 4.8 Loss with respect to the number of layers and cladding index contrast of the Bragg waveguide.

In Fig. 4.8, the leakage loss is also shown to prefer higher index contrast, while the pure loss that leaks out of the outmost cladding of the BRW structure will all approach to zero for the three index contrast cases. Inside the waveguide, we can expect different core confinement conditions for each case, as the higher index contrast one should have higher confinement in the core than the claddings. However, higher index contrast will also introduce more scattering loss to the structure in practice, which can increase the lasing threshold counteractively.

4.3.3 Asymmetric BRW design

Then, we came up with the design of asymmetric BRW that can achieve light confinement and selection at the same time. The schematic diagram for a typical BRW structure formed asymmetrically along the horizontal x-direction is shown in Fig. 4.9(a). Along the wave propagation direction (z-axis), the waveguide is uniform with total length of L. Reflectivities at the two facets of z=0 and z=L are assumed to be R_1 and R_2, respectively. The optical confinement along the vertical *y*-direction is neglected for the sake of simplicity without loss of generality. The refractive index profiles of the transverse waveguides are shown in Fig. 4.9(b), where parameters of the right and left Bragg reflectors are different so that their stop bands may be off-set [31] to produce wavelength selectivity of sub-nanometer resolution.

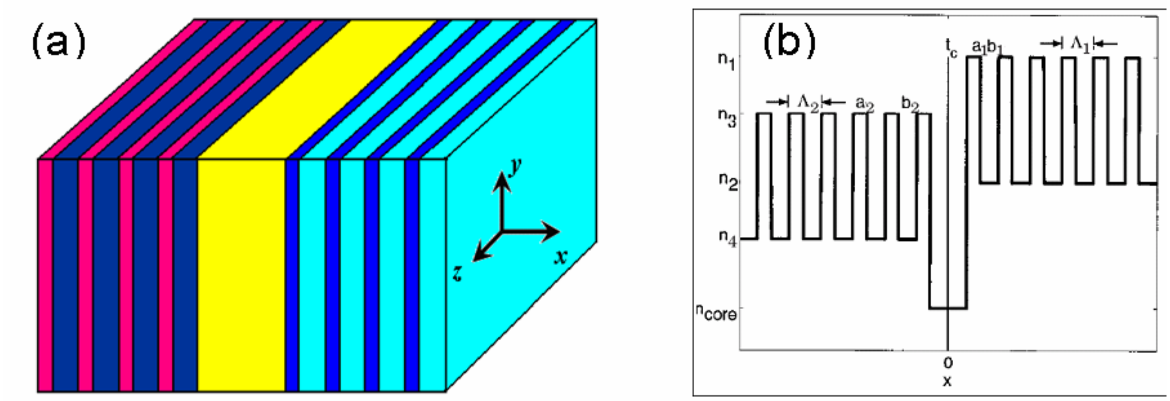

Figure 4.9 The schematic diagram for the designed Bragg reflection waveguide (BRW) lasers. (a) The designed model consisting of a transverse Bragg reflection waveguide along *x* and a uniform waveguide along *z*. (b) The refractive index profile for the one-dimensional BRW laser.

Physically, the lateral optical confinement along x is achieved by Bragg reflections from the wavelength-dependent reflectors as claddings of the waveguide. The optical field is confined in the low-index guiding layer, when the Bragg reflectors are working in the stop-band region [29]. Since characteristics of the band diagram are functions of the grating parameters, such as period, duty cycle, index difference, etc., we may control positions of the stop-bands of two different Bragg reflectors such that they overlap with each other by a small wavelength range (as observed in Fig. 4.10). Only in the overlapped region, the optical field is confined and guided in the core; outside that range, light leaks from the pass-band of one of the Bragg reflectors and hence will suffer significant loss.

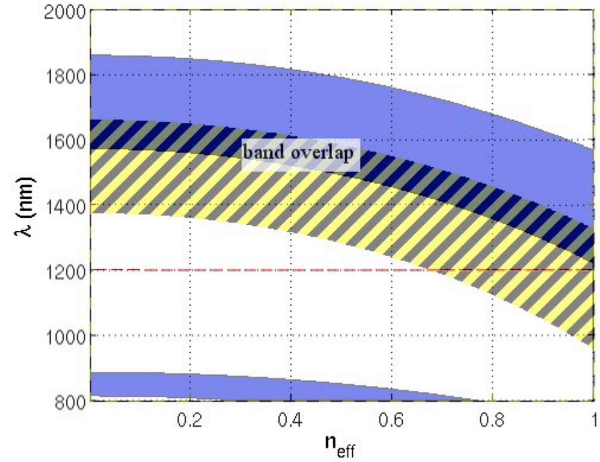

Figure 4.10 Qualitative illustration of the band diagram for the left and right infinite-layer Bragg reflectors in asymmetric BRW structure

Detailed characteristics of this kind of asymmetric waveguide can also be found in Ref.[32], and here we will be focused more on the issues for laser designs. i.e., threshold analysis for the asymmetric BRW structures with limited number (i.e., 10-20) of claddings.

4.3.4 Asymmetric waveguide design analysis

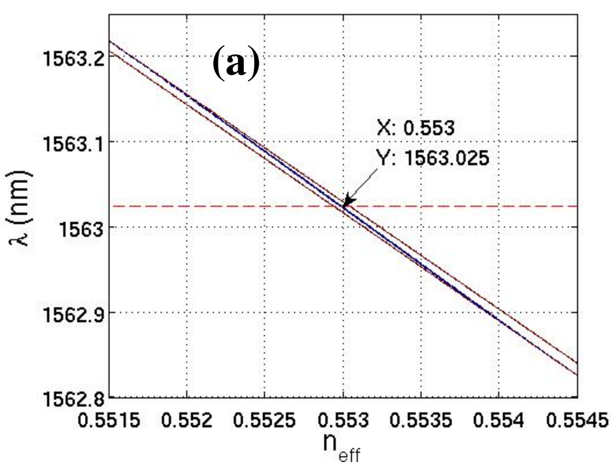

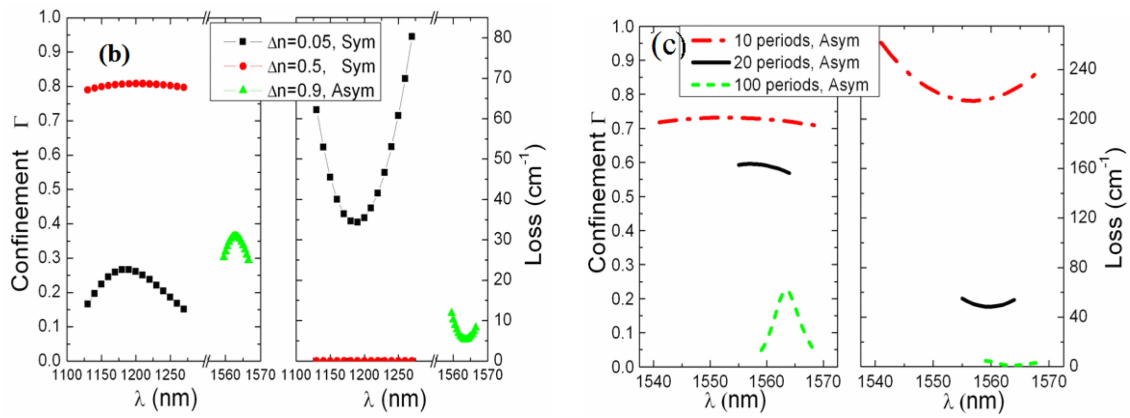

Figure 4.11 (a) Dispersion relation of an optimized infinite-layer asymmetric BRW (n_{core}=1.0, n_1=3.5, n_2=2.6, n_3=2.9658, n_4=2.0658, t_c=1000 nm, a_1=a_2=100 nm, b_1=b_2=200 nm); (b) Confinement and leakage loss profiles for the 50-period finite-layer asymmetric BRW (green-triangle line, other parameters are the same as in (a)), compared with two 50-period finite-layer symmetric BRWs with low (Δn=0.05, black-squared line) and high (Δn=0.5, red-circled line) index contrast; (c) Confinement and leakage loss profiles for the 10-, 20-, and 100-period finite-layer asymmetric BRWs (other parameters are the same as in (a)).

Band diagrams for the left and right infinite-layer Bragg reflectors in Fig. 4.9(a) are calculated from the transfer matrix method [29, 33] and shown in Fig. 4.10 as blue and left-shaded bands, respectively. By properly positioning the two stop bands, we find that their overlap can be designed sufficiently small to produce desirable band shape as shown in Fig. 4.11(a). For the ideal infinite-layer case, no wave leaks out of the waveguide and a selected bandwidth of the guidance can be narrowed down to 0.4 nm.

For the finite-layer (50-period) BRW designs, leakage through the claddings will lower the confinement and increase the total loss. Nevertheless, a narrow wavelength range with high confinement and low loss can still be guaranteed as illustrated by the green-triangle lines in Fig. 4.11(b). As a comparison, symmetric BRWs with high ($\Delta n = |n_1 - n_2| = 0.5$) and low ($\Delta n = 0.05$) index-contrast are included as the red (dotted) and black (squared) lines in the same figure. The high index-contrast symmetric BRW, as seen, has weak wavelength selectivity, while the low contrast one suffers high wave-penetration into the passive waveguide claddings, which cause low confinement and high loss in the finite-layer case. Therefore, neither of them can be used as the asymmetric one to balance the trade-off between the confinement/loss and the wavelength selectivity, which are the main factors determining a desirable threshold gain pattern for a laser.

In Fig. 4.11(c), we also compared the effect of number of claddings on the same properties of the asymmetric BRWs. As we see, confinement and loss profiles of the waveguide are smoothed by the reducing number of claddings. Consequently, sharpness of the band-edges can be ameliorated. This leads to the desirable results that the structural complexity, threshold level, and side-mode suppression are all balanced for a stable and realizable BRW laser, as we will further explain later in this section.

4.3.5 Threshold analysis

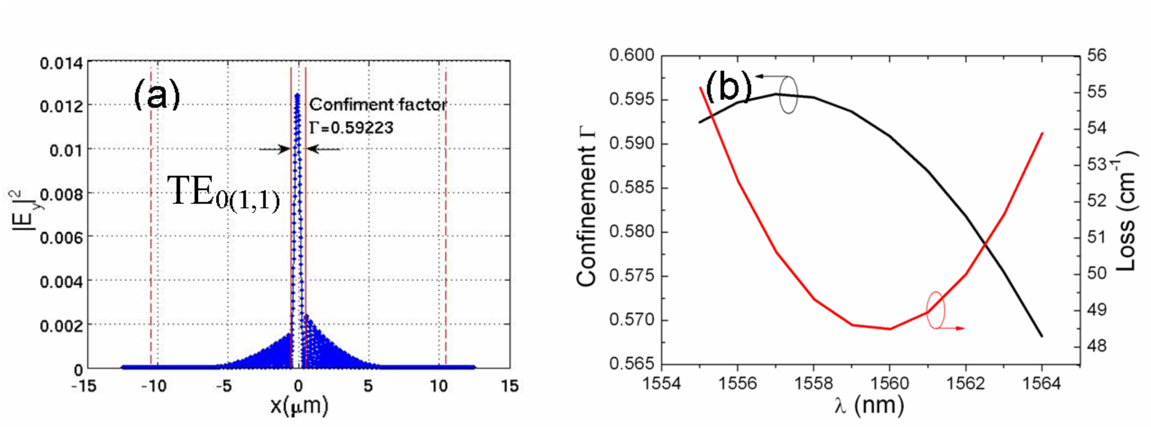

Figure 4.12 (a) Field amplitude for the TE wave of a 20-period finite-layer asymmetric BRW at λ=1559 nm (other parameters are the same as in Fig. 4.11(a)); (b) Confinement and leakage loss as a function of wavelength for the same BRW structure as in (a).

The numerical calculation of the single guided mode electric field is given in Fig. 4.12(a) (with power normalized to unity), and the confinement factor with corresponding leakage loss for the 20-period-cladding case is shown in Fig. 4.12(b). From the figures, we see that the confinement factor of the 20-period case maximizes to 59.5%, while the loss profile minimizes to 48.3 cm^{-1} around 1558 nm. By properly adjusting these parameters, we can design the asymmetric BRW that has desirable threshold gain (g_{th}) pattern to select proper oscillation mode and to ensure single-mode lasing with high SMSR. Eq. (3.34) is the formula we use to carry out threshold gain analysis of the BRW lasers:

$$\Gamma(\lambda) g_{th}(\lambda) = \gamma(\lambda) + \frac{1}{2L} \ln\left(\frac{1}{R_1 R_2}\right) \tag{3.34}$$

, where parameter $\gamma(\lambda)$ is the leakage loss due to wave penetrations through the finite-period Bragg reflectors as shown by the red line in Fig. 4.12(b) and L is the FP cavity length. The longitudinal resonance condition can be given as

$$\sin[n_{eff}(\lambda) kL] = 0 \tag{3.35}$$

, where $n_{eff}(\lambda)$ is the core effective index and k is the wave number in vacuum. The FP mode spacing can be obtained from the following formula [34] as

$$\Delta\lambda = \frac{-\lambda^2}{2L[n_{eff} - \lambda(dn_{eff} / d\lambda)]}. \tag{3.36}$$

4.3.6 Sensitivity study of structural parameters

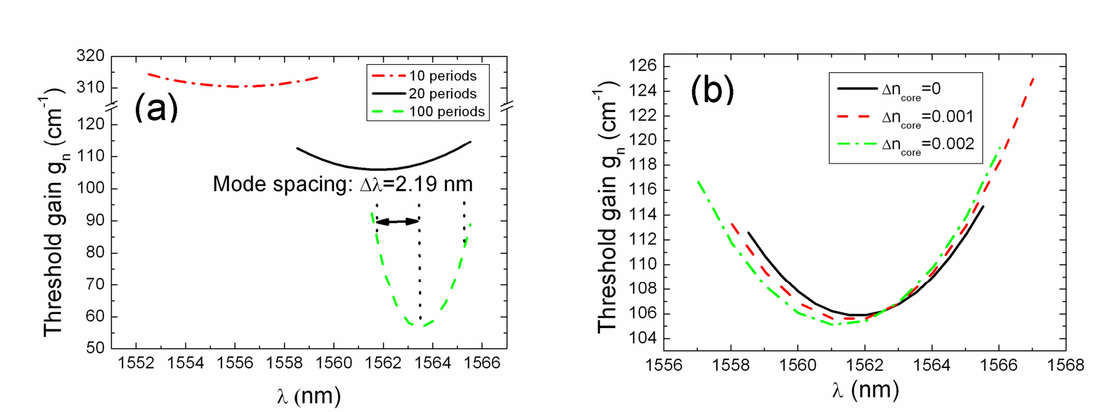

Figure 4.13 Threshold gain of asymmetric BRWs with (a) 10-, 20- and 100-period claddings. Other structure parameters are the same as in Fig. 4.11(a). (b) Sensitivity of threshold gain to the core index changes in the asymmetric 20-period cladding case.

To study the sensitivity of threshold gain to the number of periods, we could plot the threshold gain for the BRW laser of $L = 1000\mu m$ and end-facet mirror reflectivities to be $R_1 = 0.3$ and $R_2 = 0.3$ in Fig. 4.13(a), for the 10, 20 and 100 periods of the Bragg gratings, respectively. It is observed that, by reducing the number of layers in the cladding, the threshold gain increases due to overall higher leakage loss. In the meanwhile, the opening angle of the curve, which qualitatively represents sharpness of the stop-band edges, becomes wider. This latter effect will help to ameliorate the band-edge sensitivities and reduce mode-hoping due to shift of the band-edge. Also, with reducing number of cladding layers, the structural complexity is reduced. Therefore, for the design of a stable and optimized BRW laser, the threshold level, the structural complexity and the side-mode suppressions have to be all balanced.

To quantitatively study the sensitivity of threshold gain to the core index changes, we plot g_{th} with $n_{core} = 1$, 1.001 and 1.002 for the 20-period case in Fig. 4.13(b), from which we could see that the wavelength shift in the extreme situation ($n_{core} = 1.002$) is still less than one mode spacing (i.e., $d\lambda_{shift} = 0.8nm < 2.2nm$) for this design. This shows that the system is to remain in single-mode operation condition when core index is changed during the lasing process.

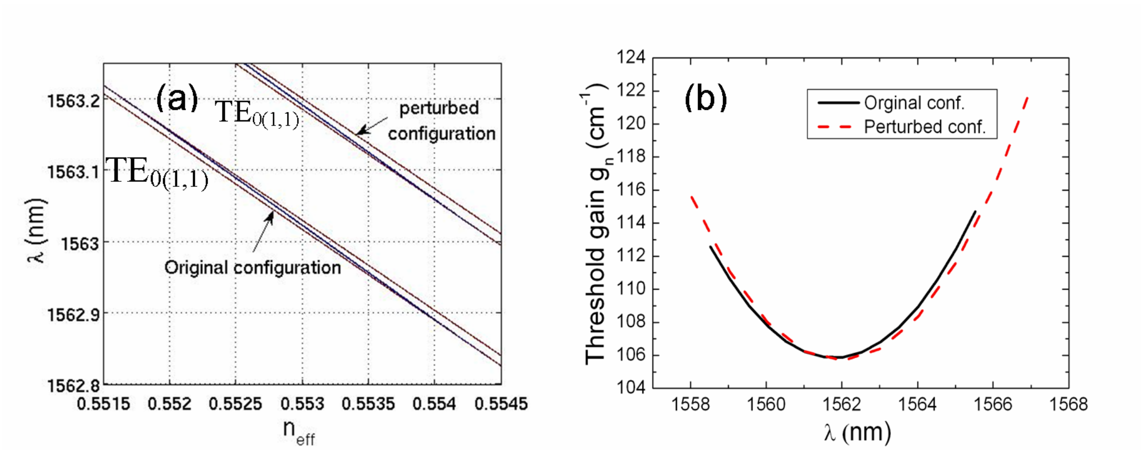

Figure 4.14 (a) Band diagram of perturbed asymmetric BRW with infinite periods of the claddings compared with original configuration as shown in Fig. 4.11(a). (b) Corresponding threshold gain change due to perturbation of the cladding index for the 20-period finite-layer case.

To study the sensitivity of threshold gain to the small change in cladding index, we perturbed the original configuration of (n_1=3.5, n_2=2.6, n_3=2.9658, n_4=2.0658) to (n_1=3.497, n_2=2.603, n_3=2.9628, n_4=2.0648) as shown in Fig. 4.14(a) for the infinite layer case. Threshold gain for the corresponding 20-period case is calculated and shown in Fig. 4.14(b). The results also show stability of the structure when operated in the single-mode condition. Mode-hopping is not likely to happen under small perturbations of the cladding or core indices.

From the above, we see that the 20-period asymmetric BRW laser structure exhibits a good balance between the structural complexity, threshold level, and mode selectivity.

4.3.7 Laser performance

From the above analysis, we can see a threshold-gain margin of more than 3 cm^{-1} can be achieved. This gain difference may be directly linked to SMSR from the following formula as [35]

$$SMSR = \frac{2P_0}{h\nu v_g n_{sp}\gamma_{tot}}\left[\frac{\Delta\alpha L}{\gamma_m L}\right], \tag{3.37}$$

where P_0 is the main-mode power, $\Delta\alpha$ is the threshold-gain margin, v_g is the group velocity, n_{sp} is the spontaneous emission factor, γ_{tot} and γ_m are the total loss and mirror loss for the mode with lowest loss, respectively. By assuming $n_{sp}=1$ for the purpose of illustration, we obtain the SMSR as a function of the main-mode power as follows:

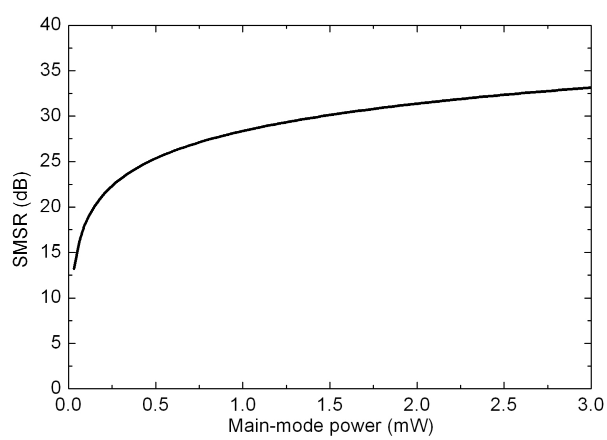

Figure 4.15 Side-mode suppression ratio of the BRW laser at different main-mode power.

4.4 Practical design of BRW laser

From the above discussions of the asymmetric BRW for laser applications, we can further simplify the design by using only one material for the waveguide substrate and etching different widths of air-slots on the surface to make the claddings as shown in Fig. 4.16 as follows:

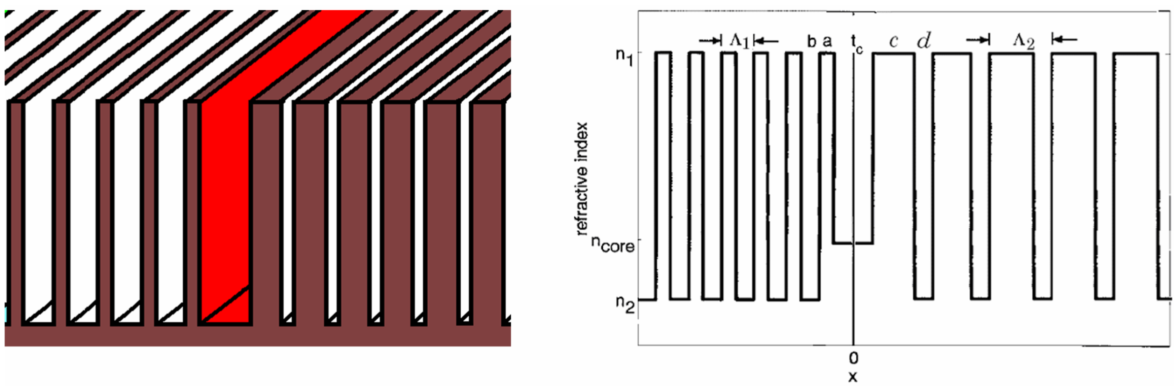

Figure 4.16 Alternative structure and refractive index profile of the 1D BRW design for Bragg laser

For the sake of simplicity, we assume that the slots are etched deep enough to ensure the validity and accuracy for the one-dimensional (1D) approximation in our modeling and simulation. Also, in order to prevent light from leaking into the high-index substrate region in the vertical direction, and guarantee confinement of the light in the core, we can also grow a few layers of highly reflective low-index materials (of thickness $\lambda/2$) underneath the active region and above the substrate, such that guidance of light can be maximized in the core, vertically.

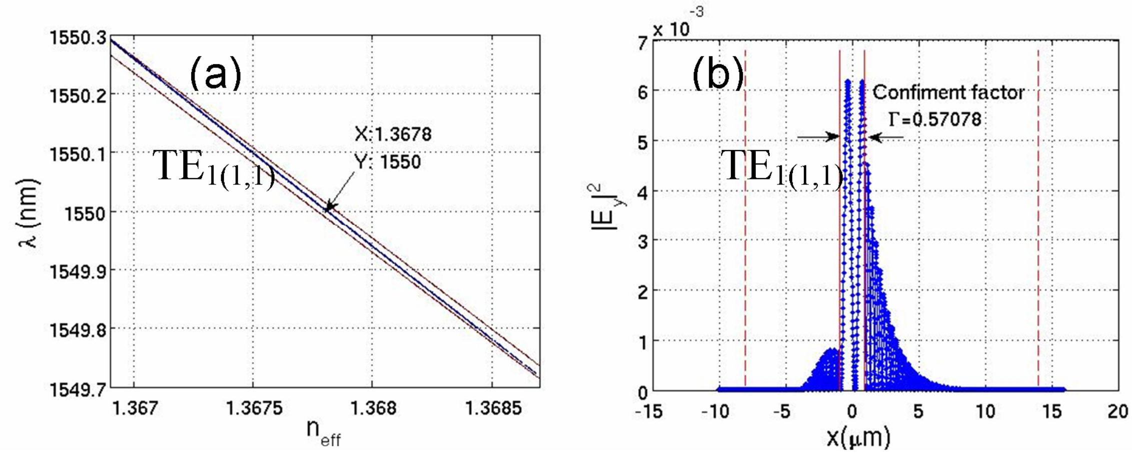

Figure 4.17 (a) Dispersion relation of a Si-based infinite-layer asymmetric BRW (n_{core}=1.5, n_1=3.45, n_2=1.0, t_c=1934 nm, a =108 nm, b=196 nm, c=249 nm and d=51 nm); (b) Field profile of the TE wave for the same structure at λ=1575 nm with finite number of layers (30 periods on the right and 10 periods on the left).

As the first step, we calculate the band-gap dispersion curve for the ideal infinite-period structure [29, 33] and the field pattern for the finite-period case, as shown in Figs. 4.17 (a) and (b). It is noted that, in the extreme case, the bandwidth of guidance can be as narrow as 0.6 nm. We observe, in the finite-layer case, that the optical field leaks more into the right-hand-side cladding due to its weaker reflective nature. From the band-gap point of view, this means that the stop band of the right-side cladding is narrower than that on the left, due to the fact that air slots are of smaller size on the right-side of the Si substrate. To equalize the reflections from both Bragg reflectors, we may use more periods on the right in the following example (e.g., 30 on the right and 10 on the left), whose parameters are n_{core}=1.5 (for Er-doped Si-NC in silica), n_1=3.45 (silicon substrate), n_2=1.0 (air), t_c=1934 nm, a =108 nm, b=196 nm, c=249 nm and d=51 nm.

To examine the performance of this BRW design as a single-mode laser, we calculate the confinement factor, the leakage loss, and the threshold gain by assuming the cavity length $L = 500\mu m$ and the facet reflectivity $R_1 = R_2 = 0.3$, as shown in Fig. 4.18.

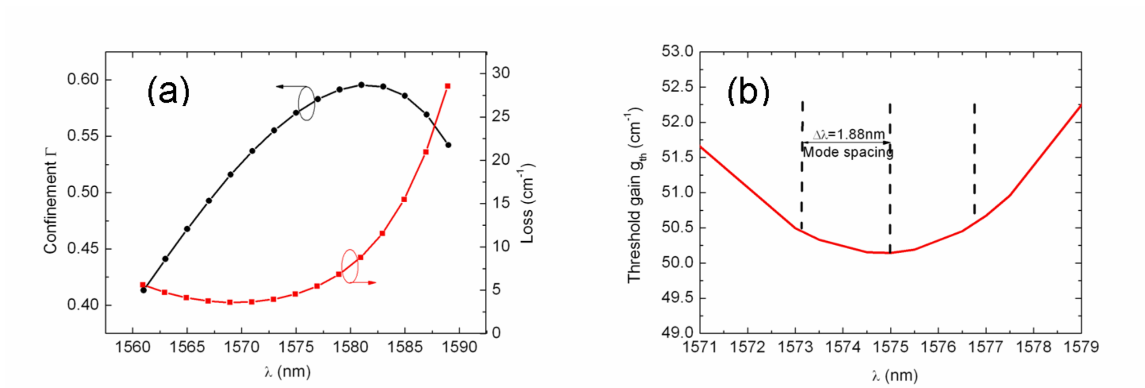

Figure 4.18 (a) Confinement factor, and (b) threshold gain of the Si-laser with Er-doped SRSO core

From Fig. 4.18(b), we observe that the threshold gain difference is 0.5 cm^{-1}, which is sufficient to guarantee a 20 dB side-mode suppression ratio (SMSR) as predicted from Eq. (3.37) for the single-mode CW operation. To further validate this point, variation of the SMSR with the central mode power is plotted in Fig. 4.19, where $n_{sp} = 1.34$ is assumed [35].

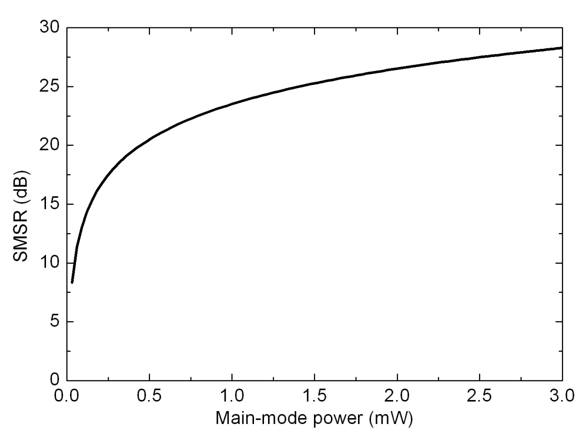

Figure 4.19 SMSR of Si-based BRW laser with Er-doped SRSO at different main-mode power

Vertically, we also find a few literatures [95-96] employing the ideas we have proposed for the asymmetric design of BRW single-mode lasers, and the following plots are cited from the references.

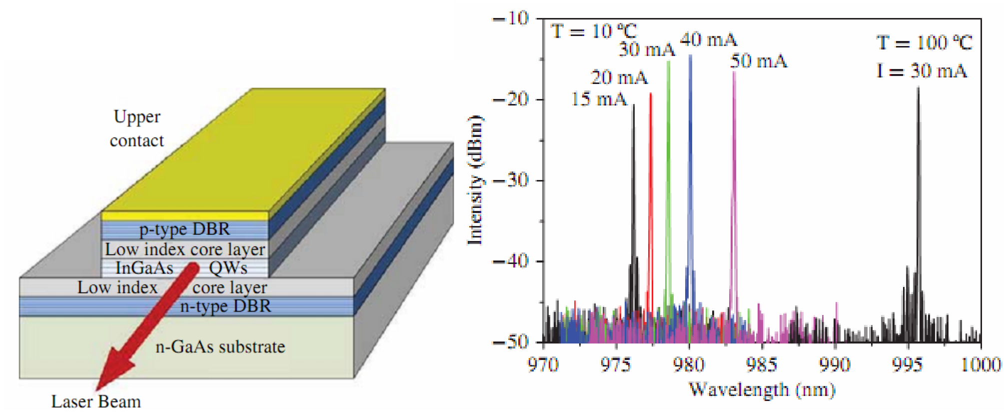

Figure 4.20 Vertical design of single BRW laser [96]

Here, we observe the wavelength shift to be highly dependent on the temperature and injection current, which may be caused by the carrier-induced index change through the claddings, while in our transverse design carriers are only through the active region.

4.5 Summary

In this chapter, we have proposed and analyzed the single-mode BRW laser that combines the longitudinal FP cavity and transverse Bragg reflectors together, for mode selection. As one of the advantages, low index gain materials can now be used in the laser structure for light amplification and confinement at the same time. Then, the use of FP cavity can also improve the laser's performance in environment with high amount of optical feedback, which suits better over DFB and DBR lasers for FTTH applications.

Chapter 5

Time domain transfer matrix method

5.1 Introduction

After having discussed the transverse direction modifications on the FP cavity, i.e., the BRW laser designs in the previous chapter, we now precede to the longitudinal direction modifications for the newly developed discrete mode (DM) laser, which is claimed to have both low cost and feedback insensitive properties while lasing in single-mode state with high SMSR. Details of this laser will be described in the next chapter, while here we introduce and emphasize more on the numerical model constructions, for the lasers to be simulated in real time. This is equally important for the laser property studies as there has been few comprehensive time domain model developed yet, to our knowledge, to study the static and dynamic behaviours of the non-periodic lasers, especially the DM lasers.

To qualitatively study the actual performances of this DM laser in various operation conditions, we need to establish a simulation model that can predict behaviours of the device under different current injections and external perturbations. Time domain transfer matrix method (TD-TMM) [36-42] is one of the choices that can provide such information. The model is constructed under the concept of conventional transfer matrix method, i.e., light waves traveling in the forward and backward directions inside the laser cavity are governed by the cascade of homogeneous propagation matrices and the interface scattering matrices through the structure. The only difference in TD-TMM is that the evolution time is now included in the model, where matrix multiplication is performed piecedwisely in time domain. The general idea of this method is also shown in the following figure (Fig. 5.1), where at different times *t* and *t+dt*, the inwards fields on either side of the section *k* are updated by the transfer matrix $A_k(t)$, and travel outwards on opposite sides of the section after time increment/step *dt*.

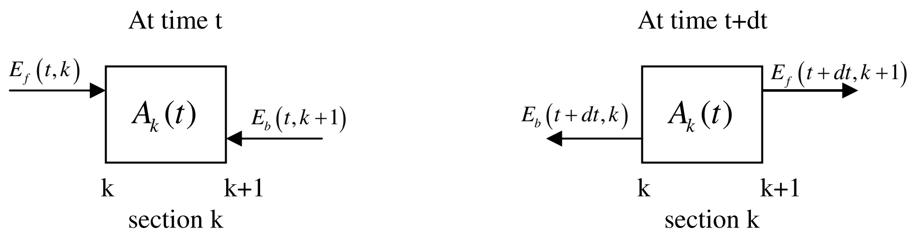

Figure 5.1 General idea of TD-TMM

5.2 Conventional transfer matrix method along longitudinal direction

To begin the time-domain simulation of a laser, we first need to mention the conventional transfer matrix method that has been used to describe the field propagations along the longitudinal direction [39]. Its formulation is slightly different from the previously discussed transverse transfer matrix method as in Chapter 2 and 3.

Here, we still start from the wave equation as follows

$$\left[\nabla^2 + \frac{\omega^2}{c^2}\varepsilon(x,y,z)\right]E_y(x,y,z) = 0 \tag{5.1}$$

, and separate the field E_y into its transverse and longitudinal components as

$$E_y(x,y,z) = \phi(x,y)F(z). \tag{5.2}$$

Then, we can write the two equations for their respective directions as follows

$$\left[\frac{\partial^2}{\partial x^2}+\frac{\partial^2}{\partial y^2}+\frac{\omega^2}{c^2}\varepsilon(x,y,z)\right]\phi(x,y)=\beta^2\phi(x,y) \tag{5.3}$$

$$(d^2/dz^2+\beta^2)F(z)=0 \tag{5.4}$$

, where β is the propagation constant.

In a homogeneous region, β is independent of the position *z*, so we can solve the second equation and write the electric field $E_y(x,y,z)$ as

$$E_y=\left[E_f\exp(-j\beta z)+E_b\exp(j\beta z)\right]\phi(x,y) \tag{5.5}$$

, where E_f and E_b are the forward and backward field amplitudes in the region.

For gratings and material junctions along the *z*-direction, we would find the propagation constant β to be different on either side of the index jump, such that the electric and magnetic fields in different regions can be connected using the boundary condition of the interface as

$$\begin{aligned} E_{y,1}\big|_{z=0} &= E_{y,2}\big|_{z=0} \\ \frac{\partial}{\partial z}E_{y,1}\bigg|_{z=0} &= \frac{\partial}{\partial z}E_{y,2}\bigg|_{z=0} \end{aligned}. \tag{5.6}$$

Here for simplicity, we have assumed the discontinuity to be at $z=0$, and the first order derivative in Eq. (5.6) is given by the $H_x\left(=\frac{\partial}{\partial z}E_y\right)$ field continuity condition.

Then, we can have

$$\begin{aligned} \left(E_{f,1}+E_{b,1}\right)\phi_1(x,y) &= \left(E_{f,2}+E_{b,2}\right)\phi_2(x,y) \\ -j\beta_1\left(E_{f,1}-E_{b,1}\right)\phi_1(x,y) &= -j\beta_2\left(E_{f,2}-E_{b,2}\right)\phi_2(x,y) \end{aligned} \tag{5.7}$$

, which by multiplying both sides of the above equations by $\phi_1(x, y)$ and integrating over the transverse plane gives

$$\begin{aligned}&\left(E_{f,1}+E_{b,1}\right)\int\phi_1\phi_1 dxdy=\left(E_{f,2}+E_{b,2}\right)\int\phi_1\phi_2 dxdy\\&\beta_1\left(E_{f,1}-E_{b,1}\right)\int\phi_1\phi_1 dxdy=\beta_2\left(E_{f,2}-E_{b,2}\right)\int\phi_1\phi_2 dxdy\end{aligned}. \tag{5.8}$$

In matrix form, we have

$$\begin{pmatrix}E_{f,1}\\E_{b,1}\end{pmatrix}=\begin{pmatrix}\frac{\beta_1+\beta_2}{2\beta_1}\chi_{12}^{TE} & \frac{\beta_1-\beta_2}{2\beta_1}\chi_{12}^{TE}\\ \frac{\beta_1-\beta_2}{2\beta_1}\chi_{12}^{TE} & \frac{\beta_1+\beta_2}{2\beta_1}\chi_{12}^{TE}\end{pmatrix}\begin{pmatrix}E_{f,2}\\E_{b,2}\end{pmatrix} \tag{5.9}$$

, with $\chi_{12}^{TE}=\dfrac{\int\phi_1\phi_2 dxdy}{\int\phi_1^2 dxdy}$.

If the laser is assumed to have only the fundamental guided mode in the transverse direction, the overlap integral χ_{12}^{TE} of those modes in adjacent regions can be set to 1, which gives the following equation for the case of index jump as

$$\begin{pmatrix}E_{f,1}\\E_{b,1}\end{pmatrix}=\begin{pmatrix}\frac{n_1+n_2}{2n_1} & \frac{n_1-n_2}{2n_1}\\ \frac{n_1-n_2}{2n_1} & \frac{n_1+n_2}{2n_1}\end{pmatrix}\begin{pmatrix}E_{f,2}\\E_{b,2}\end{pmatrix}, \text{ i.e., } T_{12}=\begin{pmatrix}\frac{n_1+n_2}{2n_1} & \frac{n_1-n_2}{2n_1}\\ \frac{n_1-n_2}{2n_1} & \frac{n_1+n_2}{2n_1}\end{pmatrix}. \tag{5.10}$$

For the homogeneous region, we have $\beta_1=\beta_2$, and by combining Eq. (5.9) and (5.5), we can get

$$\begin{pmatrix}E_{f,1}\\E_{b,1}\end{pmatrix}=\begin{pmatrix}\mathrm{e}^{-i\beta_1 z} & 0\\ 0 & \mathrm{e}^{i\beta_1 z}\end{pmatrix}\begin{pmatrix}E_{f,2}\\E_{b,2}\end{pmatrix}, \text{ i.e., } P=\begin{pmatrix}\mathrm{e}^{-i\beta z} & 0\\ 0 & \mathrm{e}^{-i\beta z}\end{pmatrix}. \tag{5.11}$$

5.3 Governing Equations for the time domain transfer matrix method

Similar to the conventional transfer matrix method, time domain TMM is also to divide the laser's longitudinal cavity into a few number of equal-size sections, whose length is controlled by the distance that light travels in the medium within a preset time step. Within each section, the parameters, such as the material gain, carrier density and photon density, etc., are assumed to be homogeneous sectional-wide. But between different sections, these parameters may vary to allow for longitudinal inhomogeneities, such as the spatial hole burning effect and the multi-pole current injections. Each section is characterized by a cascade of the corresponding scattering and propagation matrices, which modify the forward and backward traveling waves as they pass through the section. The use of matrices here is different from that in the static/conventional case, whose objective is to obtain the overall-matrix of the structure and determine its eigenmodes that can be supported by the waveguide. In time domain TMM, sequence of time for the wave propagation is included, which uses the sectional-matrices to update the wave amplitudes self-consistently.

Again, as we have discussed in the previous section about the conventional transfer matrix method, amplitudes of the two counter-propagating waves on either side of the elementary section, as in Fig. 5.1, can be connected as follows:

$$\begin{bmatrix} E_f \\ E_b \end{bmatrix}_{k+1} = \left[A_k \right] \begin{bmatrix} E_f \\ E_b \end{bmatrix}_k \tag{5.12}$$

, where matrix A represents the propagation matrix P, if section k is a uniform medium of the complex propagation constant β and length L, as

$$P = \begin{bmatrix} e^{-j\beta L} & 0 \\ 0 & e^{j\beta L} \end{bmatrix}; \tag{5.13}$$

or the scattering matrix T, if it is an index jump from n_1 to n_2, as

$$T_{12} = \begin{bmatrix} \frac{n_2+n_1}{2n_2} & \frac{n_2-n_1}{2n_2} \\ \frac{n_2-n_1}{2n_2} & \frac{n_2+n_1}{2n_2} \end{bmatrix}; \tag{5.14}$$

or any combination of those two for more general cases.

Then, for the time domain TMM [38], we can include the time factor by considering a typical section k at time t described by the transfer matrix A as follows:

$$\begin{bmatrix} E_f(t+dt,k+1) \\ E_b(t,k+1) \end{bmatrix} = \left[A_k(t)\right] \begin{bmatrix} E_f(t,k) \\ E_b(t+dt,k) \end{bmatrix} = \begin{bmatrix} a_{11}(t,k) & a_{12}(t,k) \\ a_{21}(t,k) & a_{22}(t,k) \end{bmatrix} \begin{bmatrix} E_f(t,k) \\ E_b(t+dt,k) \end{bmatrix} \tag{5.15}$$

, where through matrix A, the forward and backward-traveling waves $E_f(t,k)$ and $E_b(t,k+1)$ on either side of section k at time t will appear on their respective opposite sides at time $t+dt$ with updated amplitudes $E_f(t+dt,k+1)$ and $E_b(t+dt,k)$. During this process, matrix A is assumed to be unchanged over the time interval from t to $t+dt$. Then we can write out their relations in the equation form as

$$\begin{aligned} E_f(t+dt,k+1) &= a_{11}(t,k)E_f(t,k) + a_{12}(t,k)E_b(t+dt,k) \\ E_b(t,k+1) &= a_{21}(t,k)E_f(t,k) + a_{22}(t,k)E_b(t+dt,k) \end{aligned} \tag{5.16}$$

, which can also be rearranged to produce the expression for the updated amplitudes in terms of the old wave amplitudes and transfer matrix elements as

$$\begin{aligned} E_b(t+dt,k) &= \left[E_b(t,k+1) - a_{21}(t,k)E_f(t,k)\right] / a_{22}(t,k) \\ E_f(t+dt,k+1) &= a_{11}(t,k)E_f(t,k) + a_{12}(t,k)E_b(t+dt,k) \end{aligned} \tag{5.17}$$

At each time increment, the traveling wave would advance along the structure by one section, with their amplitudes on both sides of each section being updated by the matrix multiplication. Therefore, Eq. (5.17) is the governing equation for the time-domain traveling wave model, whose implicit assumption is that the simulation time step of this method has to be much larger than the characteristic lifetime of carriers and photons in the waveguide's gain region, such that matrix *A* can represent a stabilized state of wave as it propagate through each section piecewisely.

For the boundary conditions at two ends of the waveguide ($z=0$ and $z=L$), we have to require the fields to be connected by the facet reflectivities r_f and r_b as

$$E_f(0) = r_f E_b(0) \tag{5.18}$$

and

$$E_b(L) = r_b E_f(L). \tag{5.19}$$

During the model construction, a couple of points have to be further explained in details:

1) In the propagation matrix, β is the complex wavenumber of the uniform medium, and can be written in the form of

$$\beta = n_{eff}k_0 + j(\Gamma g - \gamma)/2 \tag{5.20}$$

In time-domain TMM, the modal gain Γg and the effective refractive index n_{eff} evolve with time, so that the complex propagation constant β will also be a function of time.

Here, Γ is the optical confinement factor and γ is the modal loss of the waveguide, which can be calculated from the transverse field distribution of the laser.

2) The section length has to be set fixed, and equal to the product of the group velocity v_g and the time step dt. For the DFB lasers, the section length is often chosen to be a multiple number (m) of the corrugation periods l, such that the time step dt can be decided as the ratio as $dt = m \cdot l / v_g$.

After construction of the transfer matrix for the optical fields, i.e., photons, inside the laser structure, we now just need to capture the change of carriers in the structure to provide sources of the photon generations.

For each section, we define a carrier density N, whose relation with the injection efficiency η, injection current density J, active region thickness d, spontaneous recombination rate R_{sp}, material gain g and photon density S can be expressed as follows:

$$N(t+dt,k) = N(t,k) + dt\left[\eta\frac{J(t,k)}{ed} - R_{sp}(N(t,k)) - v_g g(t,k)S(t,k)\right]. \quad (5.21)$$

As we see, carrier densities N are updated by using the Euler's formula to approximate the first-order differential equation for the time-dependent carrier conservation relations. This also requires the time step dt to be small enough to guarantee minimization of the finite difference error.

The injection current density J is related to I as $J = I \cdot wL$, and we often can use η to represent efficiency of the current injection into the active region.

The spontaneous recombination rate R_{sp} depends on the carrier density and can be expressed as

$$R_{sp}\left(N(t,k)\right) = AN(t,k) + B\left[N(t,k)\right]^2 + C\left[N(t,k)\right]^3 \tag{5.22}$$

, where A, B and C are the non-radiative, bimolecular and Auger recombination coefficients, respectively.

The peak material-gain g is approximated by a linear function of the carrier density, whose slope is given by the differential gain dg/dN and offset by the transparency carrier density N_{tr} as

$$g_k(N_k, S_k) = \frac{\frac{dg}{dN}\left(N_k - N_{tr}\right)}{1+\varepsilon S_k}. \tag{5.23}$$

Here, ε is the effective gain saturation coefficient [43] and is related to the fundamental saturation coefficient for the material as $\varepsilon = \Gamma \varepsilon_0$. The denominator $\left(1+\varepsilon S_k\right)^{-1}$ as the power-dependent gain compression factor is included to account for the nonlinear effect from photon emissions. As we see, the peak material-gain is inversely proportional to the photon density S, which can be written in terms of the forward and backward optical fields as

$$S_k = \left\{\left|E_{f,k}\right|^2 + \left|E_{f,k+1}\right|^2 + \left|E_{b,k}\right|^2 + \left|E_{b,k+1}\right|^2\right\} / 2v_g \tag{5.24}$$

The output power from the right-hand side can then be given by

$$P_o(t) = (1-R_f)h\upsilon wd\left|E_f(t,L)\right|^2 \tag{5.25}$$

, where $R_f = r_f^2$ is the reflection coefficient of the right end facet, hv is the photon energy and w is the width of the active region.

5.4 Other effects considered in TD-TMM

To consider several intrinsic dynamics of the laser in time-domain TMM, we also want to include a few additional effects into the formulation. These includes the injection caused index change and lasing wavelength shift, the wavelength dependent finite gain profile, the temperature effect and the feedback effect. In the following subsections, we will describe each one correspondingly.

5.4.1 Injection caused index change

One of the effects that also have to be considered, when active region of the laser is exposed to current injections, is the Kramers-Kronig (K-K) relation [44]. Due to the photon-electron interaction mechanism, waveguide refractive index *n* in section *k* will change as the injected carrier increases. To account for this effect, we can approximate the index as a first order perturbation around the transparency carrier density using linewidth enhancement factor α as

$$n_k\left(N(t,k)\right) = n_{i,tr} - \frac{1}{4\pi}\frac{dg}{dN}\left(N(t,k) - N_{tr}\right)\cdot\alpha\lambda\,, \tag{5.26}$$

The subscript *tr* represents quantities at the transparency condition, which occurs when carriers injected into the active region is equal to those consumed by the recombination and absorption mechanisms, i.e., gain is zero or start of population inversion, inside the laser. Note that we can also use other reference index and carrier values available to replace the ones at transparency condition, for instance, no-injection or threshold conditions, but the reference wavelength has to be changed to these conditions, accordingly.

5.4.2 Injection caused wavelength shift

Another effect aside from the index change is the lasing wavelength shift that comes when the structure is under current injection. Governed by the K-K relations, refractive index change will also alter the cavity resonance condition throughout the structure, such that the lasing wavelength will shift within a few nanometres until the system reaches a steady state.

For the implementation in time-domain traveling wave model, the initial wavelength can be first chosen to be around the gain peak, and then automatically corrected by wavelength shift induced by the injection current in every step. This shift can be separated into two parts [42]: one is the reference wavelength drift due to fluctuations of the average refractive index, because the latter one can be written as a linear function of the carrier density that changes with time, as in Eq. (5.27); and the other one is the shift of lasing peak relative to the reference, which can be captured by minimization of the determinant of the cascaded transfer matrix for the whole structure.

For the initial wavelength λ, we can set it to be a reference value λ_{ref}, often around the gain peak as λ_g. Then during the simulation, its shift $\Delta\lambda_{ref}$ due to the current injections can be obtained by averaging the change of refractive index $\overline{\Delta n}$ as

$$\Delta\lambda_{ref} = \frac{\overline{\Delta n}}{n_{tr}}\lambda_{ref} \tag{5.27}$$

, where $\overline{\Delta n}$ is taken over the whole structure as

$$\overline{\Delta n} = \frac{1}{M}\sum_{k} \Delta n_k (N_k) \,. \tag{5.28}$$

Note that the summation is carried out over all M sections, and Δn_k represents the index difference between the present and the transparency values of each section as

$$\Delta n_k = -\frac{1}{4\pi}\frac{dg}{dN}\left(N_k - N_{tr}\right)\cdot \alpha\lambda \tag{5.29}$$

The relative shift $\Delta\lambda_p$ of the resonance peak away from the reference wavelength, due to spatial hole burning and other non-uniform carrier distribution effects, can be captured by the minimization of laser matrix's determinant in each time step as

$$\det\left[A(t)\right] = a_{11}(\lambda) - r_1 r_2 a_{22}(\lambda) - r_1 a_{21}(\lambda) + r_2 a_{12}(\lambda) \,. \tag{5.30}$$

This determinant, once goes to zero, means the effective reflection coefficient of the total structure is infinite, i.e., light can be generated from the device with zero optical input, or lasing threshold is reached at this particular wavelength.

Therefore, the injection induced total lasing wavelength shift $\Delta\lambda$ from the reference wavelength λ_{ref} can now be calculated as the sum of the two shifts as

$$\Delta\lambda = \Delta\lambda_{ref} + \Delta\lambda_p \,, \tag{5.31}$$

and for every time step, the new lasing wavelength has to be updated as

$$\lambda = \lambda_{ref} + \Delta\lambda \,. \tag{5.32}$$

5.4.3 Gain filter

For the tunable lasers and some wide-range wavelength selective structures, such as the FP and the coupled cavity lasers, the finite bandwidth material gain profile [45] and the selective phase-matching condition have to work together physically to provide the mode selectivity and some special optical functionalities. Therefore, in the theoretical design of the time-domain traveling wave model, we have to take into consideration the wavelength dependent gain profile during the simulation; otherwise, the results would be inaccurate, especially for the FP cavity related lasers, whose resonance condition gives all equal mode-selections over the whole wavelength range.

To achieve wavelength selection, by using the finite bandwidth material gain effect in the time domain TMM, as in a real situation, the previously used flat gain profile has to be incremented by an infinite impulse response (IIR) digital filter $H(\lambda)$ to account for the material gain selection [45, 46] as

$$g(\lambda) = g(\lambda_g)H(\lambda) \tag{5.33}$$

, where $g(\lambda_g)$ is the previous peak gain function given by Eq. (5.23). The filter $H(\lambda)$ can be selected as follows [45]

$$\left|H(\lambda)\right|^2 = \frac{(1-\eta)^2}{1+\eta^2-2\eta\cos\left[2\pi c\left(\lambda^{-1}-\lambda_g^{-1}\right)dt\right]} \tag{5.34}$$

, where η is the filter coefficient chosen in between 0 and 1 to control the effective gain width. At the same time, the forward and backward optical fields have to be modified by using the first order IIR filter as

$$\begin{aligned} E_f(t+1,k) &= AE_f(t+1,k)+(1-A)E_f(t,k) \\ E_b(t+1,k) &= AE_b(t+1,k)+(1-A)E_b(t,k) \end{aligned} \tag{5.35}$$

, where A is the weighting parameter defined as

$$A = \eta e^{j2\pi c/\lambda_g \cdot dt} . \tag{5.36}$$

This procedure can then guarantee the correct spectrum to be displayed, as follows, according to the experimentally extracted material gain profile used in the simulation.

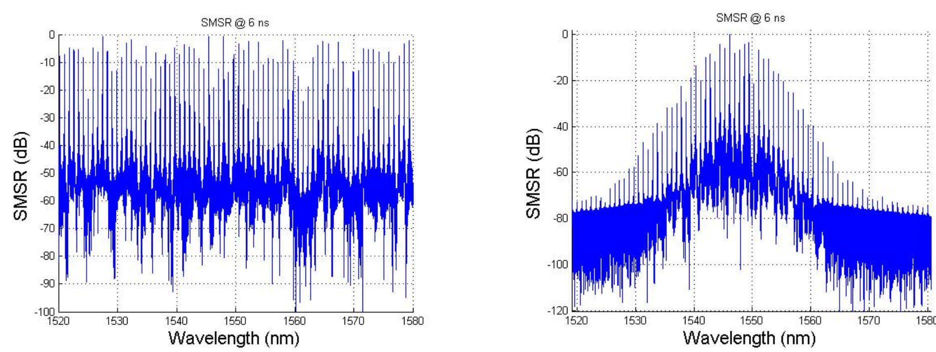

Figure 5.2 Spectrum of FP laser before (left) and after (right) the gain filter is implemented

5.4.4 Temperature effect

As the device temperature changes with different environments and external working conditions, we need to consider the temperature induced lasing wavelength shift and material gain deteriorations, which can be approximated by relating the temperature to the refractive index [41] as

$$\Delta n_{eff,T} = \frac{dn_{eff}}{dT} \Delta T . \tag{5.37}$$

Physically, this is because the atomic spacing of the semiconductor crystal will change according to different temperatures, such that dielectric constant or the refractive index will change accordingly.

Higher injection can also increase the temperature as

$$\Delta T = T - \left[T_0 + \sum_{n=0}^{\infty} \frac{t_n^1}{D_n} I^2 + \sum_{n=0}^{\infty} \frac{t_n^2}{D_n} (I - \frac{e}{E_g} P_{out}) \right], \tag{5.38}$$

, where T_0 is the temperature of the substrate viewed as a constant heat sink, and D_n and $t_n^{1,2}$ are coefficients calculated from the structure as given in [47] as follows:

$$D_n = \left[\frac{(n+1/2)\pi}{h} \right]^2 D \tag{5.39}$$

$$t_n^1 = (-1)^2 \frac{2}{h} \int_0^h R_t(x) R_s(x) \sin\left[\frac{(n+1/2)\pi x}{h} \right] dx \tag{5.40}$$

$$t_n^2 = \frac{2E_g d}{eh} R_t(h) \tag{5.41}$$

Here, h is the distance between the active region and the heat sink, D is the thermal diffusion coefficient, $R_{s,t}$ is the material's series resistance and reciprocal of thermal capacity, and E_g the band gap energy of the active material.

At the same time, differential gain and transparent carrier density in the gain formula have to be modified to include the temperature factor as

$$g_k(N_k, S_k) = \frac{\frac{dg}{dN} e^{-\frac{\Delta T}{T_g}} \ln\left(e^{-\frac{\Delta T}{T_n}} N_k / N_{tr} \right)}{1 + \varepsilon S_k} \tag{5.42}$$

, where T_g and T_n are the characteristic temperature for dg/dN and N_{tr}, respectively. This will affect the resonance condition and lasing threshold of the laser, as is shown in the *L-I* curve as Fig. 5.12 and the lasing spectrum plot as in Fig. 5.3. Parameters needed for those approximations can be extracted from the experiment already done on the same materials.

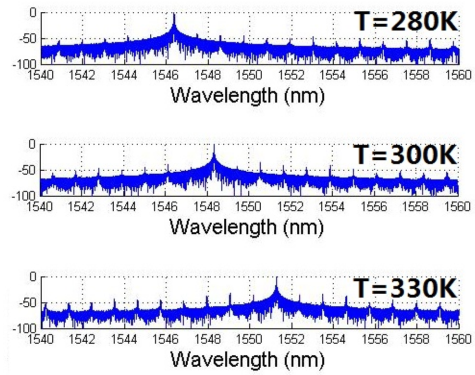

Figure 5.3 Shift of lasing wavelength for a single-mode laser at different temperatures

5.4.5 Optical feedback interferences

Optical feedback as an undesired noise from the transmission network back into the laser structures can sometimes cause the lasers to lose constructive interference, such that the relative intensity noise (RIN) and the power penalty parameters, etc., of the laser can deteriorate dramatically [7, 48-54]. This deterioration of the laser's performance is now usually treated by adding an extra optical isolator in the front of the output facet before entering the network [7], which not only increases the total cost, but also reduces the effective signal strength.

If we want to model the optical feedback effect on the laser's performance by using the time-domain traveling wave method, we can implement by adding to the facet output-field a feedback term, which is a fraction of the previous-time output but with a phase delay.

The formula for Eq. (5.19) can be updated as follows [55],

$$E_b\left(t,L\right) = rE_f\left(t,L\right) - R_0\sqrt{1-r_{feedback}^2}\,E_f(t-\tau,L)e^{-j\omega\tau} \tag{5.43}$$

, where we have assumed the optical network to be connected to the right hand side end facet of the laser and τ is the time delayed when previous output field is partially reflected back into the laser from the external network.

5.5 Procedures of the TD-TMM

After having described the theory of the time-domain traveling wave model, we need to summarize the total procedures that have to be followed sequentially to carry out the simulation.

In the first step, we need to setup the basic structural and material parameters, such as the cavity length and refractive indices. Then, transfer matrices representing the optical fields have to be initialized with lumped spontaneous emissions in the following form as

$$s(k,t) = \sigma(k)\eta(t)e^{j2\pi\delta(t)} \tag{5.44}$$

, where $\sigma(k)$ is given by $\sigma(k) = \Gamma\sqrt{h\nu \cdot g(k)n_{sp}v_g}$ and $\eta(t)$ is any random value from the Gaussian distribution. $\delta(t)$ is a random number from the normal distribution from 0 to 1. The initial field values can also be obtained from a steady-state model, and used as some random seeds. These seeds will be amplified and transferred by the structural matrices so that new field amplitudes and electron carriers can be updated in the forthcoming iterations.

In each iteration, we need to calculate the change of carrier densities by using the Eq. (5.21) and get the index change based on the carrier equation as in Eq. (5.26). Then we can find the new lasing wavelength by calculating the two parts of the wavelength shift $d\lambda$ as Eq. (5.27) and Eq. (5.30). With the help of the carrier and photon density information, we can calculate the peak gain value, on which we can add the finite gain profile function as in Eq. (5.33) to simulate the material's intrinsic wavelength selectivity. Then, we can calculate the effective wave number as in Eq. (5.20) from the gain, index and lasing wavelength information. Now the updated transfer matrix can be obtained for each section, with its matrix elements ready for the field amplitude calculations as in Eq. (5.17).

Additionally, corresponding to the gain filter, the updated field amplitudes also need to be further implemented with the weighted IIR terms as in Eq. (5.35) to acquire the add-on features of wavelength selectivity to the gain. For the field propagations, we also have to consider facet reflection as in Eq. (5.18) and (5.19), as well as the optical feedback interference factors as in Eq. (5.43) during the simulation. Then, at the end of each iteration, we can calculate the photon density from both the forward and backward field amplitudes for the subsections. Facet output power P_0 can also be calculated from Eq.(5.25). After this, the simulation can advance by one step further from t to $t+dt$, and then the whole loop is repeated until the preset total simulation time is reached.

The loop can be charted as follows:

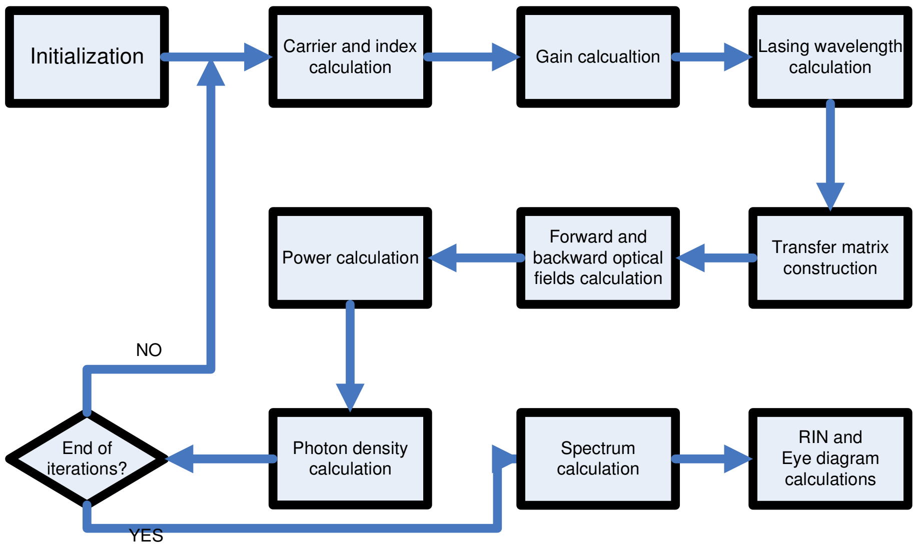

Figure 5.4 Flow chart of TD-TMM

5.6 Numerical Examples

In this section, we apply the time domain traveling wave model to a few numerical examples, so that their performances in simulation can demonstrate the validity and flexibility of this method.

5.6.1 FP laser simulation

As an example of the simplest laser structure, we tested the model's performance on a FP laser as in Fig. 5.5. The simulation parameters are in Appendix A.

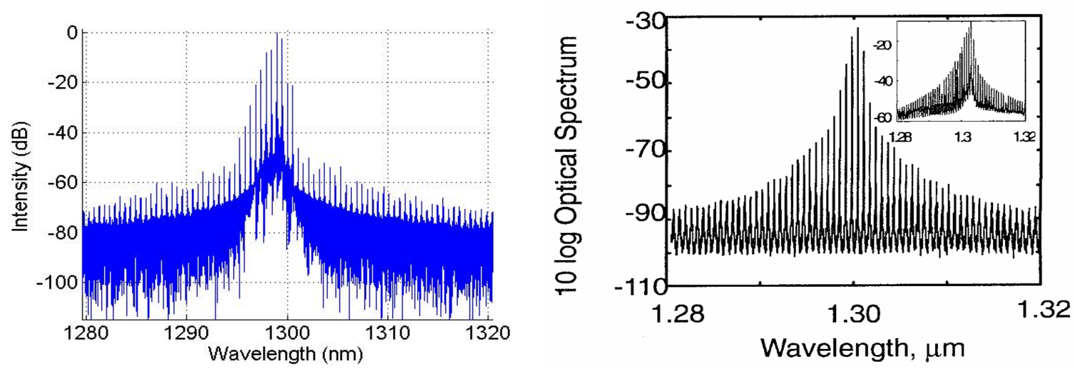

Figure 5.5 Spectrum of an FP laser from (a) TD-TMM simulation (b) literature and experiment (as in the insert) [56]

As we see, our simulation results can well reproduce the spectrum of an FP laser as obtain by the literature and experiment (as in the insert of Fig. 5.5(b)) [56].

Then, we studied the single-slot FP laser [56] as in the following figures, whose parameters used for simulation are the same as above, in Appendix A. And the slot is etched at 1/8 of the length on the left hand side.

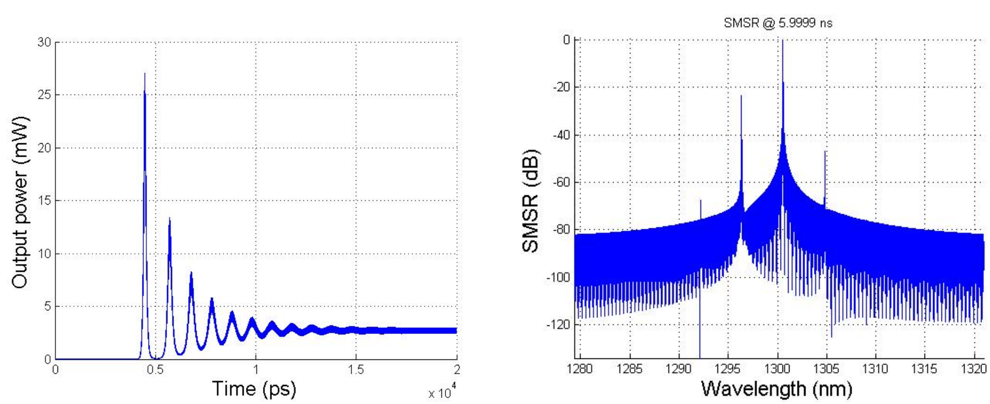

Figure 5.6 Output power and spectrum of a single slot FP laser

From the plots in Fig. 5.6, we can see the mode selection is obtained around 1.3µm with 20dB SMSR, which means the phase matching condition can be modified, by introducing shallowly etched slots purposefully into the FP cavity, for wavelength selection in originally multi-mode lasers.

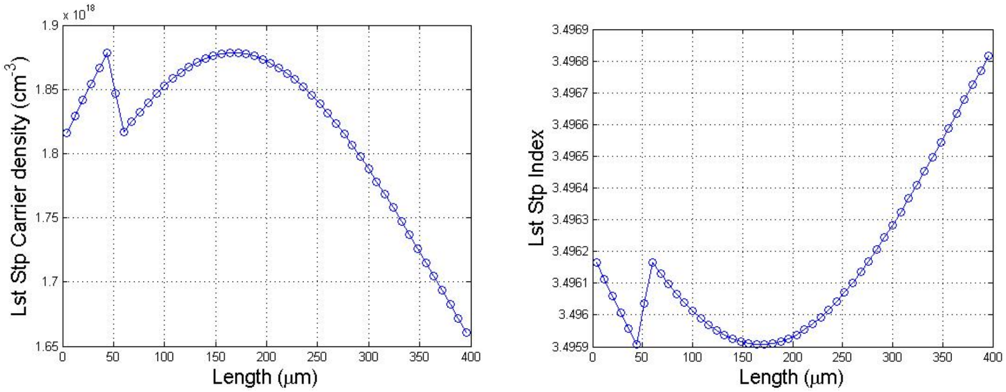

Figure 5.7 Carrier and index distribution of a single slot FP laser

In Fig. 5.7, we can see the carrier and refractive index distributions to be changed according to the slot introduced at 1/8 position. Especially, the index plot shows the slight change of index, due to current injection and K-K relations.

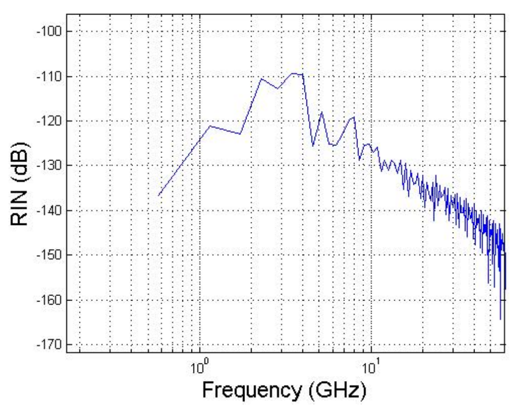

Figure 5.8 RIN of single slot FP laser

From the RIN plot in Fig. 5.8, we can see the noise level of single-slot FP laser is low and the resonance frequency is around 3 GHz, which indicates the significance of the slots on laser spectrum, if properly allocated.

5.6.2 DFB laser simulation

As the second example of TD-TWM, we calculated the DFB structure [57, 58], whose parameters is listed in Appendix B.

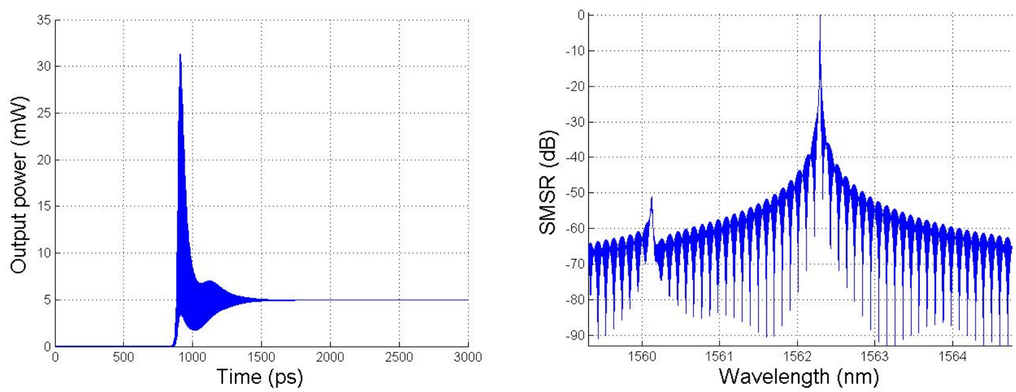

Figure 5.9 Output power and spectrum of the DFB laser

The power and spectrum in Fig. 5.9 indicate the effectiveness of the constructive interference and selection by the periodically etched slots in DFB laser, which can give a 50 dB SMSR if no external feedback perturbations are present.

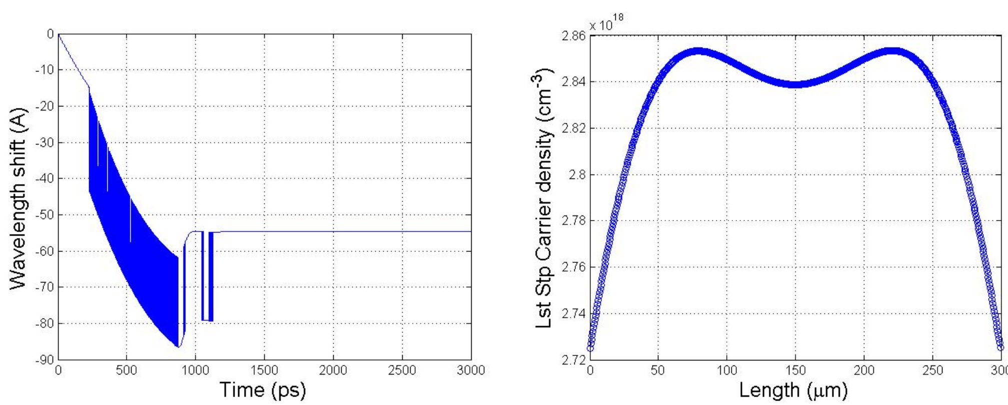

Figure 5.10 Lasing wavelength shift and carrier distribution of the DFB laser

In Fig. 5.10, we can see the wavelength shift to be accompanied by the output power plot during the simulation, such that they both reach the steady state after a certain time of set-up periods. The carrier and photon distribution in Fig. 5.10-11 also show the possible spatial hole burning effects, where density of carriers is lower around the facets of the cavity, corresponding to the relatively high photon density for the output.

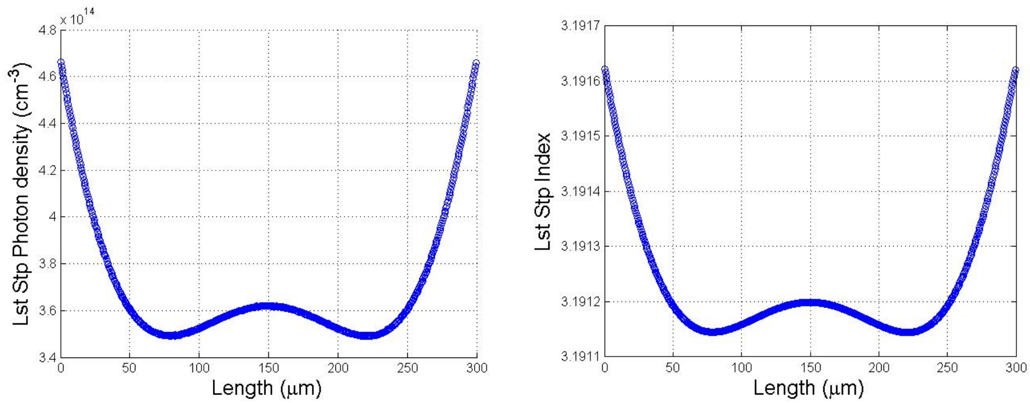

Figure 5.11 Photon and index distribution of the DFB laser

To demonstrate the model's ability in estimating lasing properties when device temperature is also taken into consideration, we calculated the following graphs for L-I curve and large signal modulation by square wave-forms at 0.5GHz, to compare with the literature. From the plot, we can see that the TD-TMM can reproduce the reference results with high accuracy. For certain increase of the environment temperature, the lasing behavior in terms of the threshold current and L-I curve slope are significantly changed. The saturation of output power can also be observed, as indicated by the decrease of slope at higher injections in Fig. 5.12(a).

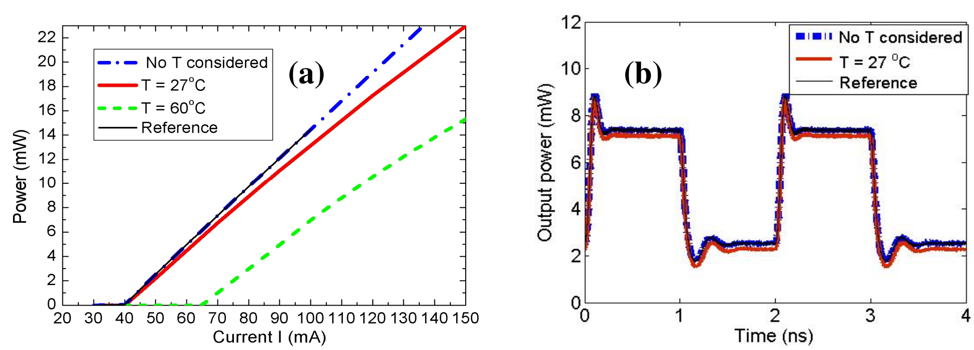

Figure 5.12 (a) L-I curve and (b) large signal modulation of a DFB laser verified from the time-domain traveling wave model

5.7 Summary

In this chapter, we have described the time-domain transfer matrix model and applied it on several examples to test the method's validity and flexibility. In the derivation, we also added the gain profile, temperature and feedback considerations into the model to improve the original TD-TMM's applicability and versatility. In the simulation, we have demonstrated its accuracy and efficiency on examples of the ordinary FP, single-slot FP and DFB lasers, to include both periodic and non-periodic cases. This also shows the method to be applicable on non-periodic DM lasers that we are going to study in the following chapters.

Chapter 6
Simulation and optimization of discrete mode laser

6.1 Introduction

Semiconductor lasers made of Fabry-Perot cavities are perhaps the most straightforward optical devices to be fabricated. However, the multimode emission property of the conventional FP lasers has limited their applications in the long-haul fibre optic communications, because there the single-mode operation with high spectral purity is desired. This has led to the development of many techniques, including the DFB, DBR and coupled cavity laser designs, etc. In those approaches, Bragg gratings are the most commonly used structures to provide mode filtering and wavelength selection functionality, while others utilize phase matching conditions of the resonance cavities to pick up modes of interest out of their FP mode-basis. More specifically, distributed Bragg reflector lasers use frequency-selective passive mirrors to force only the selected FP cavity modes to lase; while distributed feedback lasers, whose Bragg gratings are etched above the active region along the whole cavity length, use both the multiple scattering from periodic gratings and the round-trip phase matching condition to determine the lasing-mode.

However, while working with the DFB and DBR lasers, strong external feedbacks [7, 51-53] from the high density HTTx networks [8, 59] components, such as the connecters and splitters, can disturb the constructive interference of the cavity more heavily formed by Bragg gratings than by cleaved facets. Therefore, the DFB and DBR lasers' static and dynamic performances can be seriously affected [60-63]. This can be understood by realizing that the huge number of gratings etched in those lasers must delay the reconstruction of the longitudinal phase matching condition at presence of the external feedbacks, such that output of the devices will exhibit noisy and mode-hopping states in a more serious manner. In an FP laser, the feedback disturbance equally affects all longitudinal modes of the cavity, such that its output shows much less disturbance than that of the Bragg-grating based structures. Also, the fabrication of such devices involves a second or third time epitaxial growth after high resolution lithography [64], which not only increases the manufacturing complexity but also the cost. This re-growth procedure can affects the reliability of aluminum-based ternary and quaternary materials [65], such that it forces the devices to use of aluminum free quaternary systems at the price of poor performance at high temperature.

By eliminating the re-growth procedure, we can vertically grow the DBR laser onto the wafer as VCSEL [15, 66-71] for "vertical cavity – surface emitting laser", which can work in single mode condition. The principle of this design is it has very short resonance cavity so that number of the supported modes can be limited until only one wavelength is allowed. However, despite the many performance and manufacturing advantages of this structure, such as the low threshold current [70] and on-wafer testing

[72], etc., it shows high wavelength dependence on the thickness variations of the epitaxially grown layers. As in Ref. [15], a 1% miscalibration in the epitaxial layer thickness can result in a 10 nm wavelength shift for the selected single mode. This imposes stability issues on the laser's performance for applications in the optical communication systems, which brings corresponding higher requirement for the manufacturing accuracy and increases the production cost. Also, as we know, the short cavity length for amplification must demand the Bragg mirrors to have very high reflectivity for lasing, which requires a high index contrast of adjacent layers or a large number of weak-contrast periodic ones. However, the first option is hampered by having a higher scattering loss, while the second one requires a too complex structure to manufacture.

For the coupled-cavity lasers, there are alignment problems for the coupled mirrors [73, 74], and mode-hopping problems for any unintentional temperature and current fluctuations [75-77]. So in many cases, they are also used as tunable lasers for the reason that their selected mode can be shifted by controlling the external temperature or injection level under certain conditions [78-83].

Therefore, after having introduced the above lasers thus far, we need to describe a new design as in Ref. [65, 84-89], which is believed to address all the previously discussed problems of lasers for application in optical communication networks, and to provide a single mode lasing spectrum with high side-mode suppression ratio (SMSR). By selectively etching 10~100 shallow slots on the longitudinal ridge of a FP cavity, the discrete-mode (DM) lasers that are re-growth free and performance stable under various conditions, can be obtained. The etched slots act as small perturbations and mode selectors inside the FP cavity, and introduce very low scattering loss. Also, besides the many promising advantages over all other candidate lasers for optical communication applications, especially the FTTx systems, DM laser is also robust at high level of optical feedback from the other network components [65, 84, 90-92], and is stable when injection or environment induced temperature change is involved [65, 93].

6.2 Transfer matrix scheme and threshold gain design

In this section we will use the transfer matrix method to describe the logics of the threshold gain design for DM lasers, in which we can find the discrete positions of those etched slots are Fourier transform of the laser's gain threshold in continuous wavelength space. As having described in the previous chapters about the general transfer matrix scheme in capturing field propagations in the laser cavities along the longitudinal direction, we can use this method to connect all the sections' scattering and propagation matrices to obtain total transfer matrix for the structure. By applying boundary conditions at the two ends, we can find a continuous curve to represent relations of the modal gain's lasing threshold with respect to different wavelength values. Then a design procedure based on this curve can be carried out and inversely we can decide positions of the slots to be etched along the FP cavity. In the following, we will describe the procedures of DM laser threshold design as in Ref [89], to pave the way for next chapter's static and dynamic property optimizations of the structure.

6.2.1 Transfer matrix scheme

As shown in Fig. 6.1, a number of shallow slots are etched onto the FP cavity, with the total length L_c and end facet reflectivities r_1 and r_2 [89].

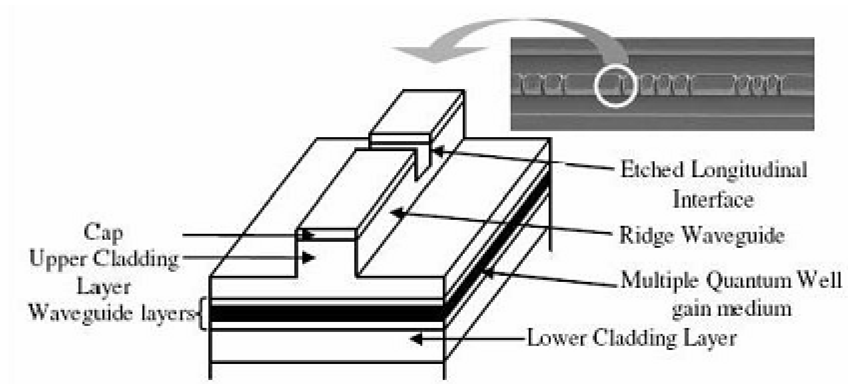

Figure 6.1 Structural layer-out of the DM laser [89].

All the slots in 3D real structure can be approximated in the 1D model by index differences along the laser's longitudinal direction as in Fig. 6.2. Then, the transfer matrix method can be used to connect those separate index discontinuities and force facet boundary condition on both ends.

Figure 6.2 1D approximation of the DM laser along the longitudinal direction.

For each of the slot, we can show in detail in the following figure as in Fig. 6.3, where slot center z_i and width l_i are the two basic parameters to define their positions. The indices of etched and un-etched parts are n_2 and n_1, respectively. Here, we have to notice that for convenience of the future derivations using the total transfer matrix, we need to define the boundaries of each slot as the close proximity outside of the etching marked by the dashed lines.

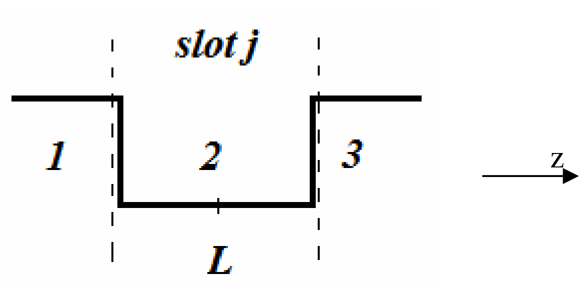

Figure 6.3 Slot of length L etched along the longitudinal direction.

The slot matrix S can be represented by the elementary transfer matrices of index jump T and uniform period P as described previously as

$$S = T_{12} P_2 T_{21} \tag{6.1}$$

where

$$[T_{12}] = \begin{bmatrix} \dfrac{n_1 + n_2}{2n_1} & \dfrac{n_1 - n_2}{2n_1} \\ \dfrac{n_1 - n_2}{2n_1} & \dfrac{n_1 + n_2}{2n_1} \end{bmatrix} \tag{6.2}$$

and

$$[P_i] = \begin{bmatrix} e^{-j\beta_i L_i} & 0 \\ 0 & e^{j\beta_i L_i} \end{bmatrix}. \tag{6.3}$$

For the total slots without considering two end facets, we have

$$M = P_1 S_1 P_3 S_2 P_5 \ldots S_{N-1} P_{2N-1} S_N P_{2N+1}. \tag{6.4}$$

Then, as an important assumption for this design method, we have to require the slots to be shallowly etched and of small length, so that index difference Δn (between n_1

and n_2) and their induced perturbations to the FP cavity can be small enough to enable the expansion of M matrix to the first order of $\Delta n / n$. There is also recent research [94] to relieve this small perturbation requirement to allow arbitrary etching depth and length of the slot, but as we are more interested in designs with as few and as shallow slots as possible, we will limit the discussion in this thesis without considering the arbitrary slot cases.

For purpose of expansion and approximation of the total slot matrix M, we can re-write the slot matrix in Pauli spin matrix form as

$$S_j = P_{2j} - q^- \sin\left(\beta_{2j} L_{2j}\right)\sigma_y + j\left[1 - q^+\right]\sin\left(\beta_{2j} L_{2j}\right)\sigma_z \tag{6.5}$$

, where

$$\sigma_y = \begin{bmatrix} 0 & -j \\ j & 0 \end{bmatrix} \text{ and } \sigma_z = \begin{bmatrix} 1 & 0 \\ 0 & -1 \end{bmatrix}, \tag{6.6}$$

and

$$q^- = \frac{q - q^{-1}}{2} \text{ and } q^+ = \frac{q + q^{-1}}{2} \tag{6.7}$$

, with $q = n_1 / n_2$ or $q = n / (n + \Delta n)$. To the first order of $\Delta n / n$, we can expand q^+ and q^- that further lead to S_j and M's approximations as

$$q^- = -\frac{\Delta n}{n} + O\left(\frac{\Delta n}{n}\right)^2 \text{ and } q^+ = 1 + O\left(\frac{\Delta n}{n}\right)^2 \tag{6.8}$$

and

$$S_j = P_{2j} + \frac{\Delta n}{n}\sin\left(\beta_{2j} L_{2j}\right)\sigma_y + O\left(\frac{\Delta n}{n}\right)^2 \tag{6.9}$$

$$M = P\left(\sum \beta_i L_i\right) + \frac{\Delta n}{n} \sum_{j=1}^{N} \sin\left(\beta_{2j} L_{2j}\right) P_{0j} \left[P_{j(N+1)}\right]^{-1} \sigma_y, \tag{6.10}$$

where

$$P_{jk} = P\left(\sum_{i=2j+1}^{2k-1} \beta_i L_i\right) \tag{6.11}$$

and the relation $\sigma_y P_i = P_i^{-1} \sigma_y$ is used.

From the expanded matrix *M*, we can find the structure's lasing threshold by requiring its boundary condition of two end facets to generate optical power without any external light fed in. Mathematically, we can calculate the total reflectivity *R* of the structure from its overall transfer matrix M_{total} as

$$M_{total} = \begin{pmatrix} 1 & -r_1 \\ -r_1 & 1 \end{pmatrix} M \begin{pmatrix} 1 & r_2 \\ r_2 & 1 \end{pmatrix} \tag{6.12}$$

$$R = \frac{M_{12}^{total}}{M_{11}^{total}} = \frac{r_2 M_{22} + M_{21} - r_1 r_2 M_{12} - r_1 M_{11}}{M_{11} - r_1 r_2 M_{22} + r_2 M_{12} - r_1 M_{21}} \to \frac{finite}{0} \to \infty \tag{6.13}$$

, which gives the governing equation of the laser's threshold as

$$M_{11} - r_1 r_2 M_{22} - r_1 M_{21} + r_2 M_{12} = 0. \tag{6.14}$$

By putting the approximate *M* matrix as Eq. (6.10) into the above equation, we can obtain the first-order approximate governing equation as

$$1 = r_1 r_2 \exp\left[2i \sum_{s=1}^{2N+1} \left(\beta_s L_s\right)\right] + i \frac{\Delta n}{n} \sum_{j=1}^{N} \sin\left(\beta_{2j} L_{2j}\right) \left[r_1 \exp\left(2i\phi_j^-\right) + r_2 \exp\left(2i\phi_j^+\right)\right] \tag{6.15}$$

, where $\phi_j^{\pm} = \phi_j^{\pm}{}' + i\phi_j^{\pm}{}''$ is the total phase shift ($\phi_j^{\pm}{}'$) and gain ($\phi_j^{\pm}{}''$) from the *j*-th slot center to the right (+) and left (-) of the laser's corresponding end facets. This approximation also requires the slot-slot and slot-external mirror scatterings within the structure to be all neglected due to the small perturbations from each slot. The above equation could be solved by separating it into real and imaginary parts so that threshold gain and phase equations can be obtained at the same time.

For the imaginary part, if the net gain $g_s\left(=\beta_s''\right)$ is assumed to be uniformly distributed along the cavity, we can write the following relation as

$$\phi_j^-{}'' = \left(\frac{1}{2}+x_j\right)\sum\left(g_s L_s\right) \tag{6.16}$$

and

$$\phi_j^+{}'' = \left(\frac{1}{2}-x_j\right)\sum\left(g_s L_s\right) \tag{6.17}$$

, where x_j represents the relative distance from each slot center to the laser's longitudinal center, as a fraction of the total cavity length, i.e., $-1/2 < x_j < 1/2$. This quantity will be used in the future to designate slot positions inside the FP cavity.

For the phase part, we can also write the following relation for each slot as

$$\sum n_s L_s k_0 = \phi_j^+{}' + \phi_j^-{}'' = m\pi + \delta_m \tag{6.18}$$

, where *m* is the longitudinal-mode number of the FP cavity and δ_m is the relative phase shift to the *m*-th mode due to perturbations of the etched slot *j*. Therefore, we can find the threshold and phase shift for a DM laser from the above real and imaginary parts of the Eq. (6.15) as

$$\gamma_m = \gamma_m^{(0)} + \frac{\Delta n}{n}\gamma_m^{(1)} + O\left(\frac{\Delta n}{n}\right)^2 \tag{6.19}$$

$$\delta_m = \frac{\Delta n}{n}\delta_m^{(1)} + O\left(\frac{\Delta n}{n}\right)^2 \tag{6.20}$$

, where in Eq. (6.19)

$$\gamma_m^{(0)} = \frac{1}{L_c}\ln\frac{1}{|r_1 r_2|} \tag{6.21}$$

is the original FP cavity's lasing threshold, independent of mode number *m*, and

$$\gamma_m^{(1)} = \frac{1}{L_c\sqrt{|r_1 r_2|}}\sum_{j=1}^{N}\sin\left(n_{2j}k_0 L_{2j}\right)\left[A_j^-\sin 2\phi_j^-{}' + A_j^+\sin 2\phi_j^+{}'\right] \tag{6.22}$$

with

$$A_j^- = |r_1|\exp\left(x_j L_c \gamma_m^{(0)}\right) \text{ and } A_j^+ = |r_2|\exp\left(-x_j L_c \gamma_m^{(0)}\right). \tag{6.23}$$

For Eq.(6.20), the first order phase shift $\delta_m^{(1)}$ is

$$\delta_m^{(1)} = \frac{-1}{2\sqrt{|r_1 r_2|}}\sum_{j=1}^{N}\sin\left(n_{2j}k_0 L_{2j}\right)\left[A_j^-\sin 2\phi_j^-{}' + A_j^+\sin 2\phi_j^+{}'\right] \tag{6.24}$$

, which is much smaller than $\gamma_m^{(1)}$ and can be neglected at small perturbation index Δn. This also implies at the first order of Δn that Eq. (6.24) can be simplified as

$$\sin\left(2\phi_j^-{}'\right) = \sin\left[2\left(m\pi - \phi_j^+{}'\right)\right] = -\sin\left(2\phi_j^-{}'\right) \approx \cos\left(m\pi\right)\sin\left(2x_j m\pi\right) \tag{6.25}$$

, which leads to further simplification of Eq. (6.22) as

$$\gamma_m^{(1)} = \frac{1}{L_c\sqrt{|r_1 r_2|}}\sum_{j=1}^{N}\sin\left(n_{2j}k_0 L_{2j}\right)\left(A_j^- - A_j^+\right)\cos\left(m\pi\right)\sin\left(2x_j m\pi\right). \tag{6.26}$$

From the above derivation, we can see that the lasing threshold now depends on Eq.(6.23), which is directly related to the slot positions x_j and facet reflection coefficients r_1 and r_2. By careful design and arrangement of the slot positions, we can engineer the gain threshold and thus control lasing behaviours of a previously multi-mode FP laser.

6.2.2 Threshold gain design for single mode laser

In this section, we will work on the previously derived formulas for the slot and threshold gain relations and design single mode lasers from this modified FP structures by maximizing the gain difference between any chosen wavelength and all other background wavelengths.

From Eq.(6.26), we can see that amplitude of the threshold gain is mainly determined by the function $M(x_j)$ as

$$M(x_j) = A_j^- - A_j^+ = |r_1|\exp\left(x_j L_c \gamma_m^{(0)}\right) - |r_2|\exp\left(-x_j L_c \gamma_m^{(0)}\right) \tag{6.27}$$

, where if $|r_1| = |r_2|$, we can further have

$$M(x_j) = 2|r_1|\sinh\left(x_j L_c \gamma_m^{(0)}\right). \tag{6.28}$$

The other factor is $\cos(m\pi)\sin(2x_j m\pi)$, which can be expanded around the selected mode number $m_0\,(= m - \Delta m)$ as

$$\begin{aligned}&\cos(m\pi)\sin(2x_j m\pi)\\&= \cos(m_0\pi)\cos(\Delta m\pi)\left[\sin(2\pi x_j m_0)\cos(2\pi x_j \Delta m) + \cos(2\pi x_j m_0)\sin(2\pi x_j \Delta m)\right].\end{aligned} \tag{6.29}$$

To minimize the threshold gain at the selected mode m_0, when $\Delta m = 0$, we can require the slot to be etched at positions where the following relation is satisfied

$$\sin\left(2\pi x_j m_0\right) = \pm 1. \tag{6.30}$$

Then to decide the number and depth of the slots needed to be etched, we have to resort to either physical idea, as in solid state physics that the wave number space properties all correspond to the atomic positions in real space through the Fourier transform [89]; or we can numerically test the possible slot positions and compare its resultant threshold with its target function to minimize their difference, as has been described in Ref. [94].

To be able to etch discrete slots as few as possible, we can use the first scheme and do Fourier transforms of a desired threshold gain to obtain its corresponding slot positions in the FP cavity. For example, if we want to design single mode lasers, the threshold gain can be chosen as a sinc function, which has a minimum in the middle for the lasing wavelength and all other higher values for wavelengths in the non-lasing background. Also, to concentrate slots in a finite-length FP cavity, we need to have periodicity in the threshold target function, which can be done by adding sinc functions periodically for different modes and dampening them by an exponential decay envelope for modes away from the central lasing wavelength. Then the Fourier transform would give density of the slots as sum of the Gaussians as

$$\Gamma_m(x) = \exp\left[-\pi\frac{\left(x - ms\right)^2}{\sigma^2}\right]. \tag{6.31}$$

By integrating it with inverse of the modulation function $M(x_j)$ over the entire cavity, we can find each slot's center position as follows

$$A\sum_n \int_{x_0}^{x_j} \left[M(x_j)\right]^{-1} \Gamma_n(x_j)dx = j - 1/2 \tag{6.32}$$

, where j is the slot number and A is the normalization constant to control total number of slots. This equation gives the gross information about where to etch the slots, although we still need to further adjust their positions to match the phase condition of constructive interference exactly as follows

$$\phi_j^{-}{}' = \frac{\left(x_j + 1/2\right) + \left(N_j^{-} + 1/2\right)\left(l / L_c\right)\Delta n / n}{1 + N\left(l / L_c\right)\Delta n / n} \sum \theta_i{}' \tag{6.33}$$

, where N_j^{-} is the number of slots to the left of slot j.

From threshold analysis using the above discussed inverse method, we calculated a DM laser structure, whose slot distribution is shown in Fig. 6.4. For detailed data of those slot positions, please refer to Appendix C for corresponding information.

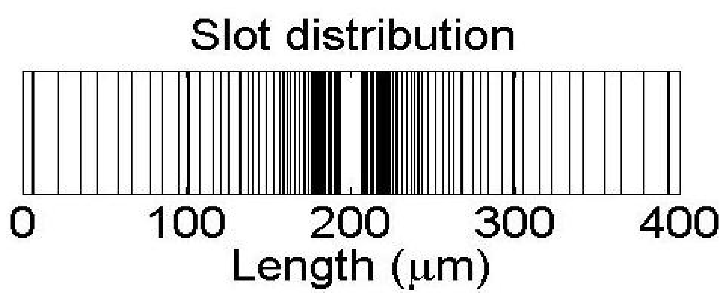

Figure 6.4 Distribution of 90 slots along the longitudinal direction for a symmetric DM laser.

The threshold gain profile of this DM laser can be shown in Fig. 6.5 as

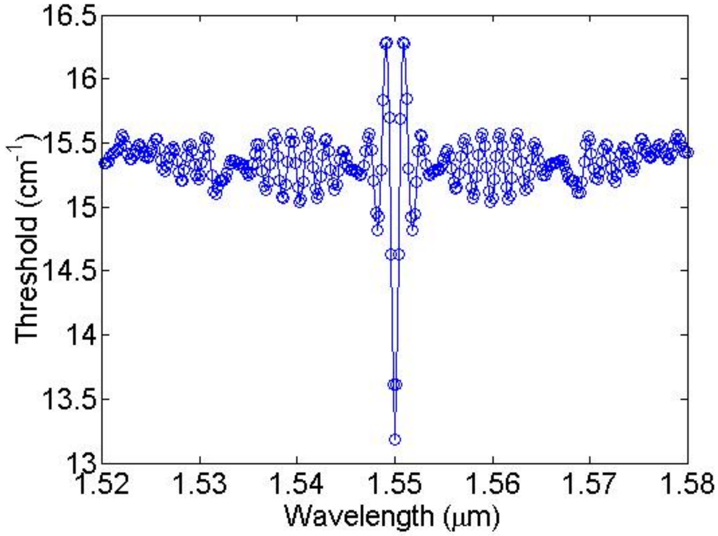

Figure 6.5 Threshold gain profile of the 90-slot DM laser.

, where this example uses 90 slots of index contrast of $\Delta n = -0.005$ on the FP cavity (substrate index $n = 3.2$). As we see, the design of threshold gain profile for single wavelength selection around 1.55μm can be achieved, by careful positioning of the slots along the FP cavity. In the following subsections, we will use the previously derived TD-TMM in Chapter 5 to simulate and optimized the lasing performance of this DM structure.

6.3 Numerical Results from TD-TMM Simulation

6.3.1 DM laser in CW condition

As described above, after having obtained the slot positions, we used the TD-TWM model to calculate its lasing spectrum, as in Fig. 6.6, whose carrier and index distributions are also shown in Fig. 6.7.

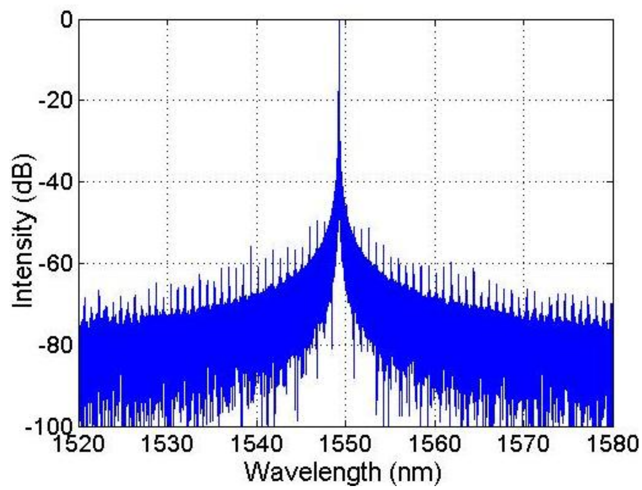

Figure 6.6 Spectrum of DM laser calculated from TD-TWM

From the plots, we see high purity lasing spectrum of DM laser, at no external perturbations and modulations. The SMSR could reach 40-50 dB around 1.55μm.

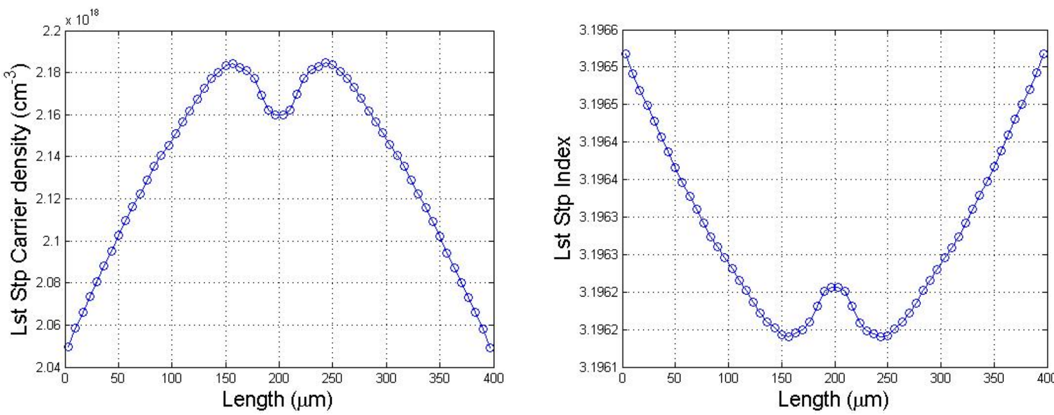

Figure 6.7 Carrier and index distribution for the DM laser

The carriers and index profiles as in Fig. 6.7 are similar to that of FP, only with changing distributions around the slot-densely-etched positions as indicated in Fig. 6.4.

Further, the lasing wavelength and SMSR with respect to the injection current are shown in Fig. 6.8(a) to indicate the wavelength shift at different pumping levels. Red shift can be seen above the 20 mA threshold and stable while slight improvement of SMSR can also be observed. By varying injection current at different temperatures, we can obtain the light-current relation as in Fig. 6.8(b), which demonstrates the T-dependent threshold current and L-I curve slope of the laser. At higher temperature, I_{th} increases while the slope decreases at a greater speed.

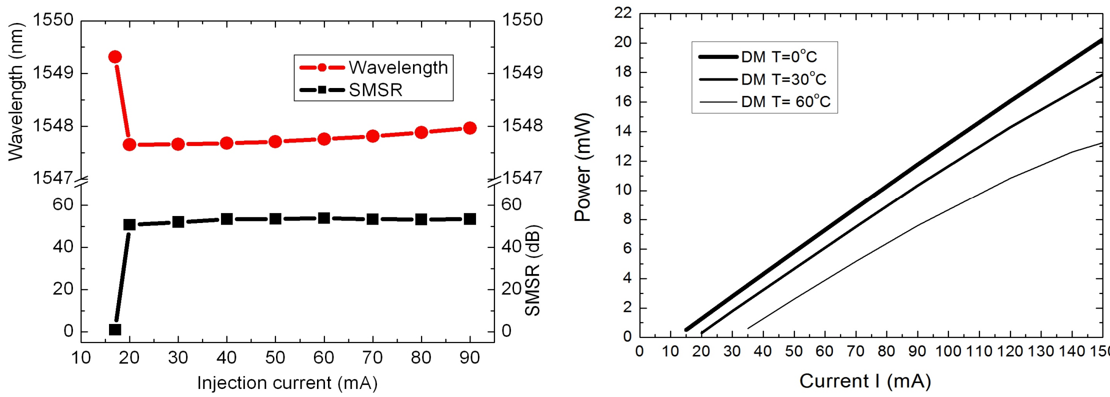

Figure 6.8 SMSR and lasing wavelength shift, and L-I curve at different temperture, of the symmetric DM laser from time-domain traveling wave model

Then, for the small signal analysis of the laser, we calculated the optical response at room temperature for three different base currents as in Fig. 6.9, from which we can see that the relaxation oscillation frequency increases from 1GHz to around 5GHz at higher injections.

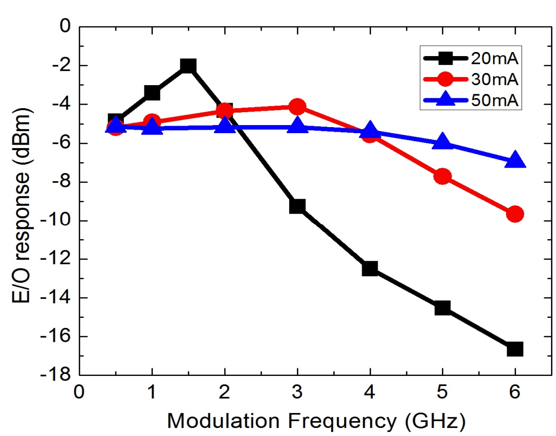

Figure 6.9 Small signal analysis for DM laser at different base current conditions

6.3.2 DM laser in modulation and feedback condition

For large signal modulation situation, we applied an alternating injection current switched between 30 mA and 50 mA to the laser at 10 Gbit/s as shown in Fig. 6.10, from which we can see clean output power and smooth lasing wavelength along the high speed modulation.

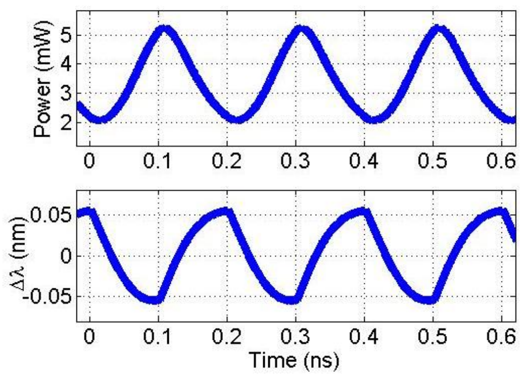

Figure 6.10 Large signal analysis for DM laser with power and wavelength shift plots at 10 Gbit/s

To see the optical feedback influence on DM structure's lasing performances, we further included a high level backward reflection of up to -25dB, i.e., $r_{feedback} = 0.05$, to the right exit end of the laser, whose output power and lasing wavelength shift, as well as the overlapped spectrum taken at different simulation times, are plotted in Fig. 6.11(a). The reason to plot spectra on top of each other is to see the possible mode-hopping during modulation, especially when injection current is switched between 0/1.

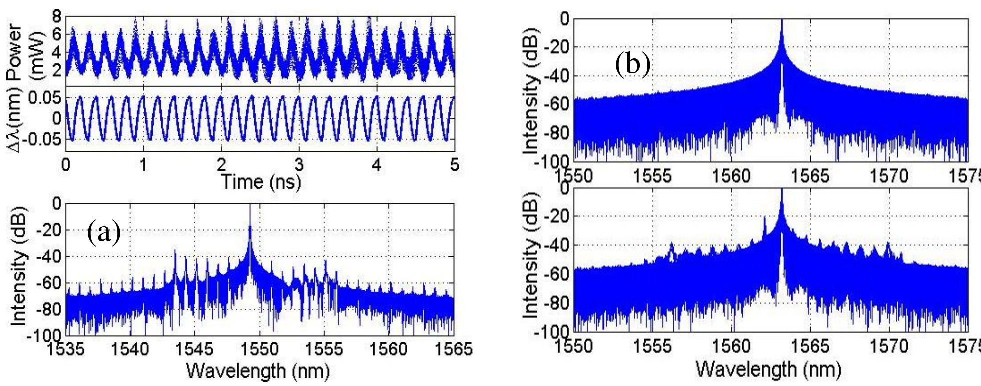

Figure 6.11 Output power, lasing wavelength shift and spectrum for (a) DM laser under -25dB external optical feedbacks and (b) DFB laser without (upper) and with -25dB feedback (lower), at 10 GHz modulation. Spectrum plot is obtained by overlapping the different spectrums sampled at different time positions

Comparing Fig. 6.11(a) with Fig. 6.6 and 6.11(a), we can see that the DM laser can maintain high single-mode spectrum under strong feedback and fast modulation condition, as experimentally described in Ref.[65, 92]. Central lasing wavelength is also changing smoothly according to the injection modulation. For further comparison, a DFB laser with the same structural and material parameters, especially the same designed threshold gain difference and exit-end facet reflectivity, is calculated before and after feedback is applied, as in Fig. 6.11(b). From those graphs, we can see the different effects of feedback on the two structures, i.e., DFB is sensitive to feedback mostly on its neighboring mode, such that mode hopping can occur to this vicinity wavelength; while DM feedback sensitivity is shared by all other suppressed FP modes covered by the material gain profile, such that the total sensitivity is reduced, but at the price of possible mode hoppings to wavelengths far away.

6.4 DM laser optimizations

After having described the inverse method, as in the previous subsection, to design the single mode DM laser, which uses the Fourier analysis to transform desired threshold gain profile to certain distributions of the slots onto the FP cavity, we need to further optimize the structure in time domain, due to the many structural solutions that we can have from one initial threshold gain profile. Under various external and modulation conditions, we can carry out the sensitivity study of some of the key design parameters in TD-TMM, as in Chapter 5, to pick out the best solution that can suite the optical communication applications.

6.4.1 Design parameters

From the structural design point of view, we have several degrees of freedom to tailor the DM laser for its best performance in output spectrum and stability. Dynamically, some of the lasing properties can also change due to the rapid switching of modulation current and temperature, such that we need to study and optimize the corresponding parameters to minimize some of the deteriorations while maintain certain performance criterions on the same level.

The main parameters that can be considered for DM laser optimization are the slot number, etching depth, width and distribution, etc. The distribution can mean symmetry property, i.e., either symmetric gratings on the whole cavity with respect to the structural center, or asymmetric gratings on only half of the structure and no slot the other half but with high reflective facet at the end, etc; or it can mean part of the longitudinal section is etched with slots while others are etching-free.

We first examine the number of slots effect on the laser performance:

The following is 11 slot asymmetric case:

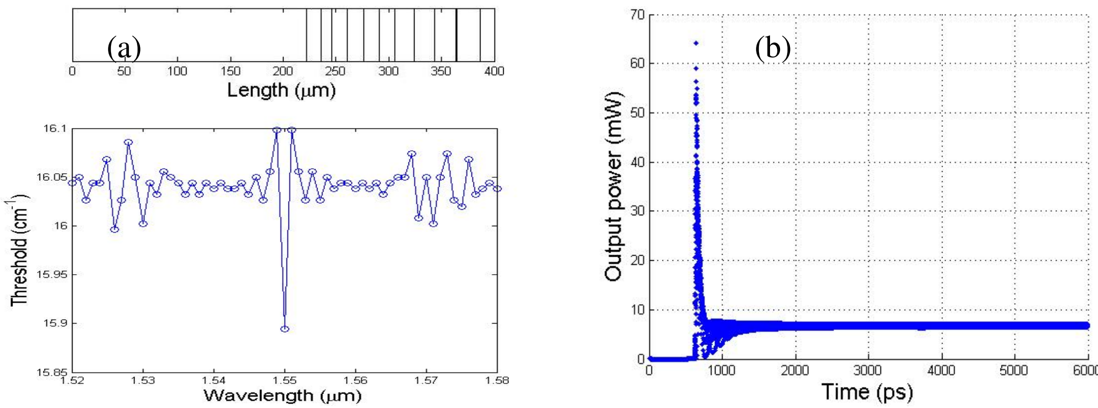

Figure 6.12 (a) 11-slot asymmetric DM laser structure and threshold gain; (b) output power from TD-TWM simulation.

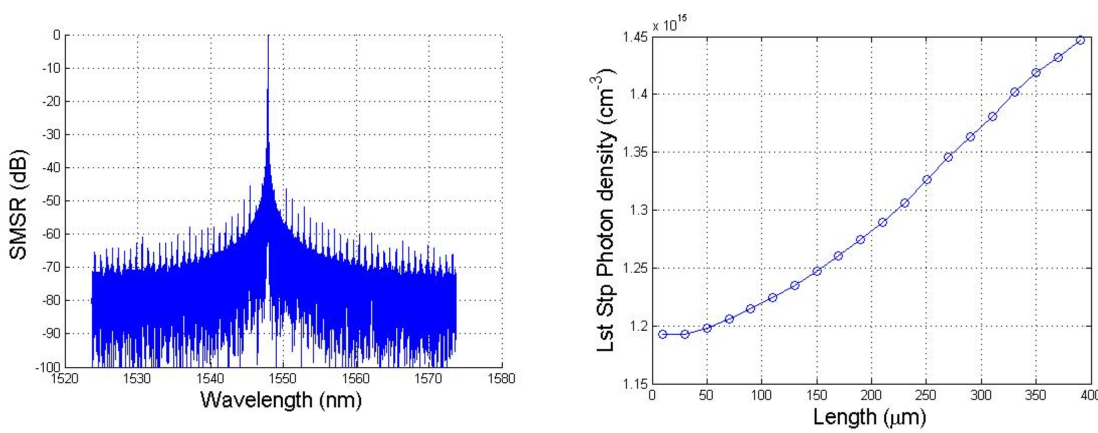

Figure 6.13 11-slot asymmetric DM laser spectrum and photon distribution.

From the plots in Fig. 6.12-13, we see the minimum number of slots needed for single-mode FP laser design is around 10 slots, while threshold gain difference of around 0.15

cm^{-1} in DM laser can hardly make DFB laser work in single mode. The photon distribution is also increasing from the high reflective end to the right-end output facet.

The following is the 15-slot asymmetric case:

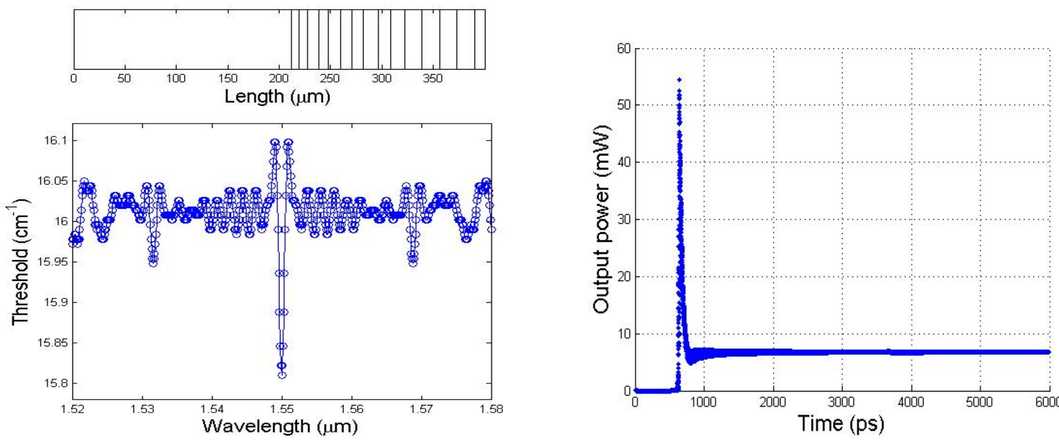

Figure 6.14 (a) 15-slot asymmetric DM laser structure and threshold gain; (b) output power from TD-TWM simulation.

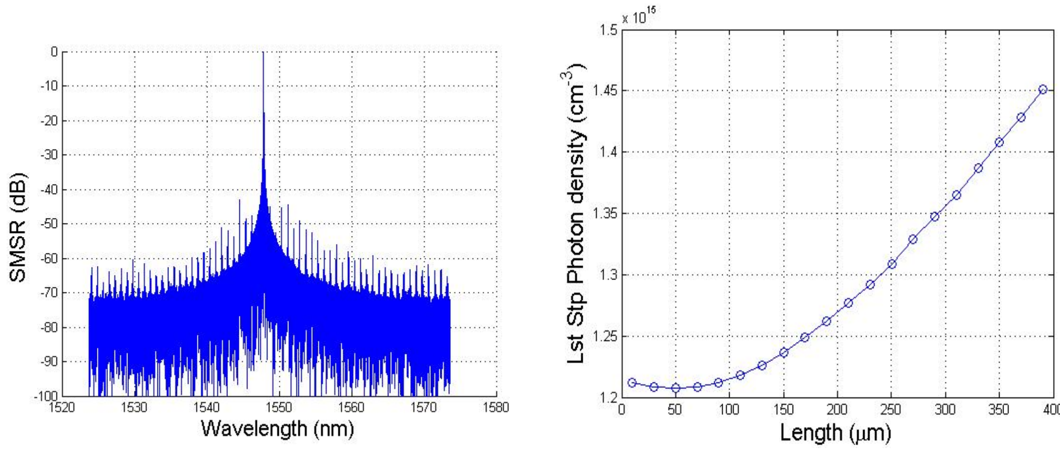

Figure 6.15 15-slot asymmetric DM laser spectrum and photon distribution.

Here, in Fig. 6.14-15, we see the wavelength selection is maintained around 40 dB SMSR and the photon density profile is similar as in the 11-slot case.

The following is 48 slot asymmetric case:

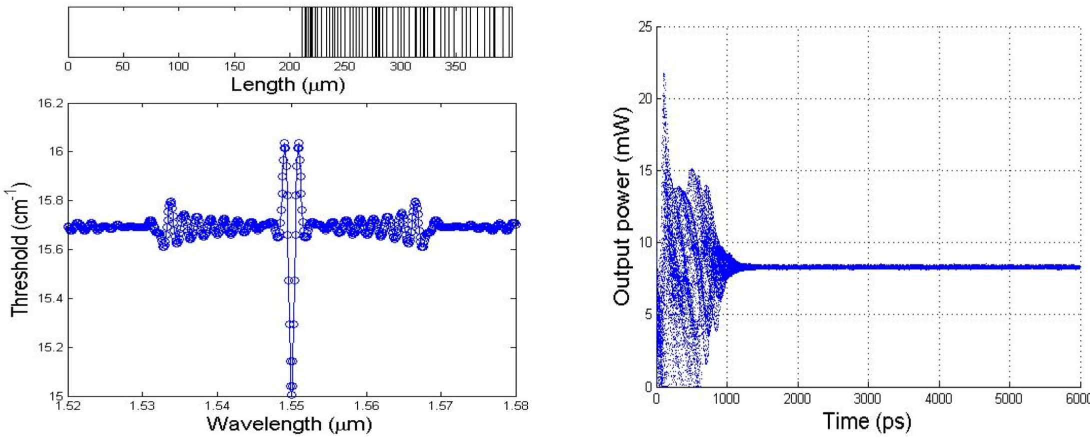

Figure 6.16 (a) 48-slot asymmetric DM laser structure and threshold gain; (b) output power from TD-TWM simulation.

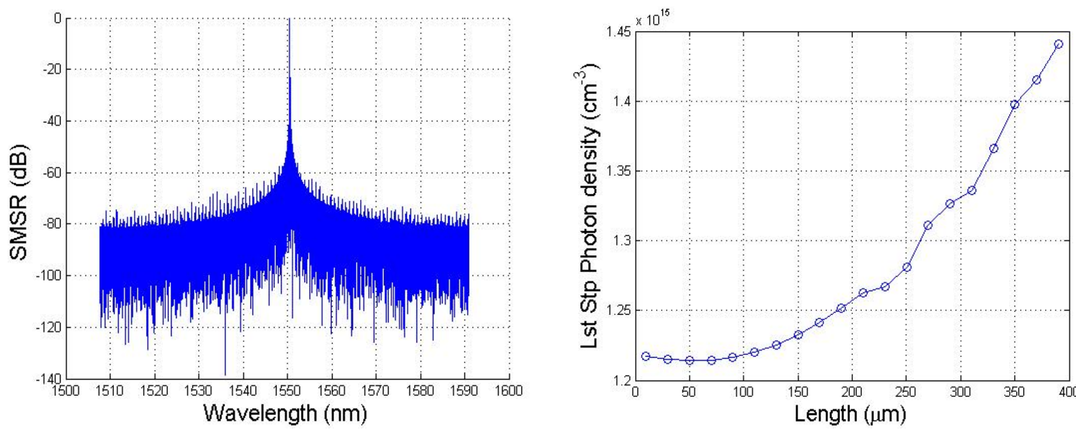

Figure 6.17 48-slot asymmetric DM laser spectrum and photon distribution.

By increasing the slot number to 48, as in Fig. 6.16-17, we see the increase in threshold gain difference to 0.7 cm^{-1} and the SMSR to around 60 dB.

Then, in the following as in Fig. 6.18-19, we can summarize and plot the sensitivity study graphs, according to different etching index contrast and slot numbers:

By fixing the contrast of $\Delta n = 0.005$ while changing slot number from 11 to 50 as above, we can summarize and plot the threshold gain difference and lasing spectrum SMSR with respect to slot number as in Fig.6.18 (a) and (b).

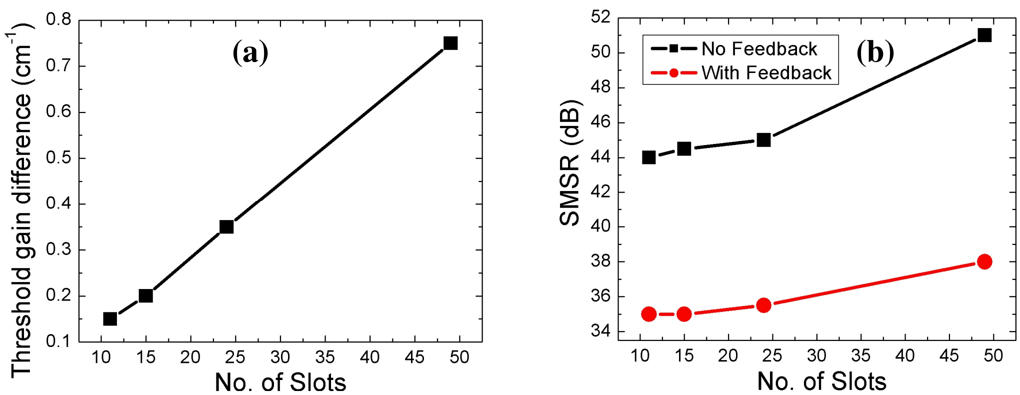

Figure 6.18 (a) Difference between the lowest and second lowest threshold gain of DM lasers v.s. different number of slots etched; (b) SMSR calculated from TD-TWM for corresponding cases in (a) before and after feedback is applied

By using the 15-slot case but changing slot index contrast from 0.001 to 0.01, we can also plot the same quantities as in Fig.6.19 (a) and (b).

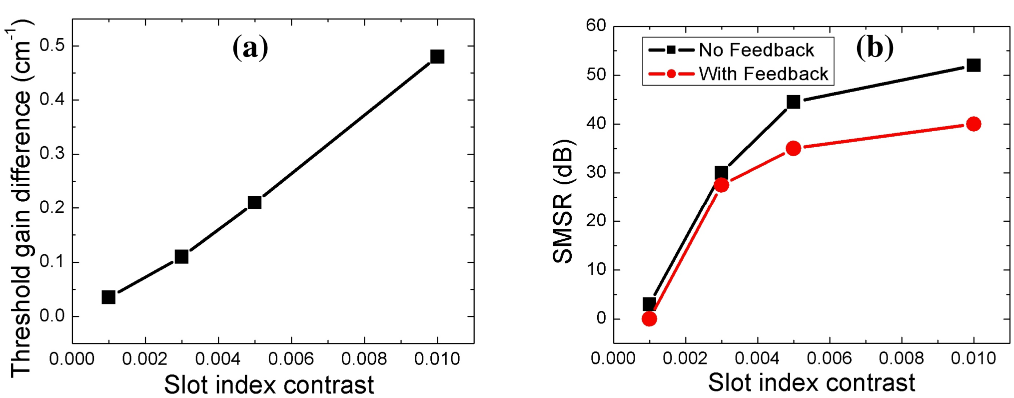

Figure 6.19 (a) Threshold gain difference of the 15-slot asymmetric DM laser with different index-contrast slots etched; (b) SMSR calculated for corresponding cases in (a) before and after feedback is applied.

From the above plots, we can see that threshold gain difference can be linearly increased by etching more or deeper slots into the FP cavity, which improves the spectrum SMSR, correspondingly. However, more importantly, the effect of deeper slots will be levelled off at higher contrast, and their improvements over feedback will be reduced, as the more/deeper slots etched the more sensitive the structure will be to external perturbations. This is also indicating that a recent development of DM laser [94] using the "pixel method" has to adopt coarse meshing segments, to reduce feedback perturbation effect on designed structures for use in the high speed, strong feedback optical communication networks. Therefore, the trade-off between slot number/depth and single-mode performance has to be balanced for an optimized DM laser.

6.5 Summary

In this chapter, we have described the design of discrete mode laser by etching a few shallow slots on the FP cavity to change threshold gain profile of the structure at different wavelengths. The design procedure is valid only at approximations when product of the number of slots and their index changes is negligible compared to the total cavity index value. And the design is generally a realization of Fourier transform of the threshold in wavelength space to its corresponding slot positions in real space. Time-domain traveling wave model is also applied to test the structure, and confirmed that this design of the single mode laser can be used to produce light signals with high SMSR and spectral purity.

Further optimization of the device is done for better optical performances and lasing stabilities under various conditions, especially at direct modulation. By using the time domain transfer matrix method as an experimental tool for the structural parameter optimizations, we can do comprehensively studies of the design and improve its single-mode quality. From the simulated TD-TMM results, we see that with proper choice of the slot number and index depth etched, high SMSR with strong feedback immunity can be achieved.

Chapter 7

Conclusions and Suggestions for Future Research

7.1 Summary of Contributions

The objective of this thesis was to study and design new types of lasers using the FP cavity, to achieve high SMSR single-mode lasing that can be immune to certain level of optical feedbacks for optical network communication applications.

The major contributions of this thesis are summarized as follows and corresponding publications can be found in Appendix D.

1. The design of asymmetric Bragg reflection waveguide based single mode laser, and its application in the Si-rich SiO_2 laser designs.
2. Comprehensive implementation of the time domain transfer matrix method, including temperature and feedback effects.
3. TD-TMM study of discrete mode lasers for the first time. And further optimization of the DM laser considering feedback and dynamic effects.

7.2 Suggestions for Future Research

Although we have conducted some detailed investigations of the transversely and longitudinally modified FP lasers for their single-mode lasing properties, there are still rooms for the improvements of those devices. For the DM laser, we can also employ the newly proposed pixel method [94] to do the single-mode design, which can relieve the small perturbation restraints on the slot numbers and etching depth, etc., in a more natural manner. But there are still issues in their currently designed structures, such as the feedback sensitivity problem, where the more slots we use as gratings in the FP cavity, the more vulnerable the laser will be to external perturbations. Also, their design is using the costly E-beam lithography to etch the slots, and should be further optimized to use lower resolution such that the photolithography can be employed.

Appendix A

Single-slot FP laser configuration and parameters

Parameters	**values**
Laser length L (μm)	400
Active region width w (μm)	1.7
Active region depth d (μm)	0.16
Facet reflectivities r_1, r_2	0.3
Confinement factor (Γ)	0.3
Effective index without injection n_{eff}^0	3.2
Group index n_g	4
Internal loss α (cm^{-1})	20
Differential gain g_N (10^{-16} cm^2)	2.7
Transparent carrier density N_0 (10^{18} cm^{-3})	0.9
Non-linear gain saturation coefficient ε (10^{-17} cm^3)	2.0
Carrier dependence of index dn/dN (10^{-20} cm^3)	-0.374
Linear recombination coefficient A (10^9 s^{-1})	0.1
Bimolecular radiation coefficient B (10^{-10} cm^3 s^{-1})	1
Auger coefficient C (10^{-29} cm^6 s^{-1})	3
Linewidth enhancement factor	5
Spontaneous emission coefficient (β)	5×10^{-5}

Appendix B

DFB laser configuration and parameters

Parameters	values
Grating period Λ (nm)	244.5
Bragg order	1
Active region volume V (μm^3)	90
Facet reflectivities r_1, r_2	0
Laser length L (μm)	300
Confinement factor (Γ)	0.3
Effective index without injection n_{eff}^0	3.2
Group index n_g	3.6
Internal loss α (cm^{-1})	50
Differential gain g_N (10^{-16} cm^2)	2.5
Transparent carrier density N_0 (10^{18} cm^{-3})	1.0
Non-linear gain saturation coefficient ε (10^{-17} cm^3)	6.0
Carrier dependence of index dn/dN (10^{-20} cm^3)	-0.374
Linear recombination coefficient A (10^9 s^{-1})	0.1
Bimolecular radiation coefficient B (10^{-10} cm^3 s^{-1})	1
Auger coefficient C (10^{-29} cm^6 s^{-1})	7.5
Spontaneous emission coefficient (β)	5×10^{-5}
Coupling coefficient κ (cm^{-1})	50

Appendix C

DM laser structure: slot positions

(Asymmetric DM cases)

11 slots	15 slots	48 slots	
387.208632	391.559372	397.862677	(continued)
364.442802	375.090446	392.049960	277.732766
343.614483	358.137156	384.299825	274.826288
323.997120	341.668173	379.940221	269.982406
306.075072	326.652373	375.822871	265.380597
290.817072	315.269408	368.799227	262.232032
276.285661	300.737974	362.986511	259.809903
260.543233	288.143993	359.111363	257.387834
246.011795	277.971892	355.236149	254.481388
235.839739	264.893610	348.212538	249.879709
222.277055	256.901207	343.126396	245.762285
	244.549493	339.493376	242.855892
	237.283675	335.860343	240.433794
	226.385066	330.047706	238.496052
	219.361398	324.235006	236.074019
		320.844205	232.925379
		317.453409	228.565836
		313.578153	225.175034
		307.281156	222.752943
		302.921566	220.573114
		300.015144	218.635400
		297.108719	216.697752
		293.233475	214.275622
		287.178619	210.884855

(Symmetric DM cases)

44 slots		60 slots	
383.814848	(continued)	387.450689	(continued)
358.627217	193.451366	366.137979	193.937243
336.345732	191.998063	348.215937	193.210438
316.970610	189.818119	333.684516	191.999363
299.775099	187.396047	318.668657	190.546023
284.274840	184.974016	304.379437	188.608378
274.829361	182.794091	295.418333	186.670616
262.477583	180.614244	283.066605	184.975127
255.696165	178.434345	276.285138	183.279611
245.524094	175.770112	265.870854	181.826373
240.437986	170.684000	259.816027	180.130875
236.078423	164.144753	254.729877	178.677501
229.539177	159.785191	246.737498	176.497679
224.453064	154.699082	242.135783	173.833406
221.788831	144.527011	238.744975	169.473830
219.608932	137.745593	235.354091	164.629918
217.429085	125.393816	230.510179	161.239034
215.249160	115.948336	226.150602	157.848226
212.827129	100.448077	223.486329	153.246511
210.405057	83.252566	221.306508	145.254132
208.225114	63.877444	219.853134	140.167981
206.771810	41.595959	218.157636	134.113154
	16.408328	216.704398	123.698871
		215.008882	116.917403
		213.313393	104.565676
		211.375630	95.604572
		209.437985	81.315352
		207.984646	66.299493
		206.773571	51.768071
		206.046765	33.846030
			12.533320

90 slots		
393.511071	(continued)	(continued)
378.737492	216.223204	156.638620
364.206050	215.254251	153.489983
354.518276	214.043180	148.161681
341.682188	212.831970	143.802094
333.205408	211.620842	140.411357
322.064596	210.409775	137.262681
315.283190	209.198644	132.418745
304.626762	208.229730	125.152953
298.814071	207.502950	120.551151
292.274841	206.776188	115.949468
284.040217	193.213497	107.714844
279.438534	192.486735	101.175614
274.836732	191.759955	95.362923
267.570940	190.791041	84.706495
262.727004	189.579910	77.925089
259.578328	188.368843	66.784277
256.187591	187.157715	58.307497
251.828004	185.946505	45.471410
246.499702	184.735434	35.783635
243.351065	183.766481	21.252193
240.928985	182.797507	6.478614
238.991259	181.828632	
236.811453	180.859637	
234.389314	179.648564	
231.240714	178.679551	
228.092061	177.468522	
225.427843	176.015198	
223.974488	174.561842	
222.521163	171.897624	
221.310134	168.748971	
220.341121	165.600371	
219.130048	163.178233	
218.161053	160.998426	
217.192178	159.060700	

Appendix D

List of Publications

D.1 International Journals

P.1. Yu Li, Yanping Xi, and Weiping Huang, “Pixel method optimization of DM lasers”, submitted to Optics Express, (2011)

P.2. Yu Li, Yanping Xi, Xun Li, and Weiping Huang, “Design and analysis of single mode Fabry-Perot lasers with high speed modulation capability”, Optics Express, 19, 12131–12140, (2011);

P.3. Yu Li, Yanping Xi, Xun Li, and Weiping Huang, “A single-mode laser based on asymmetric Bragg reflection waveguides”, Optics Express, 17, 11179-11186, (2009).

D.2 Conference papers

P.1. Yu Li, Yanping Xi, and Weiping Huang, “Modeling and design optimization of discrete mode lasers for high speed single-mode operation in optical communication networks”, Annual Meeting of IPR, Toronto, (2011).

Bibliography

[1] T. KATSUYAMA, "Development of Semiconductor Laser for Optical Communication," SEI TECHNICAL REVIEW, **69**, 13 (2009).

[2] A. Yariv, and M. Nakamura, "Periodic structures for integrated optics," Quantum Electronics, IEEE Journal of, **13**, 233-253 (2002).

[3] H. Kogelnik, and C. Shank, "Coupled Wave Theory of Distributed Feedback Lasers," Journal of Applied Physics, **43**, 2327-2335 (1972).

[4] R. Dupuis, and P. Dapkus, "Room temperature operation of GaAlAs/GaAs double heterostructure lasers grown by metalorganic chemical vapor deposition," Applied Physics Letters, **31**, 466 (1977).

[5] A. Yariv, "Coupled-mode theory for guided-wave optics," IEEE Journal of Quantum Electronics, **9**, 919-933 (1973).

[6] J. H. Moon, K. M. Choi, S. G. Mun, and C. H. Lee, "Effects of back-reflection in WDM-PONs based on seed light injection," Photonics Technology Letters, IEEE, **19**, 2045-2047 (2007).

[7] R. Tkach, and A. Chraplyvy, "Regimes of feedback effects in 1.5-μm distributed feedback lasers," Lightwave Technology, Journal of, **4**, 1655-1661 (1986).

[8] A. Banerjee, Y. Park, F. Clarke, H. Song, S. Yang, G. Kramer, K. Kim, and B. Mukherjee, "Wavelength-division-multiplexed passive optical network (WDM-PON) technologies for broadband access: a review [Invited]," Journal of Optical Networking, **4**, 737-758 (2005).

[9] H. Roussell, R. Helkey, G. Betts, and C. Cox III, "Effect of optical feedback on high-dynamic-range Fabry-Perot laser optical links," Photonics Technology Letters, IEEE, **9**, 106-108 (1997).

[10] K. Iga, and K. Kawabata, "Active Bragg Reflector and Its Application to Semiconductor Laser," Japanese Journal of Applied Physics, **14**, 427 (1975).

[11] B. F. Mason, G.A.; DenBaars, S.P.; Coldren, L.A.;, "Widely tunable sampled grating DBR laser with integrated electroabsorption modulator," Photonics Technology Letters, IEEE **11**, 638 - 640 (1999).

[12] J. E. Simsarian, M. C. Larson, H. E. Garrett, H. Xu, and T. A. Strand, "Less than 5-ns wavelength switching with an SG-DBR laser," Photonics Technology Letters, IEEE, **18**, 565-567 (2006).

[13] X. Pan, H. Olesen, and B. Tromborg, "Spectral linewidth of DFB lasers including the effects of spatial holeburning and nonuniform current injection," Photonics Technology Letters, IEEE, **2**, 312-315 (1990).

[14] P. Laurent, A. Clairon, and C. Breant, "Frequency noise analysis of optically self-locked diode lasers," Quantum Electronics, IEEE Journal of, **25**, 1131-1142 (1989).

[15] C. J. Chang-Hasnain, "Tunable VCSEL," Selected Topics in Quantum Electronics, IEEE Journal of, **6**, 978-987 (2000).

[16] G. Steinle, H. Riechert, and A. Y. Egorov, "Monolithic VCSEL with InGaAsN active region emitting at 1.28 m and CW output power exceeding 500 W at room temperature," Electronics Letters, **37**, 93-95 (2001).

[17] F. Koyama, "Recent advances of VCSEL photonics," Journal of Lightwave Technology, **24**, 4502-4513 (2006).

[18] F. Delorme, "Widely tunable 1.55- m lasers for wavelength-division-multiplexed optical fiber communications," Quantum Electronics, IEEE Journal of, **34**, 1706-1716 (1998).

[19] M. Fallahi, M. Dion, F. Chatenoud, I. Templeton, and R. Barber, "High power emission from strained DQW circular-grating surface-emitting DBR lasers," Electronics Letters, **29**, 2117-2118 (1993).

[20] P. Laurent, P. Lemonde, E. Simon, G. Santarelli, A. Clairon, N. Dimarcq, P. Petit, C. Audoin, and C. Salomon, "A cold atom clock in absence of gravity," The European Physical Journal D, **3**, 201-204 (1998).

[21] A. J. Kerman, V. Vuleti , C. Chin, and S. Chu, "Beyond optical molasses: 3D Raman sideband cooling of atomic cesium to high phase-space density," Physical Review Letters, **84**, 439-442 (2000).

[22] T. Giallorenzi, J. Bucaro, A. Dandridge, G. Sigel, J. Cole, S. Rashleigh, and R. Priest, "Optical fiber sensor technology," Quantum Electronics, IEEE Journal of, **18**, 626-665 (1982).

[23] Y. Beregovski, O. Hennig, M. Fallahi, F. Guzman, R. Clemens, S. Mendes, and N. Peyghambarian, "Design and characteristics of DBR-laser-based environmental sensors," Sensors and Actuators B: Chemical, **53**, 116-124 (1998).

[24] S. Park, E. Kim, Y. H. Park, D. Yee, T. Kwon, C. Park, H. Moon, and T. Yoon, "Sweep optical frequency synthesizer with a distributed-Bragg-reflector laser injection

locked by a single component of an optical frequency comb," Optics Letters, **31**, 3594-3596 (2006).

[25] J. Major Jr, S. O'Brien, V. Gulgazov, D. Welch, and R. Lang, "High-power singlemode AlGaAs distributed Bragg reflector laser diodes operating at 856 nm," Electronics Letters, **30**, 496-497 (1994).

[26] J. Major Jr, and D. Welch, "Singlemode InGaAs/GaAs distributed Bragg reflector laser diodes operating at 1083nm," Electronics Letters, **29**, 2121-2122 (1993).

[27] K. Utaka, S. Akiba, K. Sakai, and Y. Matsushima, "Analysis of quarter-wave-shifted DFB laser," Electronics Letters, **20**, 326-327 (1984).

[28] R. Zia, J. A. Schuller, A. Chandran, and M. L. Brongersma, "Plasmonics: the next chip-scale technology," Materials today, **9**, 20-27 (2006).

[29] P. Yeh, A. Yariv, and C. S. Hong, "Electromagnetic propagation in periodic stratified media. I. General theory," Journal of the Optical Society of America, **67**, 423-438 (1977); Y. Fink, J. N. Winn, S. H. Fan, J. D. Jannopoulos, and E. L. Thomas, Science, **282**, 1679 (1999)

[30] P. S. J. Russell, "Optics of Floquet-Bloch waves in dielectric gratings," Applied Physics B: Lasers and Optics, **39**, 231-246 (1986).

[31] Y. Li, Y. Xi, X. Li, and W. P. Huang, "A single-mode laser based on asymmetric Bragg reflection waveguides," Optics Express, **17**, 11179-11186 (2009).

[32] J. Li, and K. S. Chiang, "Light guidance in a photonic bandgap slab waveguide consisting of two different Bragg reflectors," Optics Communications, **281**, 5797-5803 (2008).

[33] J. Li, and K. S. Chiang, "Guided modes of one-dimensional photonic bandgap waveguides," Journal of the Optical Society of America B, **24**, 1942-1950 (2007).

[34] S. L. Chuang, *Physics of Optoelectronic Devices* (John Wiley& Sons,, New York, 1996).

[35] P. Fournier, B. P. Orsal, J. M. Peransin, and R. M. Alabedra, "Spontaneous emission factor and gain evaluation of an optical amplifier by using noise measurements with no input signal," (1995), p. 257.

[36] L. Zhang, S. Yu, M. Nowell, D. Marcenac, J. Carroll, and R. Plumb, "Dynamic analysis of radiation and side-mode suppression in a second-order DFB laser using time-domain large-signal traveling wave model," Quantum Electronics, IEEE Journal of, **30**, 1389-1395 (1994).

[37] S. Yu, "An improved time-domain traveling-wave model for vertical-cavity surface-emitting lasers," Quantum Electronics, IEEE Journal of, **34**, 1938-1948 (1998).

[38] M. Davis, and R. O'Dowd, "A transfer matrix method based large-signal dynamic model for multielectrode DFB lasers," Quantum Electronics, IEEE Journal of, **30**, 2458-2466 (1994).

[39] M. Davis, and R. O'Dowd, "A transfer matrix-based analysis of multielectrode DFB lasers," Photonics Technology Letters, IEEE, **3**, 603-605 (1991).

[40] S. Hansmann, "Transfer matrix analysis of the spectral properties of complex distributed feedback laser structures," Quantum Electronics, IEEE Journal of, **28**, 2589-2595 (1992).

[41] S. Hansmann, H. Walter, H. Hillmer, and H. Burkhard, "Static and dynamic properties of InGaAsP-InP distributed feedback lasers-a detailed comparison between experiment and theory," Quantum Electronics, IEEE Journal of, **30**, 2477-2484 (1994).

[42] O. A. Lavrova, and D. J. Blumenthal, "Detailed transfer matrix method-based dynamic model for multisection widely tunable GCSR lasers," Lightwave Technology, Journal of, **18**, 1274-1283 (2000).

[43] W. W. Rigrod, "Saturation Effects in High Gain Lasers," Journal of Applied Physics, **36**, 2487-2490 (1965).

[44] D. Roessler, "Kramers-Kronig analysis of reflection data," British Journal of Applied Physics, **16**, 1119 (1965).

[45] D. Jones, L. Zhang, J. Carroll, and D. Marcenac, "Dynamics of monolithic passively mode-locked semiconductor lasers," Quantum Electronics, IEEE Journal of, **31**, 1051-1058 (1995).

[46] D. Marcenac, and J. Carroll, "Quantum-mechanical model for realistic Fabry-Perot lasers," (IET, 1993), pp. 157-171.

[47] W. Li, X. Li, and W. P. Huang, "A traveling-wave model of laser diodes with consideration for thermal effects," Optical and Quantum Electronics, **36**, 709-724 (2004).

[48] Y. Hong, S. Bandyopadhyay, S. Sivaprakasam, P. Spencer, and K. Shore, "Noise characteristics of a single-mode laser diode subject to strong optical feedback," Journal of Lightwave Technology, **20**, 1847 (2002).

[49] S. G. Abdulrhmann, M. Ahmed, T. Okamoto, W. Ishimori, and M. Yamada, "An improved analysis of semiconductor laser dynamics under strong optical feedback," Selected Topics in Quantum Electronics, IEEE Journal of, **9**, 1265-1274 (2004).

[50] L. Langley, K. Shore, and J. Mørk, "Dynamical and noise properties of laser diodes subject to strong optical feedback," Optics Letters, **19**, 2137-2139 (1994).

[51] T. Deng, G. Xia, and Z. Wu, "Influence of the optical feedback on the large signal modulation characteristics of the external cavity semiconductor laser," Journal of Materials Science: Materials in Electronics, **17**, 301-305 (2006).

[52] L. Ramunno, and J. Sipe, "External cavity semiconductor laser model for the strong feedback regime," Journal of Modern Optics, **52**, 1421-1448 (2005).

[53] F. Grillot, B. Thedrez, and G. H. Duan, "Feedback sensitivity and coherence collapse threshold of semiconductor DFB lasers with complex structures," Quantum Electronics, IEEE Journal of, **40**, 231-240 (2004).

[54] F. Grillot, B. Thedrez, O. Gauthier-Lafaye, M. F. Martineau, V. Voiriot, J. L. Lafragette, J. L. Gentner, and L. Silvestre, "Coherence-collapse threshold of 1.3-μm semiconductor DFB lasers," Photonics Technology Letters, IEEE **15**, 9 - 11 (2003).

[55] M. Homar, J. Moloney, and M. San Miguel, "Travelling wave model of a multimode Fabry-Perot laser in free running and external cavity configurations," Quantum Electronics, IEEE Journal of, **32**, 553-566 (1996).

[56] D. Kozlowski, S. Young, S. Plumb, and J. England, "Time-domain modeling of mode suppression in 1.3- m Fabry-Perot lasers," Photonics Technology Letters, IEEE, **8**, 755-757 (1996).

[57] Y. Xi, X. Li, and W. P. Huang, "Time-domain standing-wave approach based on cold cavity modes for simulation of DFB lasers," Quantum Electronics, IEEE Journal of, **44**, 931-937 (2008).

[58] C. Tsang, D. Marcenac, J. Carroll, and L. Zhang, "Comparison between 'power matrix model' and 'time domain model' in modelling large signal responses of DFB lasers," (IET, 1994), pp. 89-96.

[59] G. Keiser, *FTTX concepts and applications* (Wiley Online Library, 2006).

[60] M. F. Alam, and M. A. Karim, "External Optical Feedback Effects in Distributed Feedback Semiconductor Lasers," Advances in Imaging and Electron Physics, **107**, 73-120 (1999).

[61] M. F. Alam, M. A. Karim, and S. Islam, "Effects of structural parameters on the external optical feedback sensitivity in DFB semiconductor lasers," Quantum Electronics, IEEE Journal of, **33**, 424-433 (1997).

[62] K. Petermann, "External optical feedback phenomena in semiconductor lasers," Selected Topics in Quantum Electronics, IEEE Journal of, **1**, 480-489 (1995).

[63] K. Emura, M. Shikada, S. Yamazaki, K. Komatsu, I. Mito, and K. Minemura, "Optical DPSK heterodyne detection experiments using DBR laser diodes with external optical feedback," Electronics Letters, **21**, 1121-1122 (2007).

[64] G. Morthier, and P. Vankwikelberge, *Handbook of distributed feedback laser diodes* (Artech House Norwood, MA, 1997).

[65] C. Herbert, D. Jones, A. Kaszubowska-Anandarajah, B. Kelly, M. Rensing, J. O'Carroll, R. Phelan, P. Anandarajah, P. Perry, and L. Barry, "Discrete mode lasers for communication applications," Optoelectronics, IET, **3**, 1-17 (2009).

[66] W. Yuen, G. Li, R. Nabiev, J. Boucart, P. Kner, R. Stone, D. Zhang, M. Beaudoin, T. Zheng, and C. He, "High-performance 1.6 m single-epitaxy top-emitting VCSEL," Electronics Letters, **36**, 1121-1123 (2000).

[67] T. Kageyama, T. Miyamoto, S. Makino, N. Nishiyama, F. Koyama, and K. Iga, "High-temperature operation up to 170 C of GaInNAs-GaAs quantum-well lasers grown by chemical beam epitaxy," Photonics Technology Letters, IEEE, **12**, 10-12 (2000).

[68] E. Hall, S. Nakagawa, G. Almuneau, J. Kim, and L. Coldren, "Room-temperature, CW operation of lattice-matched long-wavelength VCSELs," Electronics Letters, **36**, 1465-1467 (2000).

[69] G. Almuneau, E. Hall, S. Nakagawa, J. Kim, D. Lofgreen, O. Sjölund, C. Luo, D. Clarke, J. English, and L. Coldren, "Molecular beam epitaxial growth of monolithic 1.55 m vertical cavity surface emitting lasers with AlGaAsSb/AlAsSb Bragg mirrors," Journal of Vacuum Science & Technology B: Microelectronics and Nanometer Structures, **18**, 1601 (2000).

[70] J. Boucart, C. Starck, F. Gaborit, A. Plais, N. Bouche, E. Derouin, L. Goldstein, C. Fortin, D. Carpentier, and P. Salet, "1-mW CW-RT monolithic VCSEL at 1.55 m," Photonics Technology Letters, IEEE, **11**, 629-631 (1999).

[71] S. Yu, "Dynamic behavior of vertical-cavity surface-emitting lasers," Quantum Electronics, IEEE Journal of, **32**, 1168-1179 (1996).

[72] U. Fiedler, G. Reiner, P. Schnitzer, and K. Ebeling, "Top surface-emitting vertical-cavity laser diodes for 10-Gb/s data transmission," Photonics Technology Letters, IEEE, **8**, 746-748 (1996).

[73] P. Zorabedian, and J. Trutna, WR, "Interference-filter-tuned, alignment-stabilized, semiconductor external-cavity laser," Optics Letters, **13**, 826-828 (1988).

[74] D. T. Neilson, "Tolerance of optical interconnections to misalignment," Applied Optics, **38**, 2282-2290 (1999).

[75] M. Munroe, S. Hodges, J. Cooper, and M. G. Raymer, "Total intensity modulation and mode hopping in a coupled-cavity laser as a result of external-cavity length variation," Optics Letters, **19**, 105 (1994).

[76] L. Coldren, and T. Koch, "Analysis and design of coupled-cavity lasers--Part I: Threshold gain analysis and design guidelines," Quantum Electronics, IEEE Journal of, **20**, 659-670 (1984).

[77] D. Marcuse, "Computer simulation of laser photon fluctuations: coupled-cavity lasers," Quantum Electronics, IEEE Journal of, **21**, 154-161 (1985).

[78] J. Amin, M. Hempstead, J. Román, and J. Wilkinson, "Tunable coupled-cavity waveguide laser at room temperature in Nd-diffused Ti: LiNbO_3," Optics Letters, **19**, 1541-1543 (1994).

[79] S. Mahnkopf, R. Marz, M. Kamp, G. H. Duan, F. Lelarge, and A. Forchel, "Tunable photonic crystal coupled-cavity laser," Quantum Electronics, IEEE Journal of, **40**, 1306-1314 (2004).

[80] W. Tsang, N. Olsson, and R. Logan, "High speed direct single frequency modulation with large tuning rate and frequency excursion in cleaved coupled cavity semiconductor lasers," Applied Physics Letters, **42**, 650-652 (1983).

[81] H. Gingrich, D. Chumney, S. Z. Sun, S. Hersee, L. Lester, and S. Brueck, "Broadly tunable external cavity laser diodes with staggered thickness multiple quantum wells," Photonics Technology Letters, IEEE, **9**, 155-157 (1997).

[82] J. den Besten, R. Broeke, M. van Geemert, J. Binsma, R. Heinrichsdorff, T. van Dongen, E. Bente, X. Leijtens, and M. Smit, "An integrated coupled-cavity 16-wavelength digitally tunable laser," Photonics Technology Letters, IEEE, **14**, 1653-1655 (2002).

[83] S. Mahnkopf, M. Arlt, M. Kamp, V. Colson, G. H. Duan, and A. Forchel, "Two-channel tunable laser diode based on photonic crystals," Photonics Technology Letters, IEEE, **16**, 353-355 (2004).

[84] B. Kelly, R. Phelan, D. Jones, C. Herbert, J. O'Carroll, M. Rensing, J. Wendelboe, C. Watts, A. Kaszubowska, and P. Anandarajah, "Discrete mode laser diodes with very narrow linewidth emission," Electronics Letters, **43** (2007).

[85] F. Hollinger, and C. Jung, "Single-longitudinal-mode laser as a discrete dynamical system," Journal of the Optical Society of America B, **2**, 218-225 (1985).

[86] R. Phelan, W. H. Guo, Q. Lu, D. Byrne, B. Roycroft, P. Lambkin, B. Corbett, F. Smyth, L. P. Barry, and B. Kelly, "A novel two-section tunable discrete mode Fabry-Perot laser exhibiting nanosecond wavelength switching," Quantum Electronics, IEEE Journal of, **44**, 331-337 (2008).

[87] X. Zhang, A. Liu, D. Tang, and C. Lu, "Discrete wavelength tunable laser using microelectromechanical systems technology," Applied Physics Letters, **84**, 329 (2009).

[88] S. OBrien, and E. OReilly, "Theory of improved spectral purity in index patterned Fabry-Pérot lasers," Applied Physics Letters, **86**, 201101 (2005).

[89] S. O'Brien, A. Amann, R. Fehse, S. Osborne, E. P. O'Reilly, and J. M. Rondinelli, "Spectral manipulation in Fabry-Perot lasers: perturbative inverse scattering approach," Journal of the Optical Society of America B, **23**, 1046-1056 (2006).

[90] C. Guignard, G. Tipaka, O. Vaudel, B. Kelly, J. Patchell, L. Barry, P. Besnard, and J. O'Gorman, "Low sensitivity to optical feedback and optical injection of discrete mode lasers," (IEEE, 2007), pp. 663-664.

[91] A. Kaszubowska-Anandarajah, L. Barry, P. Anandarajah, C. Guignard, B. Kelly, and J. OGorman, "Feedback effects on performance of DM and DFB lasers in RoF systems," ECOC 07 September 16-20, 2007 Berlin, Germany, (2007).

[92] A. Kaszubowska-Anandarajah, L. Barry, P. Anandarajah, C. Guignard, B. Kelly, and J. O'Gorman, "Discrete mode lasers for applications in access networks," (IEEE, 2007), pp. 265-268.

[93] R. Phelan, B. Kelly, J. O'Carroll, C. Herbert, A. Duke, and J. O'Gorman, "- 40° C< T< 95° C mode-hop-free operation of uncooled AlGaInAs-MQW discrete-mode laser diode with emission at λ =1.3 µm," Electronics Letters, **45**, 43-45 (2008).

[94] G. Adolfsson, J. Bengtsson, and A. Larsson, "Spectral engineering of semiconductor Fabry-Perot laser cavities in the weakly and strongly perturbed regimes," Journal of the Optical Society of America B, **27**, 118-127 (2010).

[95] Bijlani, B.J, Helmy, A.S., Bragg Reflection Waveguide Diode Lasers, Optics Letters, 34, 3734 – 3736, (2009).

[96] Cunzhu Tong, Bijlani, B.J, Alali, S., Helmy, A.S., Characteristics of Edge-Emitting Bragg Reflection Waveguide Lasers, IEEE Journal of Quantum Electronics, 46, 1605 – 1610, (2010).